MRTOF とα-TOF 検出器を用いた超重核の直接質量測定

庭瀬, 暁隆

First direct mass measurement of superheavy nuclide via MRTOF mass spectrograph equipped with an α-TOF detector

Toshitaka Niwase

Department of Physics, Kyushu University

February 23, 2021

Contents

Abstract

The ground state atomic mass is one of the most fundamental physical quantities and has a unique value for each nucleus. Mass is an important tool not only for discussing nucleon-nucleon interaction but also for uniquely determining the mass number and atomic number of unknown superheavy elements, by providing a fingerprint for the identification of elements. Precision mass measurements of nuclides have been performed at many laboratories in the world. Prior to this work, the heaviest element for which atomic masses were directly measured was Lawrencium (Z=103); no such measurements had been made for a superheavy element. We have carried out precision mass measurements of several heavy nuclei in the SHE-Mass facility using a multi-reflection time-of-flight mass spectrograph (MRTOF-MS), and the gas-filled recoil ion separator GARIS-II. Due to the extremely low fusion cross section, the amount of ions to work with is small in superheavy element experiments. Therefore, accurate mass measurements are required that can discriminate against background events such as cosmic rays, environmental noise, dark counts, etc.

In this study, we have developed a new detector, which we call "α-TOF", for the first direct mass measurement of a superheavy nuclide. The α-TOF detector comprises a Si semiconductor detector embedded in a commercial time-of-flight detector, to allow correlations between the acquisition of time-of-flight signals and subsequent alpha decay events. The α-TOF detector enables accurate and precise mass measurement by using correlated alpha decay events as footprints, even for extremely low-yield cases with less than a few events per day.

The characterization of the α-TOF detector was evaluated using a mixed triplet α-source and with a ^{224}Ra radioactive source. The α-TOF detector was evaluated to have an energy resolution of σ=141.1(9) keV and a time resolution of 250.6(68) ps. It is sufficient to distinguish the decay of superheavy nuclides with different atomic numbers. It was also demonstrated that the half-life can be derived from the time difference between the arrival time and the decay time of the ions. In a subsequent online performance test, ^{207}Ra produced by the ^{159}Tb(^{51}V,3n) reaction was measured in a high-background environment to demonstrate the ability of the decay correlation to suppress background events.

The correlated measurement of time-of-flight and decay event can be applied to nuclear spectroscopy studies with MRTOF-MS equipped with the α-TOF. The decay correlated mass measurements of ^{206,207}Ra produced in the ^{159}Tb+^{51}V reaction system have been performed to directly determine the mass excesses ME(^{206}Ra)=3540(54) keV and ME(^{207g}Ra)=3538(15) keV and also the excitation energy of ^{207m}Ra to be E_{ex}=552(42) keV. Furthermore, the branching ratio of ^{207m}Ra was determined from the measured time-of-flight signal and its decay properties, and spin-parity was estimated

to be $13/2^+$, based on its systematics with the reduced alpha width (δ^2) of the neighboring nuclei.

The first direct mass measurement of a superheavy nuclide, ^{257}Db, produced in the ^{208}Pb(^{51}V, $2n$) reaction, was successfully performed using our MRTOF equipped with α-TOF detector. In a total of 105 hours of beam irradiation, we acquired 11 events wherein $^{257}Db^{3+}$ time-of-flight signals were correlated with subsequent α-decay events. The measured correlated decay events are consistent with the decay properties of ^{257}Db or its decay descendants. The mass excess of ^{257}Db was determined to be $ME(^{257}\mathrm{Db})$=100 063(231)(2) keV from a weighted average of these 11 events. The deviation from the indirectly determined value in our previous result was ΔME=171(231) keV. The mass excess derived from each of the individual events were clearly distinguished from those of isobars with different atomic numbers. It was experimentally shown that a single event is sufficient for the identification of Z and A, demonstrating that accurate and precision mass measurement is an extremely powerful tool for the identification of superheavy nuclides.

Chapter 1

Introduction

The purpose of this study is to develop an α-TOF detector to be used in the first direct mass measurement of superheavy elements.

1.1 Superheavy nuclides

There are 92 elements naturally existing on Earth, the heaviest of which is plutonium (Pu) with atomic number $Z = 94$. All of the elements above $Z = 94$ have been artificially synthesized through nuclear reactions. In November 2016, the International Union of Pure and Applied Chemistry (IUPAC) and the International Union of Pure and Applied Physics (IUPAP) approved the names Nihonium (Nh), Moscovium (Mc), Tennessine (Ts), and Oganesson (Og) for atomic number of 113, 115, 117, and 118, respectively. The Periodic Table of the Elements has been filled up to the 7^{th} period. The research is now underway in laboratories around the world to synthesize the first 8^{th} period elements, i.e, elements 119 and 120 [1].

In the 1960s, the prediction of long-lived nuclei, called "islands of stability" [2], was proposed in the nuclei with atomic numbers well beyond those of lead and uranium, as shown in Fig. 1.1. The existence of islands of stability is intrinsically important when discussing the existence limits and stability of nuclei. Until the early 1980s, the islands around $Z = 114$ and neutron number $N = 184$ were referred to as superheavy elements and superheavy nuclides. Nowadays, as pioneered by the field of radiochemistry, the term "superheavy element" denotes a trans-actinide element, *i*.e. an element with $Z \geq 104$ [3].

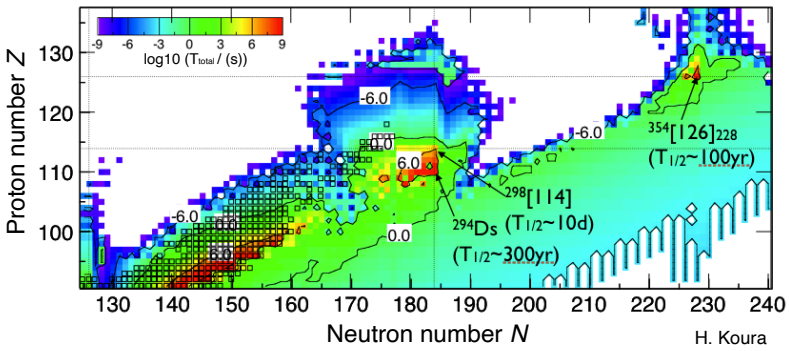

Figure 1.1: Nuclear chart showing superheavy nuclei calculated by KUTY mass formula. Open squares are known nuclides. The KUTY calculation suggests that there are islands of stability with a half-life of about 300 years around $Z = 114$ and $N = 184$, and $N = 230$. Figure courtesy of H. Koura of Japan Atomic Energy Agency (JAEA).

In 1940, the first transuranium nuclide synthesized was $Z = 93$, Neptunium, by McMillan at the University of California, through irradiation of a ^{238}U target with a neutron beam. Subsequently, elements of $Z = 94 - 98$ were synthesized by Seaborg et al., by deuteron irradiation to ^{238}U and further neutron and helium irradiation of the reaction products. These elements have been chemically identified. Elements with atomic numbers 99 and 100 (einsteinium and fermium, respectively), were first discovered in the analysis of hydrogen-bomb experiment products from the Eniwetok Atoll in the Central Pacific Ocean.

All the elements after the atomic number of 101 were produced by fusion reactions using accelerators. Mendelevium was synthesized by Seaborg et al. using a fusion reaction of ^{253}Es(α,n)^{256}Md. In the 1960s, several elements were synthesized using so-called hot fusion reactions by a group of soviet scientists lead by Oganessian. In this method, actinide elements such as uranium and americium were used as target nucleus to produce compound nuclei with high excitation energy, resulting in multiple neutrons being emitted for cooling of the evaporation residue (ER). This method was successfully applied to synthesize elements with atomic numbers from 102, nobelium, to 106, seaborgium.

In 1974, Oganessian proposed a cold fusion reaction, which uses a double closed shell target such as ^{208}Pb, and the stable nuclides were used as incident particle. In this method, the Q-value of the reaction is reduced and the excitation energy of the compound nucleus is lower than those produced in hot fusion reactions. The SHIP group at GSI in Germany successfully synthesized elements of atomic numbers from 107, bohrium, to 112, copernicium, using cold fusion reactions. And in 2004, the first event for element

113, nihonium, was reported by Morita et al. at RIKEN using a cold fusion reaction of ^{70}Zn+^{209}Bi.

The synthesis process of superheavy elements can be considered as a two-stage process of formation and de-excitation according to the compound nuclear model explained by N. Bohr [4], the evaporation residue cross section can be described by multiplication of the fusion probability (P_{fus}) and the survival probability (P_{surv}). P_{surv} is expressed as the competition between the neutron emission width and the fission width $\Gamma_{\mathrm{n}}/\Gamma_{\mathrm{f}}$ of the compound nucleus, and the probability decreases with increasing excitation energy, therefore the fusion of nuclei in a reaction system with low excitation energy is required. This is the concept of cold fusion reactions. The fusion probability, P_{fus}, decreases drastically due to "fusion hindrance" as the product of the number of protons in the projectile nucleus Z_1 and the target nucleus Z_2 increases. For asymmetric reaction systems such as hot fusion reactions, the P_{fus} would be larger than symmetric cold fusion reactions. The cross section to produce element 113 by the cold fusion reaction is already 22 fb (fb=10^{-15} barn; 1 barn=10^{-24}cm^2), and thus it is unreasonable to synthesize higher-Z nuclides in this way.

Oganessian found that the excitation energy of the compound nucleus can be relatively suppressed even in the hot fusion reaction by using ^{48}Ca, which is a doubly closed shell nuclide, as a projectile [5]. By this method, Fl (Z = 114) to Og (Z = 118) have been synthesized, and the periodic table of elements has been completed up to the 7^{th} period. The discovery of transuranium elements are summarized in Table 1.1.

Table 1.1: Summary of the synthesized trans-uranium elements.

Z	Symbol	Reaction	Investigators	Year
93	Np	^{238}U(n,γ)^{239}U $\rightarrow^{239}$Np	MacMillan et al.,	1939
94	Pu	^{238}U(d,2n)^{238}Np $\rightarrow^{238}$Pu	Seaborg et al.,	1940
95	Am	^{239}Pu(2n,γ)^{241}Pu $\rightarrow^{241}$Am	Seaborg et al.,	1944
96	Cm	^{239}Pu(α,n)^{242}Cm	Seaborg et al.,	1944
97	Bk	^{241}Am(α,2n)^{243}Bk	Seaborg et al.,	1949
98	Cf	^{242}Cm(α,n)^{245}Cf	Seaborg et al.,	1950
99	Es	^{238}U+15n $\rightarrow^{253}$Es	Seaborg et al.,	1953
100	Fm	^{238}U+17n $\rightarrow^{255}$Fm	Seaborg et al.,	1953
101	Md	^{253}Es(α,n)^{256}Md	Seaborg et al.,	1955
102	No	^{246}Cm(^{12}C,4n)^{254}No	Seaborg et al.,	1958
103	Lr	^{252}Cf(^{11}B,6n)^{257}Lr	Ghiorso et al.,	1961
104	Rf	^{249}Cf(^{12}C,4n)^{257}Rf	Ghiorso et al.,	1969
105	Db	^{249}Cf(^{15}N,4n)^{260}Db	Ghiorso et al.,	1970
106	Sg	^{249}Cf(^{18}O,4n)^{263}Sg	Ghiorso et al.,	1974
107	Bh	^{209}Bi(^{54}Cr,n)^{262}Bh	Armbruster et al.,	1981
108	Hs	^{208}Pb(^{58}Fe,n)^{265}Hs	Armbruster et al.,	1984
109	Mt	^{209}Bi(^{58}Fe,n)^{266}Mt	Armbruster et al.,	1982
110	Ds	^{208}Pb(^{62}Ni,n)^{269}Ds	Armbruster et al.,	1995
111	Rg	^{209}Bi(^{64}Ni,n)^{272}Rg	Hofmann et al.,	1995
112	Cn	^{208}Pb(^{70}Zn,n)^{277}Cn	Hofmann et al.,	1996
113	Nh	^{209}Bi(^{70}Zn,n)^{278}Nh	Morita et al.,	2004
114	Fl	^{242}Pu(^{48}Ca,3n)^{287}Fl	Oganessian et al.,	2004
115	Mc	^{243}Am(^{48}Ca,3n)^{288}Mc	Oganessian et al.,	2004
116	Lv	^{245}Cm(^{48}Ca,2n)^{291}Lv	Oganessian et al.,	2004
117	Ts	^{249}Bk(^{48}Ca,3n)^{294}Ts	Oganessian et al.,	2010
118	Og	^{249}Cf(^{48}Ca,3n)^{294}Og	Oganessian et al.,	2006

1.2 Decay theory of superheavy nuclides

The primary decay modes of extremely heavy nuclides, such as the superheavy elements, include not only β-decay and electron conversion but also α-decay and spontaneous fission. In the case of the superheavy elements, these decay modes play a role in determining their lifetimes and existence limits.

1.2.1 α-decay

One decay mode is α-decay, by which the parent nuclide P is transformed to the daughter nuclide D by emitting an alpha particle (^{4}He nucleus). It is described as

$$ {}^{A}_{Z}\mathrm{P} \Rightarrow {}^{\mathrm{A-4}}_{\mathrm{Z-2}}\mathrm{D} + \alpha + Q_\alpha, \tag{1.1} $$

where A is a mass number, and Q_α is the Q-value of the alpha decay, i.e., the energy released by the alpha decay, which corresponds to the mass difference between P and D+α. In order for alpha decay to be allowed, Q_α >0,

$$ Q_\alpha = (M_P - M_D - M_\alpha)c^2. \tag{1.2} $$

Q_α is described by Eq. (1.2), where M_x denotes the masses of parent (P), daughter (D) and alpha particles. Since in an α-decay, Q_α is distributed in the kinetic energies of an alpha particle and a daughter nucleus, the energy and momentum conservation law requires:

$$ Q_\alpha = E_\alpha + E_D = \frac{1}{2}M_\alpha v_\alpha^2 + \frac{1}{2}M_D v_D^2, \tag{1.3} $$

$$ 0 = M_\alpha v_\alpha - M_D v_D, \tag{1.4} $$

where E_α and E_D are the kinetic energy of alpha particle and daughter nuclei, v_α and v_D are the velocity of these.

From this, the relationship between the Q_α and energy can be written as follows:

$$ E_\alpha = \frac{M_D}{M_\alpha + M_D}Q_\alpha \approx \frac{A-4}{A}Q_\alpha, \tag{1.5} $$

$$ E_D = \frac{M_\alpha}{M_\alpha + M_D}Q_\alpha \approx \frac{4}{A}Q_\alpha. \tag{1.6} $$

The α-decay was explained quantum mechanically as a tunneling effect through the Coulomb barrier by Gamow [6], Condon and Gurney [7]. Their explanation led to the Geiger-Nuttal law, a relationship between the half-life $T_{1/2}$ and the Q_α given by

$$ \log_{10} T_{1/2} = a\frac{Z}{\sqrt{Q_\alpha}} + b, \tag{1.7} $$

where a and b are constants defined for each element. In the region of super-heavy elements, an improved description of the Geiger-Nuttal law has been proposed, and the experimental results have been successfully reproduced.

The improved Geiger-Nuttal law is shown in Eq. (1.8) and the proposed parameters are tabulated in Table 1.2,

$$\log_{10} T_{1/2} = \frac{a_1 Z_P + a_2}{\sqrt{Q_\alpha}} + (b_1 Z_P + b_2). \tag{1.8}$$

Table 1.2: Proposed parameter of Eq. (1.8). In the term b_2, $h_{\log}$ is a correction term for parity: $h_{\log}$=0 (Z, N= even), $h_{\log}$=1.066 (Z= even, N= odd), $h_{\log}$=0.772 (Z= odd, N=even), $h_{\log}$=1.114 (Z,N=odd).

Range	a_1	a_2	b_1	b_2	Reference
$Z > 82$,$N > 126$	2.11329	-48.9879	-0.390040	-16.9543+$h_{\log}$	[8]
$Z > 104$	1.66175	-8.5166	-0.20228	-33.9069	[9]
$Z > 82$, $N > 126$	1.81040	-21.7199	-0.26488	-28.1319	[10]
$100 \leq Z \leq 120$	1.66175	-8.5166	-0.20228	-33.9069+$h_{\log}$	[11]

The conceptual diagram of α-decay is shown in Fig. 1.2. Since the nuclear force is a short-range force, the Coulomb repulsion is dominant in outside R_0 (where R_0 is the surface of a nuclide). Since E_α is lower than the Coulomb barrier, in classical mechanics the alpha particle cannot escape from the parent nucleus. However, in quantum mechanics it is possible to exit the potential wall through the tunneling effect; this process corresponds to the α-decay.

Using the WKB approximation, the barrier penetration probability of α particles is described as

$$\begin{aligned} P &= \exp\left[-\frac{2}{\hbar}\int_{R_0}^{R_E}\sqrt{2M_\alpha[\frac{2(Z-2)e^2}{r} - E_\alpha]}dr\right] \\ &\approx \exp\left[-\frac{R_0\sqrt{2M_\alpha B_\alpha}}{\hbar}(\pi\sqrt{B_\alpha/E_\alpha} - 4)\right], \end{aligned} \tag{1.9}$$

where $B_\alpha = 2(Z-2)e^2/R_0$. The decay constant for α-decay is the product of the transmission coefficient P and the number of times the α particle collides with the barrier f,

$$\lambda = fP. \tag{1.10}$$

If the velocity of the α particle in the nucleus is v, then $f = v/(2R)$, and the decay constant and half-life are written

$$\lambda = \frac{v}{2R}P,\ T_{1/2} = \frac{2Rln2}{vP}. \tag{1.11}$$

In the alpha decay of a given nucleus, there is a microstructure in which several groups of alpha particles with similar energies appear but their intensities differ greatly from one group to another. In order to explain these

features, the internal structure of the nucleus must be taken into account. It uses either R. G. Thomas theory based on the time-independent Schrödinger equation [12] or H. J. Mang theory based on a time-dependent theory [13]. Both of these theories are shown to be equivalent under the assumption that the nuclear wave function satisfies the same boundary conditions. The alpha decay constant is the sum of the terms, each corresponding to a given final state, and is the product of two factors representing potential barrier penetration and reduced width, which can be argued from the systematics of the reduced alpha width (δ^2) of the nucleus as calculated with the Rasmussen prescription [14],

$$\lambda = \delta^2 P/h, \tag{1.12}$$

where h is the Planck constant. Using the partial half-life of α-decay and the barrier penetration factor, which can be obtained from experiments, it is possible to discuss the structure of α-decay.

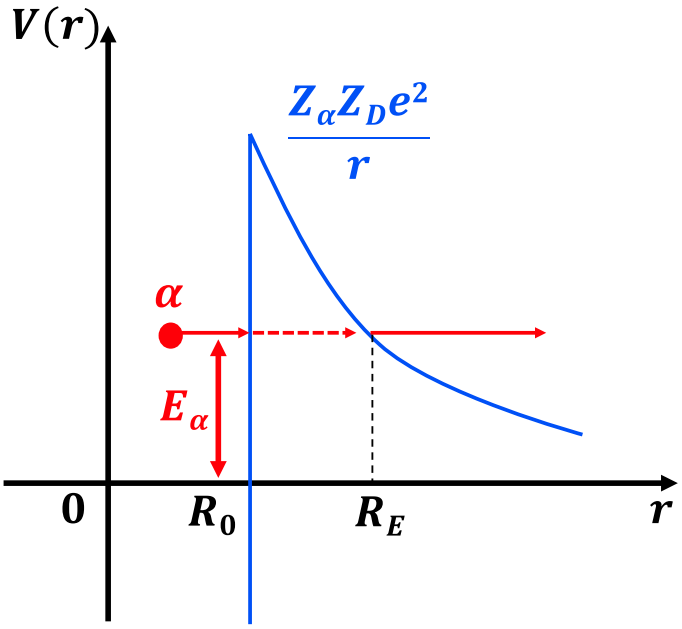

Figure 1.2: Conceptional diagram of alpha decay.

1.2.2 Spontaneous fisson

The binding energy B of the nucleus in the classical liquid drop model can be written from the semi-empirical Weizsäecker-Bethe (WB) mass formula as

$$B(A,Z) = a_v A - a_s A^{2/3} - a_i \frac{(N-Z)^2}{A} - a_c \frac{Z^2}{A^{1/3}} - \delta(A), \tag{1.13}$$

where constant terms in Eq. (1.13) are understood to be the volume term a_v, surface term a_s, asymmetry term a_i, coulomb term a_c, and paring term $\delta(A)$ (Eq. (1.14)). These parameters are determined so as to best reproduce the experimental values. A typical set of the parameters [15] is given below, in units of MeV,

$$\delta(A) = \begin{cases} 12/\sqrt{A} & (Z, N = odd) \\ 0 & (A = odd) \\ -12/\sqrt{A} & (Z, N = even) \end{cases}, \tag{1.14}$$

$$\begin{aligned} a_v &= 15.753, \\ a_s &= 17.804, \\ a_i &= 23.69, \\ a_c &= 0.710. \end{aligned} \tag{1.15}$$

Nuclear fission was described by Bohr and Wheeler in 1939 on the basis of such a classical liquid drop model [16]. A conceptual diagram of fission is shown in Fig. 1.3.

If a spherical nucleus of radius R is deformed into a cigar-shaped rotating ellipse with a constant volume and a major axis of $2a$ and a minor axis of $2b$, a and b are described as

$$\begin{aligned} a &= R(1+\varepsilon), \\ b &= R/\sqrt{1+\varepsilon}, \end{aligned} \tag{1.16}$$

where ε is a deformed parameter.

The surface area of the spheroid S is

$$S = 4\pi R^2 \left(1 + \frac{2}{5}\epsilon^2 + \cdots\right), \tag{1.17}$$

then, the increase in surface energy due to deformation, ΔE_s, is described as

$$\Delta E_s = a_s A^{2/3} \cdot \frac{2}{5}\epsilon^2 = \frac{2}{5}\epsilon^2 E_s^0, \tag{1.18}$$

where E_s^0 is the surface energy of the spherical nucleus, and using the surface tension coefficients γ and a_s, the

$$E_s^0 = 4\pi R^2 \gamma = a_s A^{2/3}. \tag{1.19}$$

From the Coulomb energy of the spherical nucleus, the elliptical Coulomb energy E_c is given

$$E_c^0 = \frac{3}{5}\frac{Z^2e^2}{R} = a_c\frac{Z^2}{A^{1/3}}, \tag{1.20}$$

$$E_c = \frac{3}{5}\frac{Z^2e^2}{R}\left(1 - \frac{1}{5}\epsilon^2 + \dots\right). \tag{1.21}$$

The increase in Coulomb energy due to the deformation is written

$$\Delta E_c = -a_c\frac{Z^2}{A^{1/3}} \cdot \frac{1}{5}\epsilon^2 = \frac{1}{5}\epsilon^2 E_c^0. \tag{1.22}$$

From the above, the variation of the total potential energy is

$$\Delta E = \Delta E_s + \Delta E_c = \frac{2}{5}\epsilon^2 E_s^0\left(1 - \frac{E_c^0}{2E_s^0}\right). \tag{1.23}$$

This formula means that the sphere is more stable if $\Delta E > 0$ and unstable if $\Delta E < 0$. Since ΔE_s is proportional to $A^{2/3}$ and ΔE_c is nearly proportional to $A^{5/3}$, therefore, in regions where A is large, such as the heavy nucleus, the second term increases and approaches $\Delta E < 0$. Consequently, the nucleus is more prone to spontaneous fission.

The value of Z^2/A, where $\Delta E = 0$ is found to be

$$\left(\frac{Z^2}{A}\right)_{\Delta E=0} \simeq 50.15, \tag{1.24}$$

that is, nuclei with $(Z^2/A) > 50.15$ are unstable to deformation and immediately undergo spontaneous fission. In the superheavy nuclei, ^{278}Nh has $(Z^2/A) = 45.93$ and $^{296}119$ has $(Z^2/A) = 47.84$, indicating that the nucleus is very unstable to nuclear deformation. In these nuclei, the probability of spontaneous fission determines the existence limit of the nucleus.

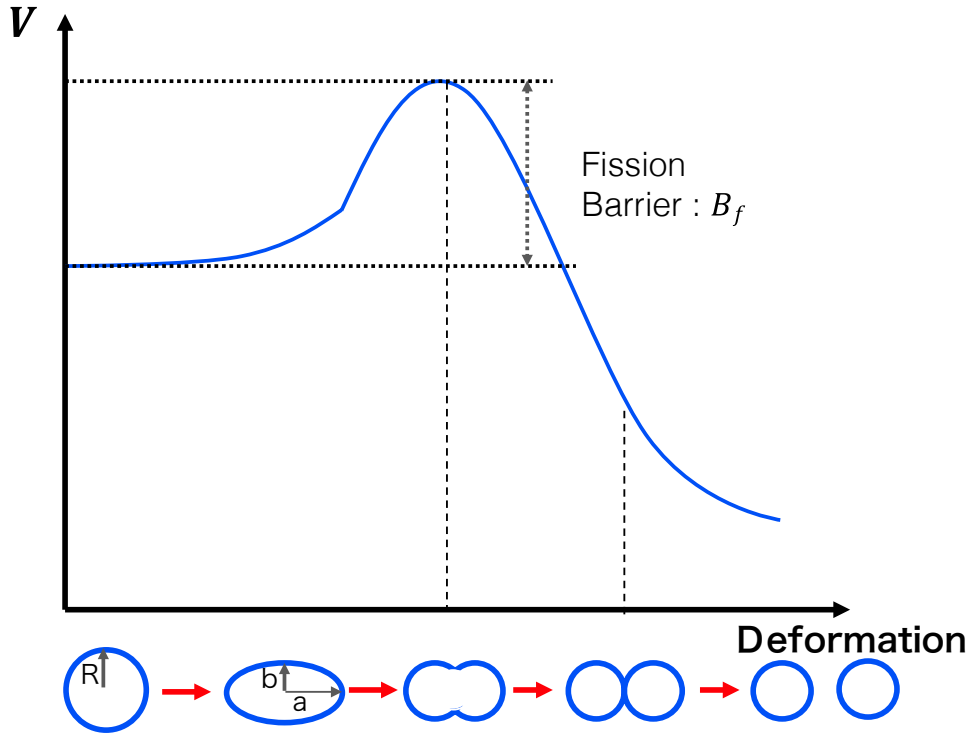

Figure 1.3: Conceptional diagram of spontaneous fission. The horizontal axis is the distance between the fragments and the vertical axis is the potential for the nuclear deformation.

1.3 Direct determination of atomic number of superheavy elements

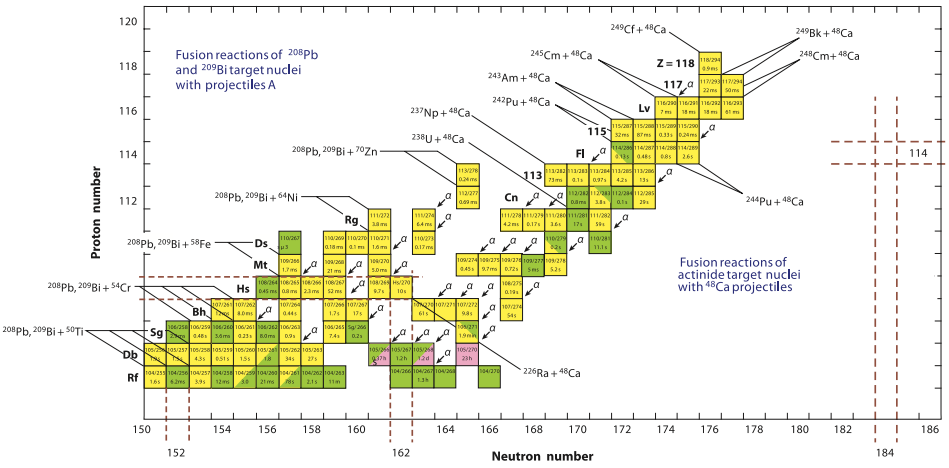

Figure 1.4: Map of the region of superheavy nuclides with the reactions used to synthesize each nuclide. The colors indicate different decay modes. This figure taken from [17].

The nuclides in the superheavy element region and the reactions used to synthesize the various nuclides are shown in Fig. 1.4. The relatively neutron-deficient isotopes of the Nh were synthesized in cold fusion reactions using stable Pb or Bi target. Their decay chain, reaching to known nuclei, meets the criteria for identification of new elements [18]. The more neutron-rich elements 112-118 were produced in hot fusion reactions using an actinide target with a ^{48}Ca beam. The decay chains of the three elements Mc, Ts, and Og have been identified by cross-bombardment reactions, although their decay chains do not reach the known nuclides [19]. Since future superheavy elements synthesis will be mainly based on hot fusion, these unknown nuclides may terminate in spontaneous fission without their decay chains reaching the known nuclides. The Joint Working Group (JWP) of IUPAP and IUPAC has called for pioneering methods to directly identify the atomic number and mass number of synthesized nuclei in future superheavy element search experiments [20].

1.3.1 Characteristic X-ray

Decay from an excited nucleus proceeds by internal conversion as well as α-decay and γ-ray emission. Following the emission of the conversion electron from the atom, X-ray emission is by far the most likely process

in the atomic deexcitation. In 1914, Moseley derived a law that relates the frequency of an element's X-ray spectrum to the atomic number of the element that emitted it [21]. For example, the K_αX- and LX-rays can be described by following relationship formula,

$$\nu_{K\alpha} = R(Z-1)^2(\frac{1}{1^2} - \frac{1}{2^2}), \tag{1.25}$$

$$\nu_L = R(Z-\sigma)^2(\frac{1}{2^2} - \frac{1}{3^2}), \tag{1.26}$$

where R is the Rydberg constant, σ is an arbitrary constant. The characteristic X-ray energies are one of the direct measures used in Z identification. These energies are predicted with high accuracy and are consistent with experimental data up to Db. The X-ray spectroscopy of the superheavy element region has been conducted for a long time, and the first identification of Rutherfordium by X-ray measurement was carried out in the early 1970s [22].

Similar to γ-rays, X-ray detection is inherently inefficient. Therefore, an extensive experimental setup with a Ge detector array is required. Recently, Rudolph et al., at GSI found the first candidate to be a Z fingerprint of the Meitnerium ($Z = 109$) isotopes from spectroscopic studies of Mc and its progenitor produced by the ^{48}Ca+^{243}Am reaction [23].

X-ray measurements provide a tool for atomic number identification, but it may give ambiguous results if pxn evaporation channels are possible or if electron capture decay is the decay mode of the nuclide in the decay chain, as demonstrated in Fig. 1.5. In Figs. 1.5 (a) and (b) we see $3n$ and $p2n$ evaporation channels with two alpha decays prior to X-ray detection. In both cases, characteristic X-rays of element $Z-5$ are observed due to an electron capture decay in the $3n$ channel's decay chain. X-ray measurements identify only the atomic number of an X-ray emitting nuclide, not the atomic number of the initial progenitor. Moreover, the mass number of the nuclide cannot be identified, therefore, the estimation of the evaporation residue includes lots of ambiguities.

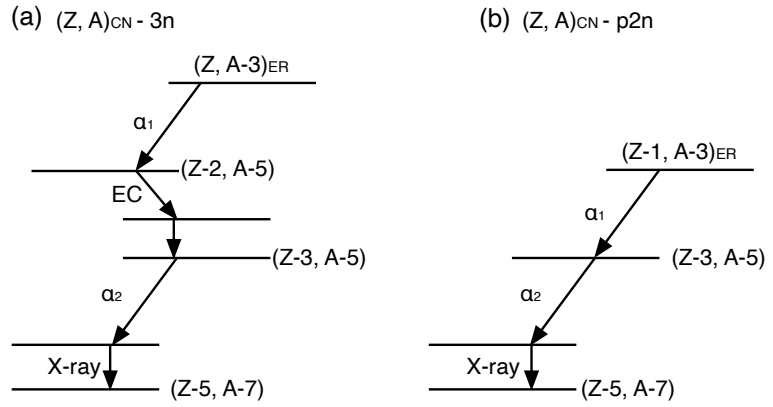

Figure 1.5: Schematic decay diagram exemplifying X-ray measurements for (a) $3n$ evaporation channel and (b) $p2n$ evaporation channel. In both cases the observed X-rays are from element $Z-5$, implying that there is some ambiguity in the assignment of parent nuclide.

1.3.2 Mass measurements

Mass is one of the most important static properties of nuclei. Nowadays, by Einstein's equation $E = mc^2$, we know the binding energy corresponds to the requirement to stabilize the nucleus as a quantum many-body system.

As the binding energy is the minimum energy to take apart a nucleus into a set of discrete nucleons, or the energy released when the nucleons interact and combine as nuclei. The binding energies reflect the nuclear structure and interactions of nucleons, mass measurements provide us with important information.

Table 1.3: Required mass precision for various research fields. These values are taken from [24].

Research Category	$\delta m/m$
Chemistry : Identification of molecules	$10^{-5} - 10^{-6}$
Nuclear mass model	10^{-6}
Nuclear structure : shell, paring	10^{-6}
Nuclear fine structure : deformation, halo	$10^{-7} - 10^{-8}$
Astrophysics : r-process, rp-process	10^{-7}
Atomic physics : Quantum electrodynamics	$10^{-9} - 10^{-11}$

High-precision mass measurements, particularly those of short-lived radionuclides, are required for the study of nuclear structure and astrophysical nucleosynthesis. Table 1.3 shows examples of research categories and req-

uisite relative mass uncertainty ($\delta m/m$). The mass excess (ME) is the fractional part of the mass in atomic mass units. Figure 1.6 shows the mass excess for the isobars of $A = 288, 284$ and 283 in the Nihonium region; the values are extrapolated from known nuclides. The mass excess difference between neighboring isobars increases quadratically with distance from the β stability line. Therefore, Z and A can often be directly and unambiguously distinguished by mass measurements with $\delta m/m \sim 10^{-6}$-level precision.

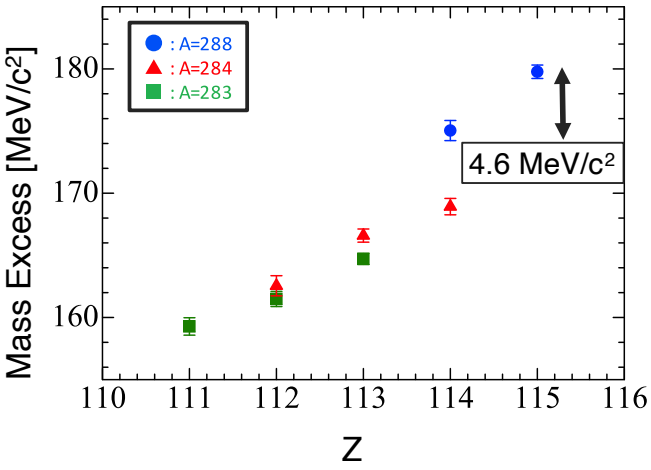

Figure 1.6: Estimated mass excess for select superheavy nuclei with $A = 288, 284$ and 283. The values, taken from AME2016 [25], are extrapolated from known nuclides.

There are a variety of global mass models that attempt to accurately predict unknown masses. The accuracy of these mass models will be crucial to discuss the validity of the unknown nuclear masses once they have been experimentally determined. The first attempt to describe the binding energy of the nucleus is the liquid drop model as described by the semi-empirical WB equation, describe as Eq. (1.13). Although the liquid drop model ignores the nuclear shell effect, it is the basis for many mass models.

Shell model

Attempts to understand the nucleus from the standpoint of the independent particle model began in 1949 with the proposal of the nuclear shell model by Meier and Jensen. The idea of the shell model originated from the accumulation of experimental facts suggesting the phenomenon of shell closure in nuclear structure. It is a fact that when Z or $N = 2$, 8, 20, 28, 50, 82, 126 that nucleus is in a particularly stable state. A nucleus is considered to form a closed shell when Z or N is equal to these numbers, which are called “magic numbers”.

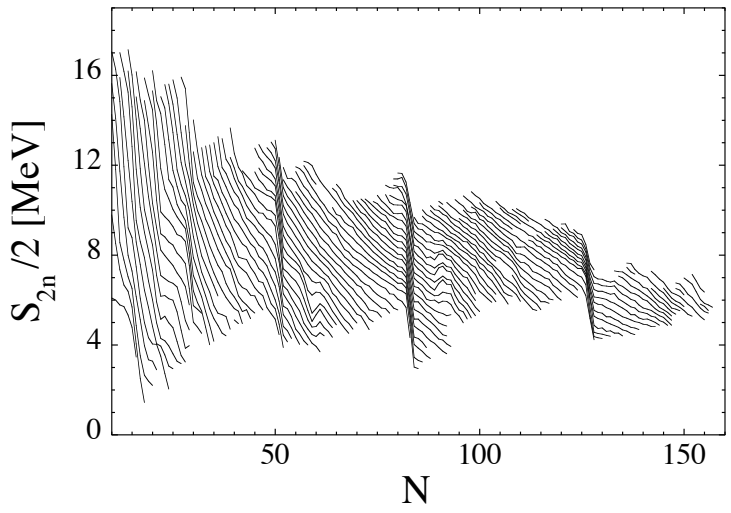

Figure 1.7: Two-neutron separation energies for isotopic chain with known masses. The steep change in S_{2n} seen at N=50, 82, and 126 are a signal of the neutron shell closures. Other non-monotonic features can indicate e.g. shape deformations, etc. This figure taken from [26].

To explain the manifestation of the shell effect, we consider the energy required to remove one or two neutrons from a nucleus, called the neutron separation energy, S_n, and the two-neutron separation energy, S_{2n}, and defined as

$$S_n = B(Z,N) - B(Z,N-1), \tag{1.27}$$
$$S_{2n} = B(Z,N) - B(Z,N-2), \tag{1.28}$$

where B is the binding energy of an atom as determined by the masses of the atoms

$$B(Z,N) = Zm_{\rm p} + Zm_{\rm e} + Nm_{\rm n} - M(N,Z), \tag{1.29}$$

where $m_{\rm p}$, $m_{\rm e}$, and $m_{\rm n}$ are the masses of the proton, electron, and neutron, respectively, while M is the atomic mass. The neutron separation energy is a quantity that describes the stability of the nucleus against neutron emission, and in the nuclides near the neutron drip line, shows the neutron binding state. Figure 1.7 shows a plot of S_{2n} as a function of the neutron number. It can be seen that S_{2n} has a sharp minimum when the number of neutrons increases by one from the magic numbers. That is, the neutrons make a closed shell at this magic number value. The same trend can be seen when we perform similar plots for proton separation energies, S_p and S_{2p}.

Macroscopic-Microscopic approach

The liquid drop model reproduces most of the known isotopes, but does not include the shell structure. In contrast, the shell model explains the occurrence of magic numbers very well, but it does not allow us to calculate the absolute value of the binding energy. Therefore, in 1966, W. D. Myers and W. J. Swiatecki attempted to extend the liquid drop model by combining both theories. These types of approaches are called macroscopic-microscopic approaches because they involve both microscopic assumptions of single-particle energy levels and macroscopic assumptions of the liquid drop model.

Subsequently, V. M. Strutinsky proposed the hypothesis that the shell correction δ_S and the pairing correction δ_P for protons and neutrons contribute to the binding energy of the nucleus. The binding energy B^{MM} described by this macroscopic-microscopic approach is expressed by

$$B^{\mathrm{MM}}(N,Z) = B^{\mathrm{LD}} + \Sigma(\delta S + \delta P), \tag{1.30}$$

where B^{LD} is the binding energy from the liquid drop model. The shell correction is determined by evaluating the energy difference between the level interval S of the non-uniform distribution and the level interval $\bar{S}$ of the uniform distribution,

$$S = \Sigma_i n_i \epsilon_i, \quad \bar{S} = \int_{-\infty}^{\infty} \epsilon g(\epsilon) d\epsilon, \tag{1.31}$$

where ϵ_i are the energy eigenvalues of the protons and neutrons, and n_i are the population numbers of a given energy level. The distribution function $g(\epsilon)$ is defined by a smearing parameter γ,

$$g(\epsilon) = \frac{1}{\gamma\sqrt{\pi}} \Sigma_i n_i e^{\frac{-(\epsilon-\epsilon_i)^2}{\gamma^2}}. \tag{1.32}$$

Similarly, the pairing correction δP is derived by Bardeen-Cooper-Schrieffer theory [27]. Today, several additions to this approach have been made and various theoretical calculations have been performed. For example, the FRDM model allows for droplet compression. The WS4$^{\mathrm{RBF}}$ has been constructed to reproduce experimental values by adding the radial basis function correction (RBF) to the Weizsäcker-Skyrme (WS) model, which takes into account the isospin dependence of the model parameters and the specular correction from isospin symmetry. KTUY calculation is a phenomenological method that considers the nucleus as the basis of a sphere and the deformed nucleus as its spherical coordination mixture.

Microscopic methods

In addition to the macroscopic microscopic approach, purely microscopic methods have also been developed. The Hamiltonian H by the Hartree-Fock approximation describes the interactions between nuclei as the mean field V_{HF} produced by the nucleus and the interactions of any nucleus,

$$H^{\mathrm{HF}} = -\frac{\hbar^2}{2m}\Sigma_i \nabla_i^2 + \Sigma_i V_i^{\mathrm{HF}}. \tag{1.33}$$

In this method, the binding energy is evaluated as the sum of the energy functions solved by the Ritz variation method [28],

$$B^{\mathrm{SHF}} = E_{\mathrm{kine}} + E_{\mathrm{coulomb}} + E_{\mathrm{pair}} + E_{\mathrm{skyrme}} + E_{\mathrm{corr}}, \tag{1.34}$$

where the first four terms are kinetic, coulomb, and pairing energies and a correction term. E_{skyrme} is a term for considering phenomenological nucleon-nucleon interactions and is called the skyrme force. There are various versions that extend the skyrme force term, and a typical one used for mass model calculations is HFB.

1.4 Ion manipulation for low-energy RI

The ion manipulation techniques are used to handle low energy ions such as, stopping, transporting, thermalization and trapping. Especially for radioactive ions, it is important to efficiently handle ions, since the yields are generally not so high. The most common way to manipulate low-energy ions is by using a magnetic field and/or radiofrequency (RF) electric field. In our experimental setup, we use a gas catcher and multiple RF trap systems to manipulate ions.

1.4.1 Gas catchers

The gas catcher, also called a gas cell or gas-filled ion guide, was first used in the IGISOL method in JYFL [29]. A primary beam irradiated a target in the gas cell, and the reaction products were thermalized by the helium buffer gas and extracted by the gas flow. There were problems with space charge effects caused by high intensity primary beam. However, if the primary beam is preseparated by a separator one can minimize space charge effects. The separated and transported ions are decelerated and thermalized in a gas catcher filled with a noble gas, typically a Helium. The Helium gas is often chosen as a buffer gas because it has the highest first ionization potential among chemical elements. The thermalized ions are extracted by a combination of a direct current (DC) electric field and a gas flow or of DC

and RF electric fields in the gas cell. The extracted low-energy beam is sent to the high vacuum region where the experiment is performed.

1.4.2 RF carpet

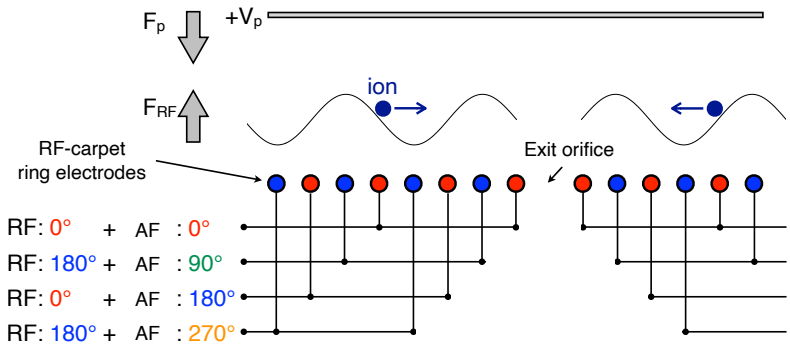

Figure 1.8: Conceptual view of RF carpet and ion surfing method. F_{RF} and F_{p} are the repelling force from the RF carpet and a pushing force, respectively. This figure taken from [30].

In experiments with unstable nuclei using an ion trap, the RI beam is thermalized and stopped in the gas cell, and then extracted as a low-energy radioactive ion beam. In order to quickly and efficiently extract ions from the gas cell, the transport of ions by electric field is effective. The radio-frequency ion guide method using an RF carpet has been widely used for this purpose.

An RF carpet is a type of RF trap that uses a non-uniformity electric field to trap ions. an RF voltage with a phase difference of 180 degrees is applied between adjacent electrodes as shown in Fig. 1.8. Four phase audio frequency (AF) signals are superimposed on the RF signal to produce a traveling wave that can transport ions radially along the carpet. The average force due to the RF electric field gradient formed by this is always directed away from the electrodes. This force acts as a barrier to the electrodes for the ions and they remain above the surface of the carpet. The strength of the ion barrier is determined by the balance between the force of the electrostatic field that pushes the ions toward the carpet and the repulsive force of the RF field that repels the ions.

The motion of an ion of mass m in a gas is determined by following equation

$$m\ddot{r} + \frac{e}{\mu}\dot{r} = -e\nabla\Phi(\boldsymbol{r}, t), \tag{1.35}$$

where $\mu = \mu_0 P_0/P$ is the mobility of ions, P_0 is the atmospheric pressure, μ_0 is the mobility of the ions under P_0 and Φ is the potential. If we let the relaxation time of velocity $\tau_v = v = \mu m/e$, then the equation becomes

$$m\ddot{r} + \frac{1}{\tau_v}\dot{r} + \frac{e}{m}\Phi = 0. \tag{1.36}$$

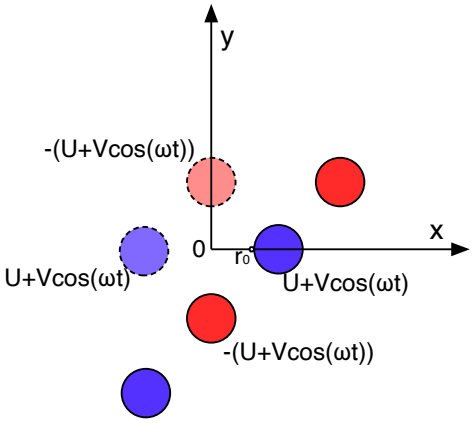

Figure 1.9: Conceptual view of virtual electrodes placed inside an RF ring electrodes.

The RF electric field of an RF carpet can be approximated as an RF quadrupole electric field by placing a virtual electrode inside the ring electrode, as shown in Fig. 1.9.

Then, the quadrupole potential Φ is approximated by

$$\nabla\phi(x,y,z,t) = \frac{\Phi_0(t)}{r_0^2}\phi(x,y,z,t) = \Phi_0(t)\frac{x^2-y^2}{r_0^2}, \tag{1.37}$$

where $\Phi_0(t) = 2(U + V\cos\omega t)$,

$$\nabla\phi(x,y,z,t) = \frac{\Phi_0(t)}{r_0^2}\begin{pmatrix} x \\ -y \end{pmatrix}. \tag{1.38}$$

The effective electric field is estimated by using the pseudo-potential in the quadrupole field as shown in Fig. 1.9. Divide the motion of an ion into a mean-motion part and a micro-vibration term,

$$\begin{aligned} \boldsymbol{r} &= \bar{\boldsymbol{r}} + \rho(t) && (1.39)\\ &= \bar{\boldsymbol{r}} + c\boldsymbol{E}_{\mathrm{RF}}(\boldsymbol{r})\cos(\omega t + \beta), && (1.40) \end{aligned}$$

where constant c is determined by substituting Eq. (1.40) for (1.36). Thus, micro-vibration term is expressed by

$$\rho(t) = -\frac{e}{m\omega}\frac{\boldsymbol{E}_{\mathrm{RF}}}{\sqrt{\omega^2+1/\tau_v^2}}\cos(\omega t+\beta), \tag{1.41}$$

$$\tan\beta = \frac{1}{\tau_v}. \tag{1.42}$$

The average force due to the RF electric field F is

$$\begin{aligned}\bar{\boldsymbol{F}}(\bar{\boldsymbol{r}}) &= e\langle \boldsymbol{E}_{\mathrm{RF}}(\boldsymbol{r})\cos\omega t + [\nabla|_{r-\bar{r}}\boldsymbol{E}_{\mathrm{RF}}(\boldsymbol{r})]\,\rho(t)\cos\omega t\rangle_{\text{time average}} \\ &= -\nabla\boldsymbol{E}_{\mathrm{RF}}^2(\bar{\boldsymbol{r}})\frac{e^2}{4m}\frac{1}{\omega^2+1/\tau_v^2}.\end{aligned} \tag{1.43}$$

For the average force, considering the case of vacuum and the case in gas is

$$\bar{\boldsymbol{F}}(\bar{\boldsymbol{r}}) = \begin{cases} -\nabla\boldsymbol{E}_{\mathrm{RF}}^2(\bar{\boldsymbol{r}})\frac{e^2}{4m\omega^2} = -e\nabla\Psi_{\text{pseued}} & \omega\tau_v \gg 1(\text{Vaccum}) \\ -\nabla\boldsymbol{E}_{\mathrm{RF}}^2(\bar{\boldsymbol{r}})\frac{e^2}{4m}r_v^2 = -e\nabla\omega^2 r_v^2\Psi_{\text{pseued}} & \omega\tau_v \ll 1(\text{Gas}). \end{cases} \tag{1.44}$$

The motion of ions due to the RF electric field is determined by the pseudo-potential Ψ_{pseued},

$$\Psi_{\text{pseued}} = \frac{e}{4m\omega^2}\boldsymbol{E}_{\mathrm{RF}}^2, \tag{1.45}$$

RF quadrupole field,

$$\phi = V_{\mathrm{RF}}\frac{x^2-y^2}{r_0}, \tag{1.46}$$

is used to described the electric field,

$$\boldsymbol{E}_{\mathrm{RF}}^2 = 4V_{\mathrm{RF}}^2\frac{r^2}{r_0^2}. \tag{1.47}$$

Thus, the average force due to the RF electric field in the gas can be expressed by

$$\bar{\boldsymbol{F}}(\bar{\boldsymbol{r}}) = -\frac{8V_{\mathrm{F}}^2}{r_0^3}\frac{r}{r_0}\frac{e^2}{4m}r_v^2 = -2m\mu^2\frac{V_{\mathrm{RF}}^2}{r_0^3}\frac{r}{r_0}. \tag{1.48}$$

From the equation, the closer the ion is to the electrode, the greater the repulsion force is, the more it is pulled away from the electrode. The force acting on the ions for a given RF electric field becomes stronger for heavier ions, and weaker at higher gas pressures. Also, the use of narrowly spaced electrodes is expected to have a significant effect.

Traditionally, the transport of ions at the surface of an RF carpet has been performed by an electrostatic gradient formed by a DC voltage superimposed on the RF voltage. This limits the ion transport rate and increases the extraction time, which makes it difficult to apply to short-live radioactive nuclei. The ion surfing method was developed to solve this problem [30, 31].

Ion surfing methods

The ion surfing method uses a traveling wave electric potential instead of a static potential gradient to transport ions. By superimposing an AF voltage with a phase difference of 90 degrees between neighboring electrodes, a potential traveling wave is formed on the ion barrier as shown in Fig. 1.8. The ions on the RF carpet are transported in waves by the traveling wave. The speed of ion transport is determined by the amplitude and speed of the traveling wave, and the speed of the traveling wave is also determined by the frequency of the AF, the number of phases, and the pitch of the electrodes in the RF carpet. If the amplitude of the traveling wave is small, the ions will slip out of the traveling wave and not be transported properly. On the other hand, if the amplitude is large, the traveling wave becomes too deep and some ions are lost due to collision with the carpet electrodes. If the amplitude of the traveling wave is appropriate, the rate of ion transport will coincide with the rate of the traveling wave. The AF signals applied to form the traveling wave at the N electrodes is written as

$$V_{\mathrm{AF,i}} = V_{\mathrm{AF}} \cdot \cos(\omega_{\mathrm{AF}} \cdot t + 2\pi \frac{i}{N} + \phi_{\mathrm{AF}}). \tag{1.49}$$

The AF amplitude V_{AF} changes in phase by $2\pi/N$ between electrodes. The wavelength of the traveling wave is written as

$$\lambda = N \cdot a, \tag{1.50}$$

where the angular frequency of the AF voltage be ω_{AF}, the speed of the traveling wave can be expressed by

$$v_{\mathrm{wave}} = \frac{1}{2\pi}\omega_{\mathrm{AF}} \cdot \lambda = \frac{Na}{2\pi}\omega_{\mathrm{AF}}. \tag{1.51}$$

Assuming that the potential surface is sinusoidally fluctuating, the amplitude of the potential traveling wave decreases exponentially with respect to the distance y from the surface of the electrode. The two-dimensional oscillations of the V_{AF} are expressed as Eq. (1.52),

$$V_{\mathrm{AF}}(x, y) = V_{\mathrm{AF}} \cdot \cos\left(\frac{2\pi}{\lambda}(v_{\mathrm{wave}} \cdot t - x)\right) e^{-2\pi(y/a)}. \tag{1.52}$$

1.4.3 RF multipole ion guide

The multipole ion guide technique is used for ion transport and ion trapping. By applying radio-frequency signals with a 180-degree phase difference to adjacent electrode rods, the ions are radially confined in an ion guide and their motion is described as oscillations in a pseudo-potential.

In the cylindrical coordinate system (r, θ, z), the potential of a two-dimensional $2N$-pole field which is formed by rods (Fig. 1.10, left) which are uniformly distributed along a circle of radius r_0 around z-axis with an RF voltage $\pm V \cos \omega t$ applied between the adjacent rods is written as

$$\begin{aligned} \Phi &= \phi_0 \cos \omega t \\ &= \left(\frac{r}{r_0}\right)^2 \cos(N\theta) V \cos \omega t, \end{aligned} \tag{1.53}$$

where,

$$\begin{aligned} \boldsymbol{r} &= \bar{\boldsymbol{r}} + \bar{\rho}(t) \\ &= \bar{\boldsymbol{r}} + \rho_0 \cos \omega t. \end{aligned} \tag{1.54}$$

Then, the equation of motion can be described as

$$m\ddot{\boldsymbol{r}} = -e\nabla\Phi, \tag{1.55}$$

then,

$$\rho_0 = \frac{e}{m\omega^2}\nabla\phi_0. \tag{1.56}$$

The average force that ions receive is

$$\begin{aligned} \bar{\boldsymbol{F}}(\bar{\boldsymbol{r}}) &= -e\langle \nabla\phi(\bar{\boldsymbol{r}}) + [\nabla|_{r-\bar{r}}(\nabla\phi_0)]\, \bar{\rho}(t) \cos \omega t \rangle_{\text{time average}} \\ &= -\frac{e^2}{4m\omega^2}\nabla|\nabla\phi_0^2|^2. \end{aligned} \tag{1.57}$$

The ion motion then follows from the pseudopotential

$$\Psi_{\text{pseued}} = \frac{e}{4m\omega^2}|\nabla\phi_0(\boldsymbol{r_0})|^2, \tag{1.58}$$

then,

$$\Psi_{\text{pseued}} = \frac{eN^2}{4m\omega^2}\left(\frac{V}{r_0}\right)^2\left(\frac{r}{r_0}\right)^{2(N-1)}. \tag{1.59}$$

The right side of Fig. 1.10 shows the pseudo-potential for $N = 2$, 3 and 4 corresponding to quadrupole, sextupole and octupole, respectively.

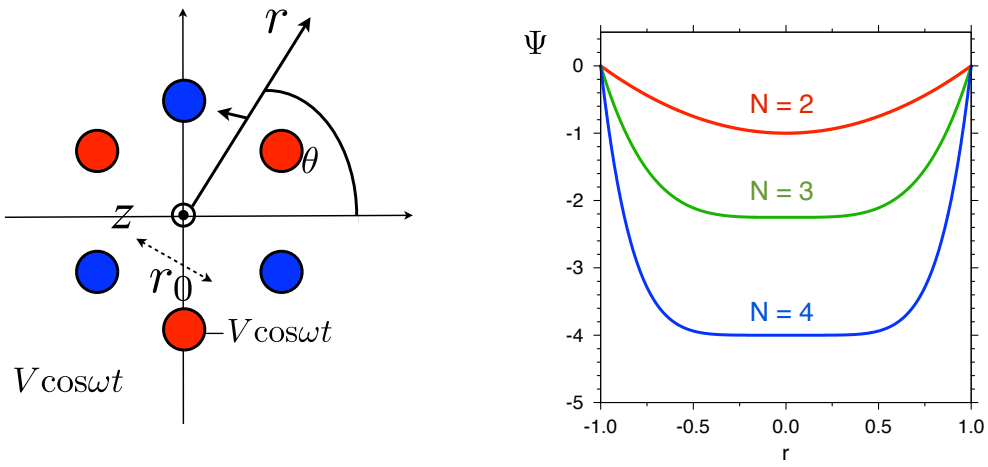

Figure 1.10: (left) Cross section of a sextupole ion guide within the cylindrical coordinate system. (right) Pseudo-potential of multipole field with quadrupole (N=2), sextupole (N=3) and octupole (N=4).

1.4.4 RF quadrupole ion trap and mass separator

The potential of the linear quadrupole ion trap can be expressed by

$$\Phi(x, y, z, t) = \Phi_0(t) = (U - V\cos\omega t)\frac{x^2 - y^2}{2r_0^2}, \tag{1.60}$$

the equation of motion for the ions of mass m and charge ze in a trap can be expressed by Mathieu's equation,

$$\frac{d^2u}{dr^2} + (a_u - q_u\cos 2\tau)u = 0, \tag{1.61}$$

where u indicates each axis. Assuming that the ion is singly charged ($q = e$), the equation of motion are

$$\begin{aligned} \frac{d^2x}{dr^2} + \frac{e}{m_i r_o^2}(U - V\cos\omega t)x &= 0, \\ \frac{d^2y}{dr^2} + \frac{e}{m_i r_o^2}(U - V\cos\omega t)y &= 0, \\ \frac{d^2z}{dr^2} &= 0, \end{aligned} \tag{1.62}$$

where m_i is mass of ion, r_0 is the distance from center of the ion trap to the rod electrode. The solution to this equation are described,

$$r = \frac{\Omega t}{2}, \qquad a_x = -a_y = \frac{4zeU}{mr_0^2\Omega^2}, \qquad q_x = -q_y = \frac{2zeV}{mr_0^2\Omega^2}. \tag{1.63}$$

For a given U, V, and Ω combination, we obtain a stable region of ions in any m/z range passing through the quadrupole. Figure 1.11 (left) shows a diagram with overlapping stability regions for the motions in the yz- and yz- planes, and a detailed view of the upper half of the first stable region is shown in Fig. 1.11 (right). If a/q is set to 0.237/0.706=0.336, their is stable motion in the xy-plane at only one point in the diagram – the vertex. By holding q constant and decreasing a, i.e. decreasing the ratio of U to V, the range of m/z with which ions can pass through the quadrupole at the same time can be increased. In other words, the quadrupole ion trap can be used as a mass filter.

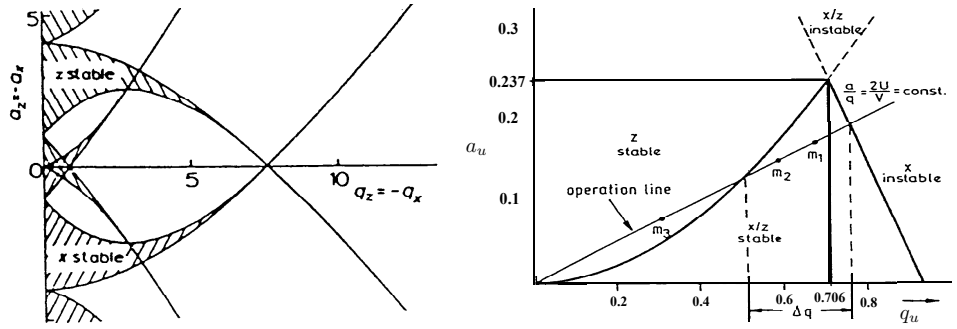

Figure 1.11: (left) The stability diagram for the two-dimensional quadrupole field. (right) The first stable region of diagram for the quadrupole field.

1.5 Mass measurement techniques

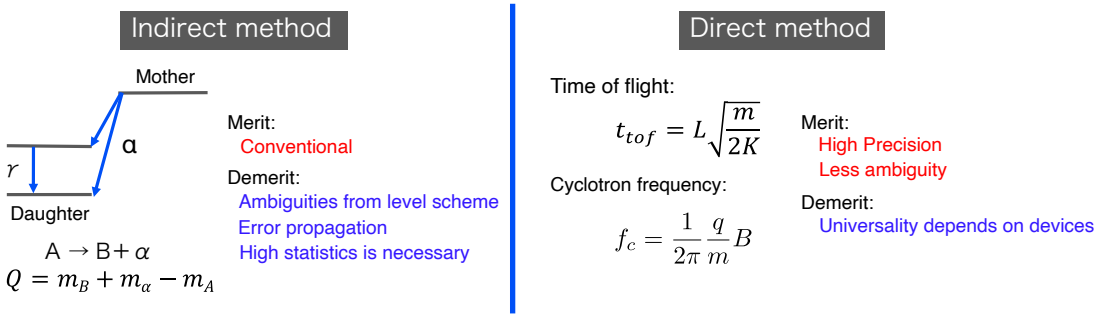

Figure 1.12: Comparison of mass measurement techniques. (left) Indirect method, (right) direct method.

In general, there are two methods for measuring the mass of nuclei: indirect and direct methods, as shown in Fig. 1.12.

1.5.1 Indirect mass measurements

The indirect mass measurement relies upon the Q-values of nuclear reactions and radioactive decay, as shown in Fig. 1.12. The Q-value for nuclear decay provides the mass difference between the parent and daughter nuclei. In order to obtain a mass value from nuclear decay, the radioactive isotopes must be linked to a known mass. This technique is a historically common method. However, in the case of unstable isotopes, the determination of the final mass may involve a long chain decay, which may lead to the accumulation of error from each subsequent decay.

The remarkable instance of a noteworthy result is the direct mass measurement of ^{150}Ho by Penning-trap mass spectrometer at CERN/ISOLDE. It was found that the indirect measurements result had an 800 keV discrepancy as β-decay spectrometry studies had misidentified the excited and ground states [32, 33]. This demonstrates the importance of direct mass measurements.

1.5.2 Direct mass measurements

The history of direct mass measurement of nuclei began with a spectrometer developed by J.J. Thomson in the 1910s. Despite a poor mass resolving power, about R_m ~20, isotopes of Neon with A=20 and 22 were identified [34]. Later, his student Aston developed a velocity focusing mass spectrometer that achieved a mass resolving power of R_m ~600. Their experiments revealed the presence of isotopes in most of the known elements.

Subsequent developments would continue to improve the mass resolution and sensitivity of mass spectrometers. In the early 1970s, R. Klapisch et al., were the first to combine a classical mass spectrometer with an accelerator at the Proton Synchrotron (PS) at CERN to measure the atomic masses of unstable isotopes [35, 36]. Their measurements provided the first evidence that the magic number $N = 20$ disappears for Na isotopes. Today, direct mass measurements combine some combination of electric field and magnetic field, time-of-flight, frequency determination, and magnetic rigidity. Such mass spectrographs and mass spectrometers exist worldwide to make mass measurements of exotic nuclei.

The magnetic sector type mass spectrometers were commercialized in the 1950s, paving the way for advances in organic chemistry by mass spectrometry. The principle of a magnetic sector mass spectrometer is described by the Lorentz force F_L , which depends on the velocity of the ion v and the magnetic field B, which is orthogonal to v, and the charge of the ion q,

$$F_L = qvB(\sin\alpha), \tag{1.64}$$

where α is the angle between v and B. An ion of mass m_i and charge q flying at velocity v in a direction perpendicular to a uniform magnetic field draws a circular orbit of radius r_m such that the Lorentz force F_L and centrifugal force F_c are balanced:

$$F_L = qvB = \frac{m_i v^2}{r_m} = F_c, \tag{1.65}$$

$$r_m = \frac{m_i v}{qB}. \tag{1.66}$$

This equation is the principle of the magnetic sector type mass spectrometer. That is, the radius r_m is proportional to an ion's m/q. Since the mass resolving power of a magnetic sector mass spectrometer is limited by the energy spread, they are commonly used in combination with an electrostatic sector mass spectrometer to reduce the energy dispersion. The relationship between the electrostatic force F_e and the centrifugal force F_c can be expressed as

$$F_e = qE = \frac{m_i v^2}{r_e} = F_c, \tag{1.67}$$

$$r_e = \frac{m_i v^2}{qE}, \tag{1.68}$$

where E is the strength of the electric field and r_e is the radius of the electrostatics analyzer (ESA). From this equation, it can be seen that ESA act

as energy dispersers. Combining these converging effects of magnetic and electric fields, the double-focusing mass spectrometer was developed. The typical ESA is known as the Mattauch-Herzog arrangement. By combination with the electric field, the mass resolving power can be improved by a factor of 10 compared to a purely magnetic field mass analyzer, achieving a resolution of $R_m \gtrsim 10000$. The Mattauch-Herzog configuration is still used for analyzers such as those for isotope ratio mass spectrometry (IR-MS).

Recently, an attempt has been made to apply this double focusing mass spectrometer to identify the mass number A of the superheavy nuclei at the Lawrence Berkeley National Laboratory (LBNL). The primary beam and the evaporation residues are separated by the Berkeley Gas-filled Separator (BGS) and transported to the focal plane chamber. Where the ions thermalized in the gas catcher, are then transported into the low background area behind the wall by the multiple RF trap systems. The ions are then mass separated by a system named FIONA (For the Identification Of Nuclide A) [37]. FIONA uses unbalanced vertical electric and magnetic fields to cause ions to move in trochoidal orbits. The equation of motion for a charged particle of mass m and charge Ze passing through a Wien filter with an electric field E and a magnetic field B can be expressed as

$$x = a\omega t + \frac{v\sin(\theta)}{\bar{\omega}}(1-\cos(\omega t)) - \left(a - \frac{v\cos(\theta)}{\omega}\right) sin(\bar{\omega}t), \tag{1.69}$$

$$y = \frac{v\sin(\theta)}{\bar{\omega}}\sin(\bar{\omega}t) + \left(a - \frac{v\cot(\theta)}{\omega}\right)(1-\cos(\omega t)), \tag{1.70}$$

where v is the initial velocity in the $x-y$ plane perpendicular to the magnetic field B, θ is the angle between x-axis and v, ω and a are defined by the relations $\bar{\omega} = ZeB/m$ and $a = mE/ZeB^2$. The pitch of each trochoid is almost directly related to the A/q of the traveling ions. Therefore, neighboring isotopes can be separated based on differences in A/q ratios. They performed decay chain measurements to identify the mass number of ^{288}Mc and ^{284}Nh produced by the ^{243}Am(^{48}Ca, 3n) reaction with a mass resolving power of $R_m \sim 250$ [38]. Furthermore, they have successfully identified a new neutron deficient isotope of ^{244}Md produced by the ^{209}Bi(^{40}Ar, $5n$) reaction [39]. The FIONA is not expected to have a high mass resolving power, therefore cannot be used to identify the atomic number Z. Its strength is in cases where the evaporation channel is clear, such as the cold fusion reactions. Although this is not strictly a mass measurement, it is an approach to superheavy nuclei that has received much attention as an application of mass spectrometry techniques.

SPEG at GANIL and TOFI at LANL are in-flight mass spectrometers that measure mass by time-of-flight and magnetic rigidity, as determined by

the equation

$$B\rho = \frac{\gamma m_0 v}{q}. \tag{1.71}$$

Despite a low mass resolving power of $R_m \sim 10^4$, they can measure short lived nuclei of the order $T_{1/2} \sim 1\mu s$, and can measure the masses of unstable nuclei far from the valley of stability.

One way to try to increase mass resolving power by extending the flight path is to use a storage ring such as the experimental storage ring (ESR) at GSI [40]. When operating in isochronous mass spectrometry (ISM) mode [41], the revolution time of the ions orbiting in the ESR is recorded and the mass is determined from the time-of-flight ratio to the reference ion.

Despite the fast measurement speed of about 10 μs, it achieves a mass resolving power of $R_m \sim 10^5$. This method is still used for mass measurement of short-lived neutron-rich nuclei. Another method used in a storage ring is to use cold electrons to cool the ions orbiting in the ring and determine the mass from the orbital period of the ions using the Schottky method, so-called Schottky mass spectrometry (SMS) [42]. Although this method can increase the mass resolving power to $R_m \sim 10^6$, it requires thousands of ions for the measurement and the applicable half-life is limited to $T_{1/2}$ >5 s due to the long cooling time.

In recent years, the most accurate method of measuring atomic mass has been Penning trap mass spectrometry (PTMS). Relative mass uncertainty can reach 10^{-12} [43] for stable nuclei and 10^{-9} for unstable nuclei. The PTMS uses a strong, uniform axial magnetic field to confine particles radially and a quadrupole electric field to confine particles axially. The cyclotron frequency, f_c, of an ion trapped in a magnetic field can be measured and the atomic mass determined from

$$f_c = \frac{1}{2\pi}\frac{q}{m}B, \quad \delta f_c = 1/(\sqrt{N} \cdot t_{\mathrm{obs}}), \tag{1.72}$$

where N is the number of detected ions and t_{obs} is the measurement duration. Because of the required duration for a high-precision frequency measurement, it is suitable for measurements of nuclei relatively long lifetimes down to about 100 ms. As the frequency determination requires at least several tens of ions, the technique is not amenable to the lowest-yield ions.

Penning traps have been installed at RI beam facilities around the world. The first PTMS for rare isotopes, ISOLTRAP, was installed at the ISOLDE facility at CERN [44] to perform high-precision mass measurements of ions produced by ISOL. Following ISOLTRAP, Penning trap were installed at several other facilities, such as JYFLTRAP in Jyväskylä [45], CPT at Argonne National Laboratory [46], LEBIT at NSCL/MSU [47], and SHIPTRAP at GSI [48].

MRTOF-MS

The multi-reflection time-of-flight mass spectrograph (MRTOF-MS) was invented nearly 30 years ago for general purpose mass measurements [49]. Prior to 2015, the development and usage of such devices for mass measurements were reported by the laboratories ISOLDE in Switzerland [50], RIKEN in Japan [51], and GSI in Germany [52], The construction and commissioning of MRTOF-MS has since spread to other laboratories such as TRIUMF in Canada [53], GANIL in France [54], Argonne in USA [55], and Lanzhou in China [56], while plans for future implementations have been proposed at IGISOL in Finland [57], and the future facility RAON in South Korea [58].

The mass resolving power of a time-of-flight mass spectrometer can be explained by the relationship between the time-of-flight (TOF) t and the width of TOF, Δt, from the detected ion distribution as

$$R_m = \frac{t}{2\Delta t}. \tag{1.73}$$

To achieve high mass resolving power in TOF mass spectrometry, the width Δt must be as narrow as possible compared to t, and a long flight path is also desirable. Solutions to these requirements have been devised such as storage rings [59] described as above, figure-eight-shaped multi-turn mass spectrometers [60], and MRTOF-MS. The MRTOF-MS device consists of at least two electrostatic ion mirrors that can reflect ions back and forth and a field-free drift region to provide a long flight path. Initial conceptions of MRTOF-MS had a U-shaped configuration consisting of three mirrors, however the transmission efficiency decreased due to optical aberrations as the number of revolutions increased [61]. In order to avoid this optical aberration issue, current MRTOF-MS instruments use a pair of rotationally symmetric, coaxial mirror electrodes [62].

The difference in TOF between two ions of different masses traveling on the same flight path with the same kinetic energy depends only on the square root of their mass ratio. In the actual measurement, the measured TOF, t, which is the measured TOF, must contain an additional systematic offset t_0 to account for the imperfect synchronization between the onset of the ion's motion and the start of the measurement clock,

$$t = (a + b \cdot \ell)\sqrt{m} + t_0, \tag{1.74}$$

where ℓ is the number of laps an ion travels between mirrors, and a and b are constants related to the length of a single non-reflective flight path and total flight path, respectively. The part of the first term enclosed in parentheses depends only on the ion energy and can be treated as a constant among

ions making the same number of laps. By determining the value of offset t_0 independently, the mass of a given nucleus can be determined from a single reference ion,

$$m = \left(\frac{t - t_0}{t_{ref} - t_0} \right)^2 m_{ref} = \rho^2 m_{ref}, \tag{1.75}$$

where ρ is the ratio of the time-of-flight of the analyte ion to the reference ion.

The MRTOF-MS uses electrostatic ion mirrors that reflect the ions, minimizing their time spread and allowing for a long flight path. Designing the shape of the mirror potential to cancel out the energy dispersion of the ions, energy isochronous conditions can be achieved and mass resolving power can be maximized. A conceptual diagram of the energy isochronous behavior is shown in the lower part of Fig. 1.13. According to the potential gradient in each mirror, the higher-energy ions travel a slightly longer path than the lower-energy ions, removing the energy dependence from the ion's TOF.

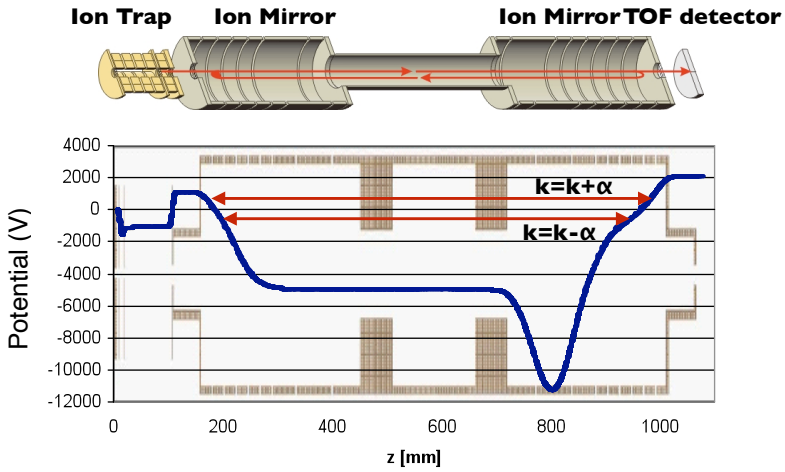

Figure 1.13: (Upper panel) Schematic view of MRTOF-MS, it consist of two ion mirror and ion trap and detector. (Lower panel) Conceptual view of energy isotonicity in the MRTOF-MS.

The MRTOF has an optimal lap number that maximizes the mass resolving power for the configuration and setting. When the number of lap exceeds the optimal value, the time spread increases and the mass resolving power decreases. This is similar to the spatial divergence of an optical lens. The dependence of the mass resolving power on the lap numbers is shown in Fig. 1.14. The MRTOF-MS is a powerful mass measurement device with

a short processing time of tens of milliseconds or less, and capable of high mass resolving power.

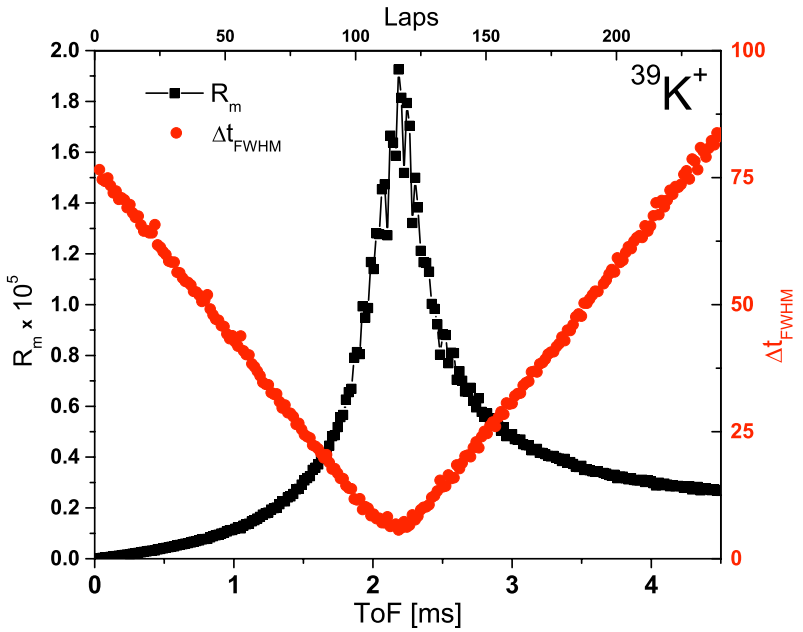

Figure 1.14: Scan of the lap number to determine number of laps at which the ions achieve a time focus. Number of laps are indicated at the top, while TOF is indicated along the bottom. In this case, $^{39}K^{+}$ ion is focusing at 125 laps. This figure taken from [63].

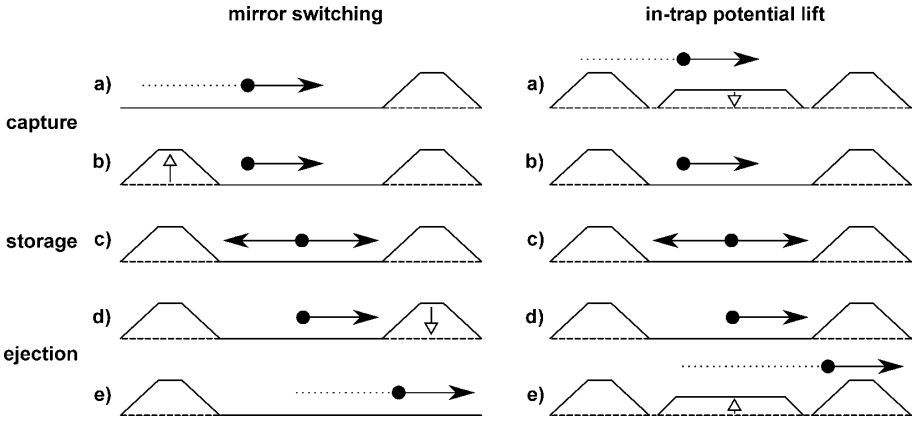

Figure 1.15: Comparison of mirror switching methods and in-trap potential lift method operation modes of MRTOF-MS. In the mirror switching methods, the potential of the left and right mirrors are changed to allow to inject and eject of ions. In the in-trap potential lift method, the left and right mirror potentials are fixed, and the potential of center region is increased or decreased to move ions in and out. This figure taken from [64].

There are two ways to manipulate ions by MRTOF-MS: mirror switching and in-trap potential lift. These methods are shown schematically in Fig. 1.15. The in-trap potential lift does not require a change in mirror potential during the measurement. This is effective and efficient for both high resolution and stability. However, the in-trap potential lift method has the disadvantage of a narrow mass bandwidth. The acceptance time window t_{lift} of the in-trap potential lift technique can be evaluated as

$$t_{\mathrm{lift}} = \frac{l_{\mathrm{lift}}}{v_{\mathrm{ion}}} = l_{\mathrm{lift}} \sqrt{\frac{m_{\mathrm{ion}}}{2E_{\mathrm{transfer}}}}, \tag{1.76}$$

where v_{ion} and m_{ion} are the velocity and mass of the moving ions and l_{lift} is the length of the drift region, respectively. Assuming $m_{\mathrm{ion}} = 60$ u, $E_{\mathrm{transfer}} = 5$ keV, and $l_{\mathrm{lift}} = 30$ cm, we would calculate $t_{\mathrm{lift}} = 2.4$ μsec. This time window can cover a mass range of $\Delta m/m \approx 0.1\%$ in the typical case of a total TOF of 5 ms.

The mirror-switching technique, conversely, allows for measurements with wide mass bandwidth. Consider the situation where two ions of differing masses $m_1 \neq m_2$ have the same TOF,

$$(\zeta + \ell_1) b \sqrt{m_1} = [\zeta + (\ell_1 + \Delta\ell)] b \sqrt{m_2}, \tag{1.77}$$

where $\zeta = a/b$, and $\Delta\ell$ is the difference in lap numbers. The mass bandwidth is defined as the maximum mass range over which the same lap number can

take place simultaneously, which corresponds to a limit of $|\Delta\ell| \to 1$. Thus, by rewriting m_2 as $m_1 + \Delta m$, we can find the mass bandwidth by solving Eq. (1.77) in the limit of $|\Delta\ell| \to 1$ [63],

$$\frac{\Delta m}{m} = \frac{2(\zeta + \ell_m) + 1}{(\zeta + \ell_m)^2}, \quad \ell_m = \frac{\sqrt{m_2}}{\sqrt{m_2} - \sqrt{m_1}} - \zeta. \tag{1.78}$$

In the case of Fig. 1.14 the optimal lap number is about 125, so the mass bandwidth can be estimated to be $\Delta m/m$ =1.6%. When the ions are ejected from the MRTOF, the potential of the mirror is lowered to allow the ions to pass through the mirror into the detector (processes (d) and (e) in mirror switching of Fig. 1.15). The effective mass bandwidth has been confirmed by offline experiments to be around 60% of the upper limit for $A/q \sim 40$ ions [63].

Now, let us introduce three facilities that have pioneered the use of MRTOF equipment.

a)MRTOF at ISOLDE/CERN

ISOLTRAP at ISOLDE/CERN was the first facility developed for high-precision mass measurements of short-lived nuclei. The online facility ISOLDE produces RI by proton-induced fission reactions in a thick UO_2 target using a 1.4 GeV proton beam. The unstable nuclei generated are ionized by various methods, such as a plasma source, high-temperature surface ionization, and resonant laser ionization. The ions are accelerated and transported through the isotope separator online (ISOL) and then delivered to ISOLTRAP as a 30 keV/q continuous ion beam. These ions are decelerated, thermalized, and trapped in an RF quadrupole (RFQ) cooler-buncher and transferred to the MRTOF as ion bunches (see Fig. 1.16).

The MRTOF at ISOLDE uses the in-trap potential lift method. This method is not suitable for wide mass bandwidth measurements, however it is well suited for narrow mass bandwidth measurements, making it well-suited for combination with the ISOL method. The MRTOF system at ISOLDE was initially developed as an isobar separator for the Penning trap system. However, for short-lived, low-yield nuclei that cannot be measured by the Penning trap, MRTOF has been used for mass measurement in standalone operation.

The atomic masses of the neutron rich isotopes $^{51-54}$Ca were measured [65] by the ISOLTRAP group. In the case of ^{51,52}Ca, the MRTOF was used as an isobar separator for the Penning trap. In the case of the ^{53,54}Ca isotopes, the low production rate and short lifetime in addition to the large contamination by ^{53,54}Cr isobars, made it impossible to measure by PTMS. Therefore, the atomic masses of these nuclides were determined by using the MRTOF as an independently mass spectrometer.

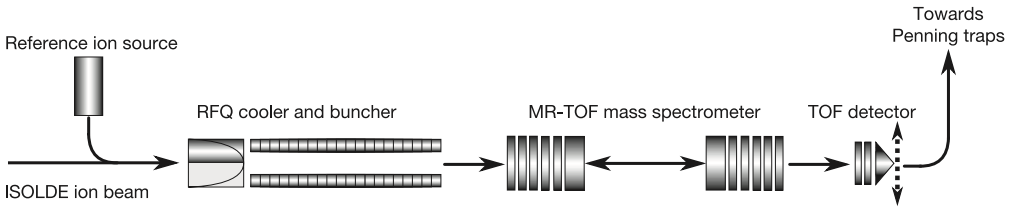

Figure 1.16: Schematic view of the MRTOF-MS at ISOLDE/CERN. This figure taken from [65].

b)MRTOF at FAIR/GSI

The MRTOF at GSI [66] was developed as both a mass spectrometer and isobar separator for the low-energy branch of the Super FRS [67], which uses a superconducting magnet to separate exotic nuclear beams produced by nuclear spallation and fission of ^{238}U beams at ≈1 GeV/nucleon. The MRTOF at GSI uses a triple injection trap system that allows the ion cooling and ion release process to take place in less than a few milliseconds with a duty cycle of about 100%. A post-analyzer reflectron is installed at the exit of the GSI MRTOF to ensure the final time focus. (See Fig. 1.17).

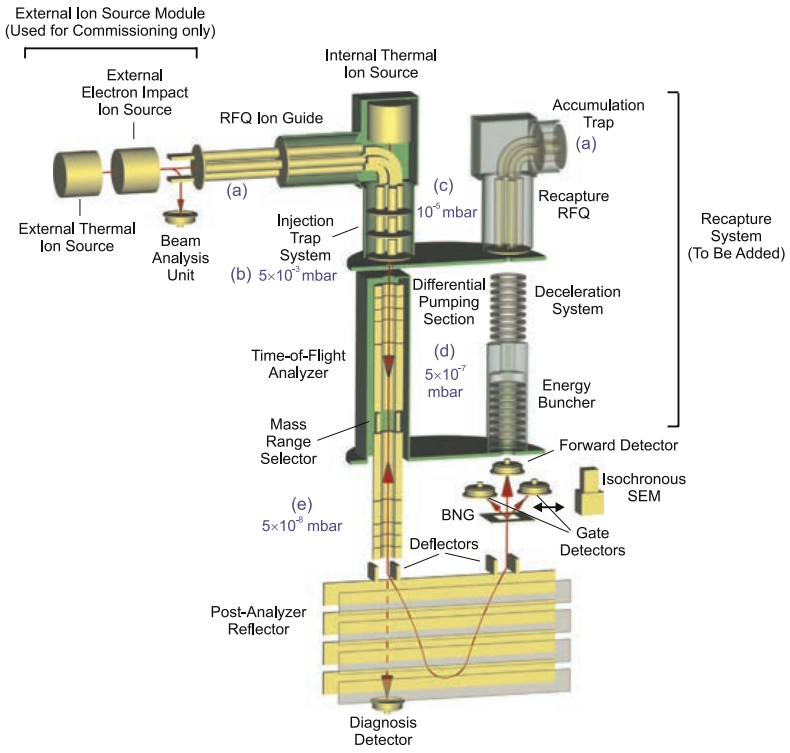

Figure 1.17: Schematic view of the MRTOF-MS at FAIR/GSI. This figure taken from [67].

c)MRTOF at RIKEN

At the RIKEN Nishina Center for Accelerator-Based Science, the MRTOF has been combined with several instruments such as the in-flight RI beam separator BigRIPS [68], the gas-filled recoil ion separator GARIS-II [69], and the KEK isotope separator KISS [70]. This enables us to measure the masses of unstable nuclei produced by various production methods such as spallation, fusion, and multinucleon transfer reactions. The MRTOF coupled with GARIS-II, called the SHE-Mass facility, will be explained in Section 1.6.

The MRTOF devices developed at RIKEN all use the mirror switching method. This enables simultaneous mass measurement over a wide range. The ability to perform wide mass bandwidth measurements makes highly effective utilization of the RI beams available.

In the initial commissioning of the MRTOF system at RIKEN, the ^{8}Li produced by fragmentation reaction of a ^{13}C beam at 100 MeV/n was transported by an RF gas cell ion guide behind the fragment separator RIPS. Ions from the gas cell were accumulated in an RF ion trap system and transferred

to an MRTOF system whereby mass measurements were performed. A relative mass uncertainty of 6.6×10^{-7} [51] was achieved for ^{8}Li. The initial setup of the MRTOF-MS at RIKEN shown in Fig. 1.18.

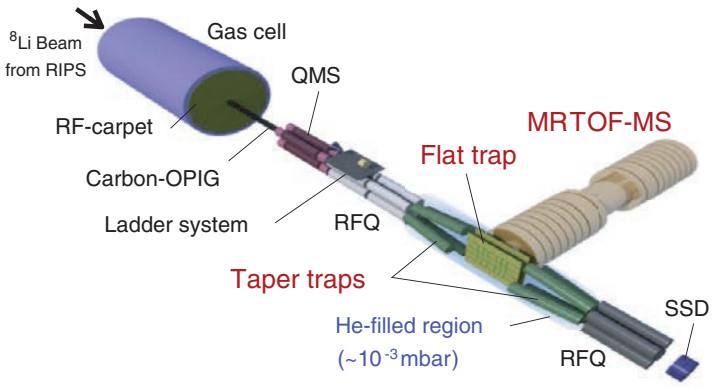

Figure 1.18: Schematic view of the initial setup of the MRTOF-MS at RIKEN. This figure taken from [51].

1.6 SHE-Mass facility

Following the success of the MRTOF system coupled to RIPS, the SHE-Mass facility was constructed, which coupled the MRTOF with GARIS-II. This system was developed to measure the masses of the relatively low-energy products produced by fusion evaporation reactions, especially for the masses of superheavy elements.

The evaporation residues transported by GARIS-II are thermalized in a cryogenic gas cell, and extracted by a traveling wave RF carpet. The extracted ions are transported by RF multipole ion guides to a "flat trap" and injected into the MRTOF. Because of space constraints in the initial SHE-Mass facility, trapped ions were transported to a room below GARIS-II for re-trapping and mass analysis by MRTOF-MS (see Fig. 1.19).

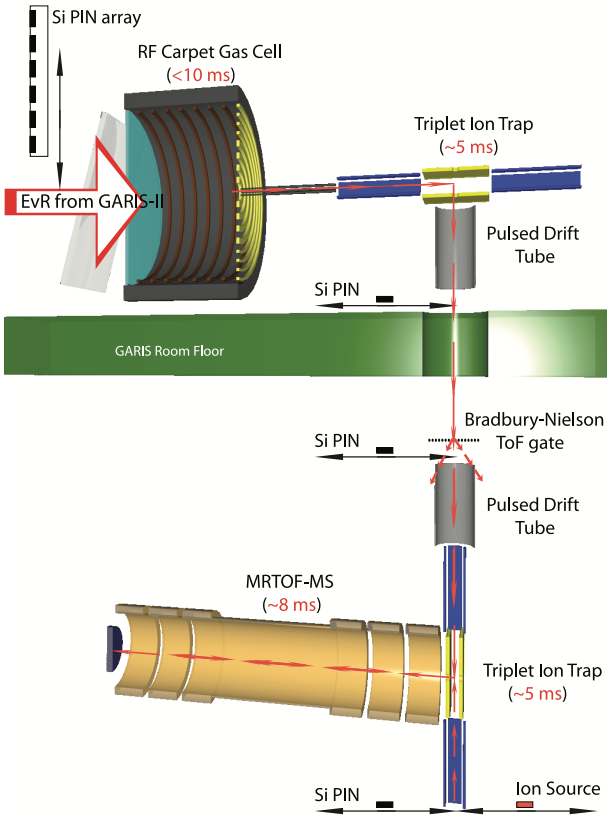

Figure 1.19: Schematic view of SHE-Mass facility. This figure taken from [71].

1.6.1 GARIS-II

In a fusion reaction, the evaporation residues are emitted in the same direction as the primary beam. Therefore, a device capable of separating these reaction products from the primary beam is required. Because the synthesized ions are heavy elements with large masses, having a large angular spread in the target and gas, a recoil separator with large acceptance is required. There are two major types of recoil separators currently in use around the world: velocity filters and gas-filled recoil separators.

The so-called velocity separator, such as SHIP at GSI, operates under vacuum. They use magnetic and electrostatic field combinations to guide only particles of a specific velocity to the focal plane, independent of the charge state of the ions. Evaporation residues have a charge-state distribution, with the velocity being a function of the charge state. In the case of a

velocity separator, only evaporation residues with a specific charge state are transported to the focal plane, greatly limiting the transmission efficiency.

A gas-filled recoil separator, such as GARIS-II at RIKEN [69] can achieve a higher efficiency. By filling the particle's orbit with a dilute He gas in addition to a static magnetic field, charge exchange between ions and He gas causes the particle to converge to an average equilibrium charge $\bar{q}$ that is proportional to the product of the incident velocity and the cube root of the atomic number Z, as described in Eqs. (1.79) and (1.80),

$$\bar{q} = 0.625 \times \frac{v}{v_0} \times Z^{1/3} \quad (9.1 \leq \frac{v}{v_0} \leq 19.1, Z \geq 82), \tag{1.79}$$

$$\bar{q} = 0.242 \times \frac{v}{v_0} \times Z^{1/3} + 2.19 \quad (4.6 \leq \frac{v}{v_0} \leq 6.0, Z \geq 102), \tag{1.80}$$

where v is the velocity of ions, v_0 is the Bohr velocity $v_0 = (c/137)$. In a dipole magnet field, the trajectory of a particle is proportional to the product of velocity and mass number and inversely proportional to the charge, as shown by the magnetic rigidity (Eq. (1.81)),

$$B\rho = 0.0227 \times \frac{(v/v_0)A}{q}. \tag{1.81}$$

Substituting the equilibrium charge into this equation, we find the magnetic rigidity depends only on the atomic number and mass, as shown in Eq. 1.82. Thus, gas-filled separators can separate and focus ions regardless of their initial charges and velocities, and thus have a high transmission efficiency.

$$B\rho = 0.0362 \times \frac{A}{Z^{1/3}} \tag{1.82}$$

The GARIS-II consists of a Q_v-D-Q_h-Q_v-D magnet configuration with two dipole magnets (D1 and D2) and three quadrupole magnets (Q1-Q3), as shown in Fig. 1.20. The initial GARIS [72] has a D-Q-Q-D magnet configuration; GARIS-II has an additional Q_v in the fore to expand the vertical acceptance. Therefore, it is optimized for reactions, such as hot fusion reactions, where the products are slow and the angular spread is large due to multiple scattering. The primary beam particles are deflected and separated from other particles by D1 and stopped by a tantalum beam dump. The vacuum chamber of GARIS-II is filled with 70 Pa He gas in typical operation. A differential pumping system installed upstream from the target chamber maintains high vacuum in the accelerator beam line. The focal plane chamber is maintained at high vacuum, and separated from the upstream beam line, by a 0.5 μm Mylar foil.

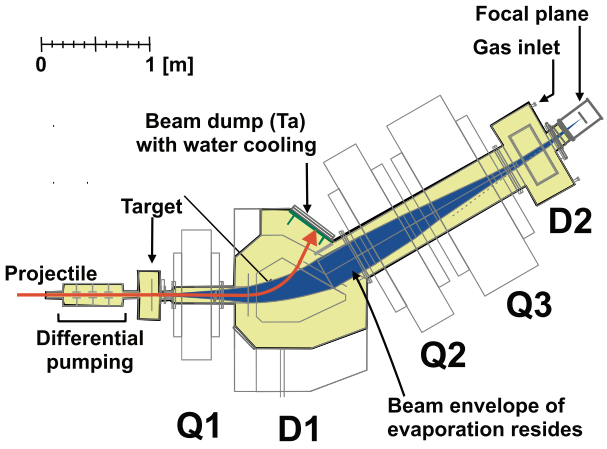

Figure 1.20: A schematic view of GARIS-II. Yellow area indicates the dilute He Gas filled region. This figure taken from [69].

1.6.2 Cryogenic gas-cell

The analyte ions separated and efficiently transported by GARIS-II are injected into a gas cell in the focal plane. For efficient measurements, the background rate of stable ions must be suppressed. The main source of stable background ions is charge exchange with contaminants in the gas cell. Despite using 99.99995% high-purity helium gas, sufficient contaminants may exist within the gas cell to produce large amounts of stable ion background. To reduce this stable ion background, we have designed the gas cell to operate at cryogenic temperatures, down to 50 K. At sufficiently low temperatures, contaminants in the gas are expected to freeze out.

The charge state of the extracted ions is very important in determining the frequency and amplitude of the RF voltages. Although some factors are still unclear, studies of the charge states of the particles drawn over two years of experiments have shown that many nuclides are extracted as doubly-charged ion when operating at cryogenic temperatures. As indicated by Fig. 1.21, isotopes of francium, an alkali metal, were extracted as singly-charged ions when the temperature in the gas cell was near room temperature, and were extracted as doubly-charged ions when the temperature was low.

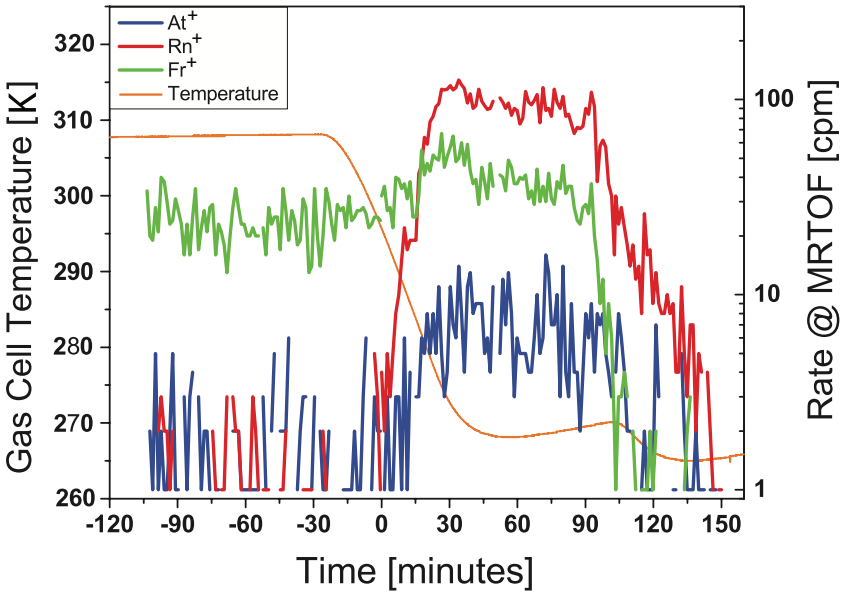

Figure 1.21: Observed yield at MRTOF-MS for singly-charged ions of isotopes of Fr, Rn, and At. The temperature was measured at opposite side of the cryocooler thermal coupling. At cryogenic temperatures, there were no singly-charged ions observed. This figure taken from [73].

From the measurements of At^{2+}, Rn^{2+}, Fr^{2+}, etc., an element with a second ionization potential of less than 22 eV, corresponding to the second ionization potential of Fr, is expected to be extracted in the doubly-charged state under cryogenic temperature operation. The suppression of U^{2+} below 105 K was also observed, which indicates that a third ionization potential below 22 eV is expected to be extracted in a triply-charged state at sufficiently low operating temperatures [73]. Recently it has been reported that Th^{3+} and U^{3+} were extracted from a gas cell [74], supporting this expectation.

Using the NIST Atomic Spectra Database [75], the expected extracted charge state for each element is summarized in Fig. 1.22. The elements indicated by open white letters are those that have been observed as doubly-charged ions at the SHE-Mass facility; most elements are predicted to be doubly-charged based on a second ionization potential above 22 eV.

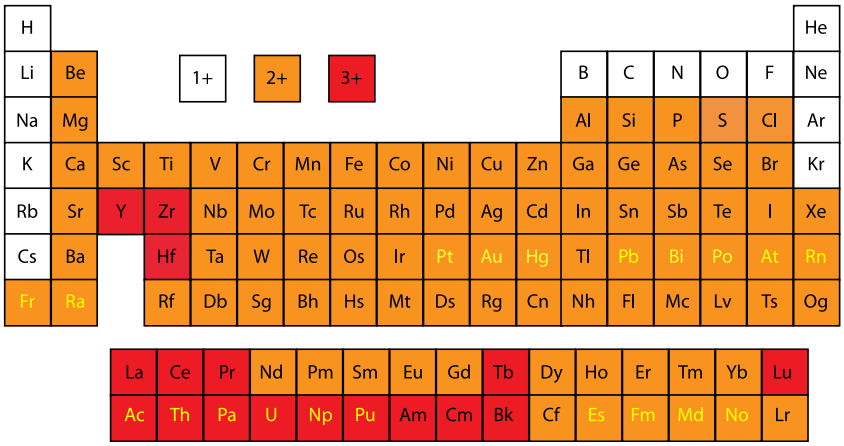

Figure 1.22: Expected extracted charge state for each element, presuming sufficient cryogenic temperature. The dominant charge states were determined as the maximum charge state with ionization potential less than 22 eV, based on the observation of Fr^{2+} . Elements labeled in white have been observed as doubly-charged ions at the SHE-Mass facility. This figure taken from [73].

1.6.3 Flat trap/Drift tube

The flat traps are built using two printed circuit boards (PCB) [76], as shown in Fig. 1.23, and work on the same principle as traditional segmented Paul traps. While conventional Paul traps use four rod electrodes to create an approximate quadrupole field, the flat trap uses six strip electrodes. Each PCB consists of three strips divided into seven segments. The central electrodes of each PCB have a 0.5 mm^2 hole at their center. During trapping, the same electric potential is applied to the central electrode of each PCB. By switching the potentials applied to the central electrode of each PCB, a dipole electric field is created at the center of the trap and ions can be extracted through the small exit hole. The ions emitted from the flat trap are guaranteed to have low emittance.

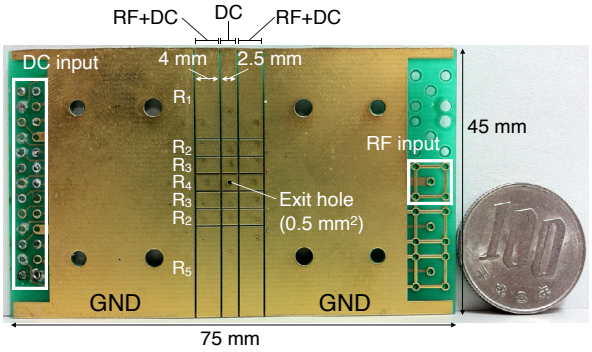

Electrode		R_1	R_2	R_3	R_4	R_5
Length (mm)		14.9	2.6	2.6	2.6	14.9
DC voltage (V)	: Accumulation*	-4.5	-5.7	-5.8	-6.0	5.0
	: Cooling	27	10.5	7.5	5.0	27

* R_1 side is the entrance in this case.

Figure 1.23: Photograph of the flat trap with typical direct current (DC) voltages annotated. A 100 JPY coin is included for scale. This figure taken from [76].

In the original SHE-Mass configuration, ions ejected from the first flat trap were accelerated by a pulsed drift tube. A second drift tube downstairs was used to decelerate the ions so they could be captured and stored in the second flat trap. The drift tube accelerates and decelerates ions by applying a high voltage pulse as they pass through the drift tube. A diagram of the principle of acceleration and deceleration by the drift tube is shown in Fig. 1.24.

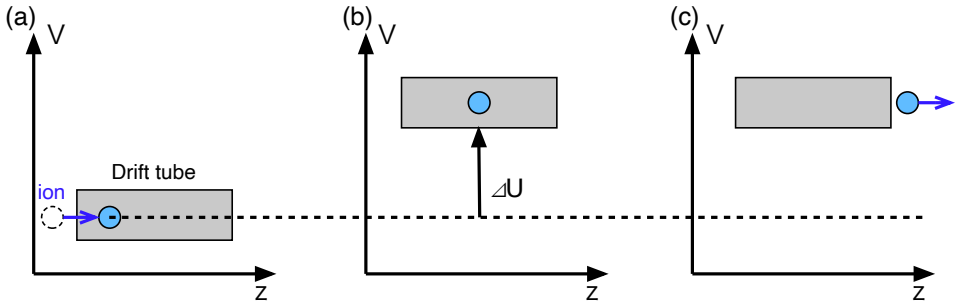

Figure 1.24: Diagram to explain the principle of a drift tube. (a) An ion enters the drift tube. (b) A high-voltage pulse is applied to the drift tube; the ion's potential energy increases by . (c) The ion accelerate by ΔU upon leaving.

1.6.4 Reference ion

All time-of-flight mass spectrometers, including MRTOF, require at least one mass reference to derive unknown masses from time-of-flight and to track time-of-flight drift in instruments for high accuracy mass measurements. The reference mass should ideally be an isobar of the species of interest to avoid higher-order effects in relation to TOF and mass. In addition, the intensity of the reference ion must be high enough to track TOF drift. Since such a suitable reference ion is not always available in online experiments, an external ion source is needed.

For offline calibrations and general online measurements, thermal ion sources [77] capable of providing alkali and alkali earth ions (Li^+, Na^+, K^+, Ca^+, Rb^+, Cs^+) are used. The flat trap can inject ions from the side opposite to the analyte ion delivery, as shown in the left side of Fig. 1.25. A voltage is applied to the heater electrodes of the ion source, and the emitted reference ions are transported by a linear ion trap to a flat trap for cooling. The reference ions are injected into the MRTOF during the time sequence during the cooling process of the analyte ions (right of Fig. 1.25), and the reference ion's TOF is measured.

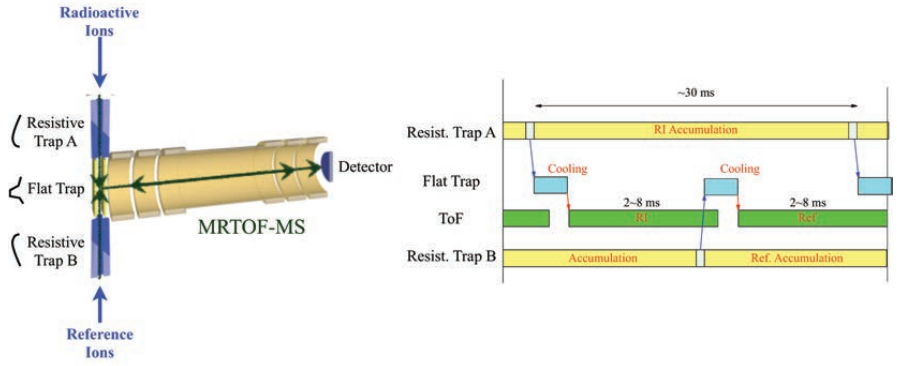

Figure 1.25: (left) Schematic view of ion injection from reference and analyte ion sides. (right) Conceptual view of time sequence of measurements. Using this method we can compensate for TOF drift without any loss of analyte ions.

Isobaric reference

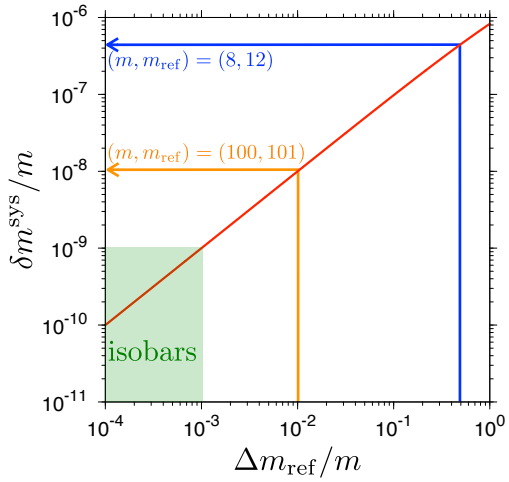

Figure 1.26: The effect of δt_0^{sys} on relative mass uncertainty as a function of relative mass difference between analyte and reference ions. This figure taken from [78].

The mass determination using reference ions is subject to systematic errors due to the mass difference between analyte and reference ions. The dependence of the measured mass on the offset time t_0 is linear, which can be expressed from the first-order expansion of Eq. 1.75 on t_0,

$$m = \frac{q}{q_{\rm ref}}\left(m_{\rm ref}\left(\frac{t}{t_{\rm ref}}\right) + 2m_{\rm ref}\frac{t(t-t_{\rm ref})}{(t_{\rm ref})^3}t_0\right). \tag{1.83}$$

The systematic error given by the uncertainty in t_0 is

$$\frac{\delta m^{\rm sys}}{m} = \frac{2m_{\rm ref}}{m}\frac{t(t-t_{\rm ref})}{t_{ref}^3}\delta t_0^{\rm sys} \tag{1.84}$$

$$= \frac{2}{t_{\rm ref}}\left(1-\sqrt{\frac{m+\Delta m_{\rm ref}}{m}}\right)\delta t_0^{\rm sys}, \tag{1.85}$$

where $\delta m^{\rm sys}/m$ is the relative systematic mass uncertainty, $m_{\rm ref}$ and $t_{\rm ref}$ are the mass and TOF of the reference ion, while m and t are the mass and TOF of the analyte ion. A single reference mass measurement of $^8Li^+$ ions using $^{12}C^+$ as a reference ion [51] yielded a systematic mass uncertainty of 3.4 keV (relative mass precision of $\delta m/m$=4.5×10^{-7}), assuming an uncertainty of δt_0 = 10 ns. To minimize such systematic errors, it is necessary to use isobaric references. When light particle emission channels such as α- and

p-channel exist from the fusion reactions, it is relatively easy to provide an isobaric reference. In the case of the reaction ^{nat}S(^{36}Ar,X), ^{65}Ga could be measured with a total relative precision $\delta m/m$=3.5×10^{-8} by use of an isobaric reference [79]. This precision was a comparable to that achieved by PTMS, and the atomic mass was in agreement with previous measurements by PTMS.

When using an external ion source, the systematic error is determined by the A/q difference between the analyte ion and nearest stable alkali isotope. For example, in the case that (m,$m_{\rm ref}$) is (100,101), then $\Delta m/m$=1%, producing a systematic error of 10^{-8}, as shown in the relationship between the mass difference and the system error shown in Fig. 1.26. The use of an isobaric or near-isobaric reference makes the statistical error dominant in most cases, so it has been considered to develop reference ions of heavy molecular ions by electrospray ionization (ESI) methods.

1.6.5 Drift correction

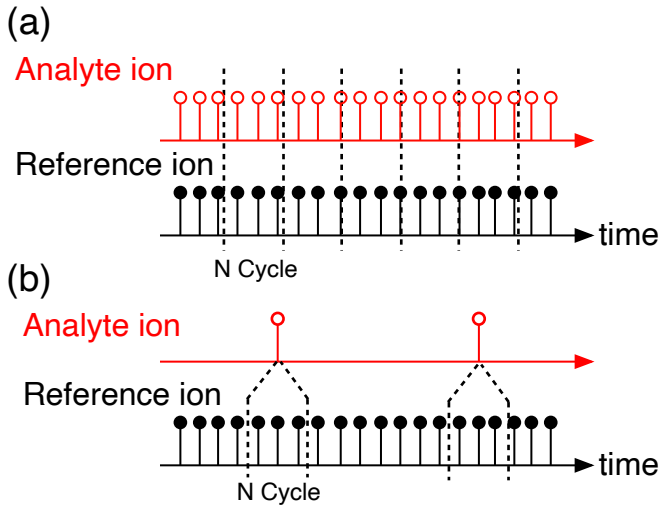

Figure 1.27: Comparison of drift correction methods. (a) Reference ions are sliced by each cycle. (b) Slice-by-event analysis methods.

In the case of long-term measurements, fluctuations in the time-of-flight may occur. Typical sources of such fluctuations include long-term fluctuations caused by the thermal expansion and contraction of the spectrometer and thermal drift of the power supplies due to temperature changes, and microscopic fluctuations caused by limited stability of the power supply voltages. These TOF drifts can be compensated for by the use of reference ions. If there are sufficient amounts of analyte ions, a simple correction is made

as shown in Fig. 1.27(a). Before making such corrections, first we calculate the "standard TOF" t_{std} determined by fitting the raw TOF data. The raw data is then divided into i subsets of N cycles each. For each subset i of ions, the corrected TOF $t_{\mathrm{corr,i}}$ is calculated using the following relationship,

$$t_{\mathrm{corr,i}} = t_{\mathrm{raw,i}}\left(\frac{t_{\mathrm{std}}}{t_{\mathrm{i}}}\right), \tag{1.86}$$

where $t_{\mathrm{raw,i}}$ is the uncorrected TOF for each ion in subset i, t_{i} is the center value of fitting within the i^{th} subset.

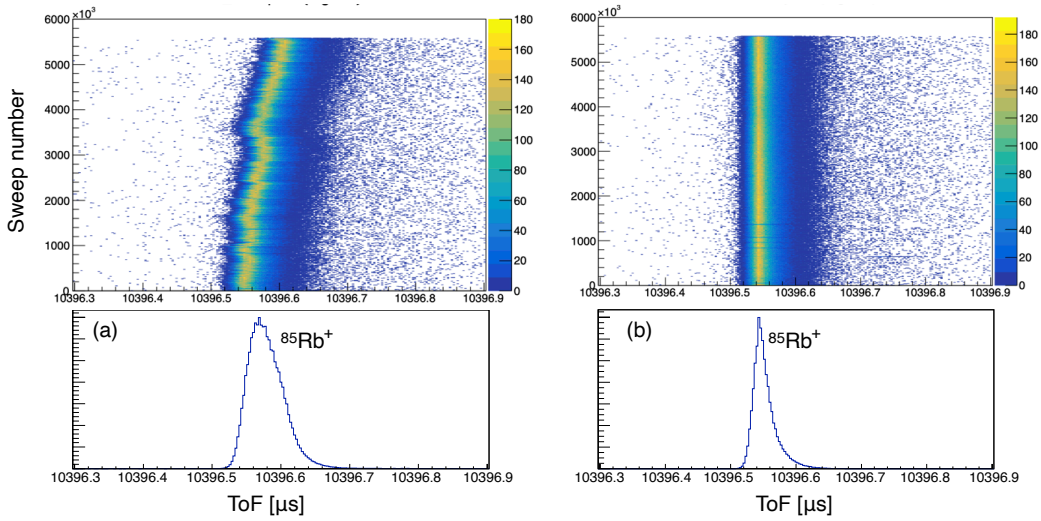

Figure 1.28: Example of drift compensation. (a) raw spectrum of $^{85}Rb^{+}$ during 24 hours measurements. (b) drift corrected spectrum by divided from every 600 cycles.

An example of the results of such a correction is shown in Fig. 1.28. This is a spectrum of the reference ion $^{85}Rb^{+}$ measured for 24 hours. The left panel shows a raw spectrum, and the right panel shows the spectrum corrected by using 600-cycle-subsets. It is striking how clearly the time-of-flight fluctuations in the spectrum have been compensated.

If the analyte ion are few, it is not necessary to look at all raw data for reference ions. In such a case, a method we call Slice-by-event analysis, shown in Fig. 1.27 (b), which uses reference ions before and after the each analyte event, is more suitable. This technique was used in the measurement of Md isotopes, which had a yield of about one event per 1,200 seconds [80]. By choosing an appropriate slicing cycle width, a comparison with the reference ion can be made with high accuracy, without the time fluctuation.

1.7 Direct mass measurement for heavy nuclei

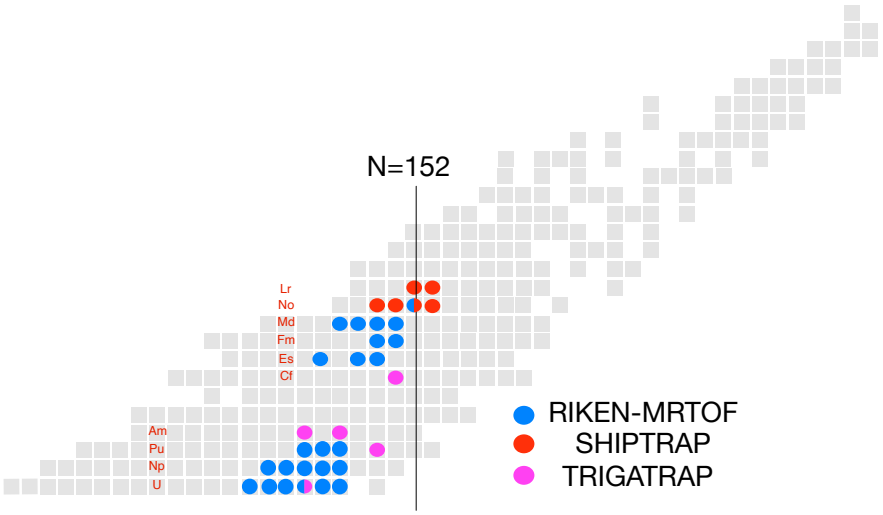

Figure 1.29: Part of the nuclear chart focusing on the transuranium region. The nuclei with a superimposed circle have been directly measured. Facilities which measured each isotope are color-coded as described in the legend.

There are not many cases of direct mass measurements of heavy nuclei. A region of the nuclear chart focusing on transuranium elements is shown in Fig. 1.29. Among the currently published data, only 10 nuclei have been directly measured among transfermium nuclei. The heaviest nuclei measured are $Z = 103$, ^{255}Lr and ^{256}Lr, measured by SHIPTRAP [81], the Penning trap system at GSI. The atomic masses of four nobelium isotopes were directly measured by SHIPTRAP [82, 83] and one isotope by RIKEN-MRTOF [80]. These nuclides can be produced in relatively high yields by cold fusion reactions of ^{48}Ca+^{208}Pb and ^{209}Bi. The cross section of ^{254}No is 1.8 μb and ^{256}Lr is 60 nb. The Es to Md isotopes have been measured only by RIKEN-MRTOF system [80]. Most of the nuclides in the vicinity of Uranium were measured by RIKEN-MRTOF in multi-nucleon transfer reactions of ^{18}O/^{19}F+$^{235/238}$U [84]. In addition, several transuranium nuclei produced in a nuclear reactor have been measured by TRIGATRAP [85].

1.7.1 SHE-Mass facility II

The location of GARIS-II was changed from the RILAC facility to the E6 room of RIBF facility as a part of the new superheavy element search project "nSHE". The MRTOF system was relocated at the same time and the SHE-Mass II facility was constructed, allowing direct coupling of the gas

cell with the focal plane of the GARIS-II. A comparison of the two setups is shown in Fig. 1.30. The basic ion manipulation techniques are equivalent, however the number of ion transport stages has been reduced because there is no longer a need for downstairs transport. Therefore, the total transport efficiency is expected to be improved. The previous SHE-Mass facility had an efficiency of about 1∼2%. The α-TOF detector to be developed in this study is installed in the ion detection section of the MRTOF.

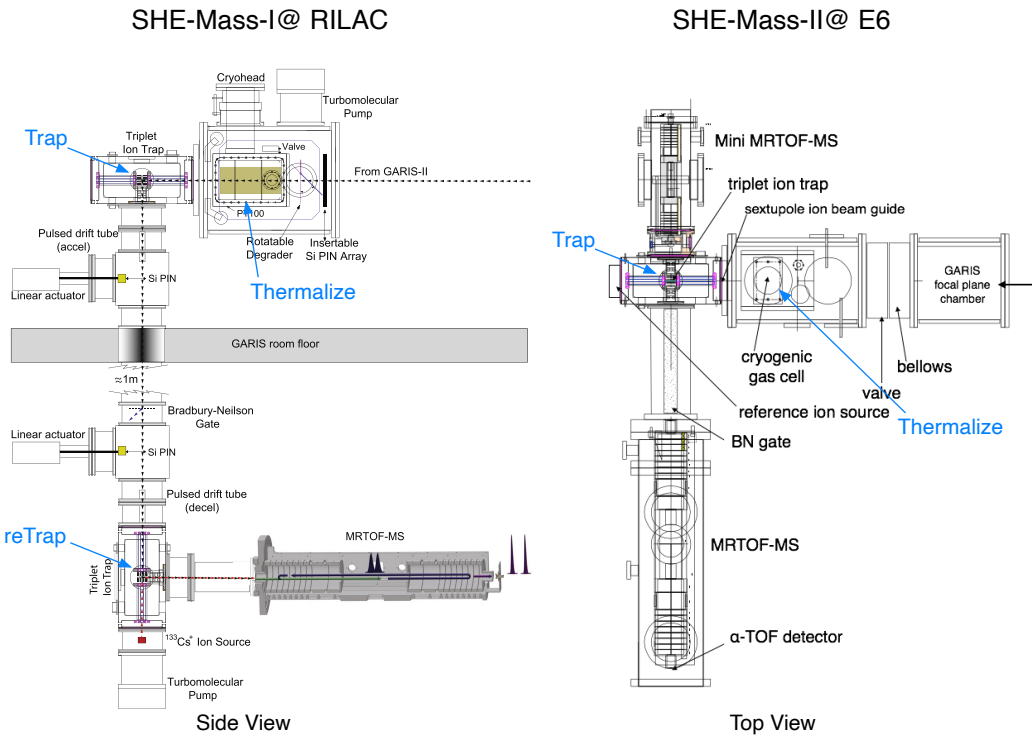

Figure 1.30: Schematic view of the comparison of the two facilities. (a) SHE-Mass facility at RILAC building. (b) SHE-Mass-II at E6 room in Nishina building – a part of RIBF.

1.7.2 Bottleneck for measurement of superheavy nuclei

The difficulty of experiments with superheavy nuclei is that the amount of atoms that can be produced is limited due to extremely low fusion cross-sections. Table 1.4 shows the half-lives, production reactions, cross-sections, and yields at the focal plane for various major nuclei with atomic numbers $Z \geq 101$. The yields are for a typical gas-filled recoil separation system, assuming a target thickness of 0.8 mg/cm^2 and a beam intensity of 0.5 pμA. Up to $Z = 103$, Lawrencium, has been measured by SHIPTRAP at GSI. And the masses of Nobelium have been successfully measured by the RIKEN-

MRTOF and SHIPTRAP, but no directly measurements of the masses of the so-called superheavy elements with $Z \geq 104$ have been published to date.

Table 1.4: Summary of half-life, production reactions, and cross-sections of typical transfermium nuclides. Yield estimates assume a target thickness of 0.8 mg/cm^2 and a beam intensity of 0.5 pμA.

Z	Nuclei	$T_{1/2}$	Reaction	Cross section [nb]	Yield
101	^{255}Md	27 min	^{248}Cm(^{11}B, 4n)	4000	20 s^{-1}
102	^{255}No	3.52 min	^{248}Cm(^{12}C, 5n)	580	3 s^{-1}
103	^{256}Lr	27 s	^{249}Cf(^{11}B, 4n)	122	0.7 s^{-1}
104	^{261}Rf	70 s	^{248}Cm(^{18}O, 5n)	13	4 min^{-1}
105	^{262}Db	34 s	^{248}Cm(^{19}F, 5n)	1.5	0.5 min $^{-1}$
106	^{265}Sg	8.5 s	^{248}Cm(^{22}Ne, 4n)	0.38	6 h $^{-1}$
107	^{267}Bh	17 s	^{249}Bk(^{22}Ne, 4n)	0.07	2 h^{-1}
108	^{269}Hs	9.7 s	^{248}Cm(^{26}Mg, 5n)	0.007	3 d^{-1}
112	^{283}Cn	3.8 s	^{242}Pu(^{48}Ca, 3n)^{287}Fl $\rightarrow$ ^{283}Cn	0.004	2 d^{-1}
113	^{284}Nh	0.97 s	^{243}Am(^{48}Ca, 3n)^{288}Mc $\rightarrow$^{284}Nh	0.003	1.5 d^{-1}
114	^{289}Fl	1.9 s	^{244}Pu(^{48}Ca, 3n)	0.002	1 d^{-1}

For nuclei with higher atomic numbers, production cross section of $\sigma \ll$ 10 nb are typical and we must anticipate event rates on the level of one per day or less. In such a measurement, reliable discrimination of background events – such as dark counts, stable molecules, etc. – is essential.

The primary decay mode of superheavy elements is alpha decay and spontaneous fission, thus the decay properties can be used to fingerprint the radioactive nuclides. If we can correlate such decay properties with the time-of-flight signal, we will be able to distinguish a true event from background events.

For this purpose, we have developed a new detector, referred to as an α-TOF detector, which can measure an ion's time-of-flight as well as its decay energy and absolute time between implantation on the detector and subsequent decay(s) of implanted radioactive ions. In addition to background reduction in mass measurements, this detector can be used for nuclear spectroscopy such as half-life determination and disambiguation of ground and excited states.

1.8 Research strategy

In this study, we have developed an α-TOF detector to solve the problem of mass measurement of superheavy nuclei, as described in Section 1.7.2, and to open up a new technique of decay-assisted mass spectroscopy. Details of the development and the performance evaluation of the α-TOF by offline radioactive source and online testing are described in Chapter 2.

In Chapter 3, as a demonstration of the nuclear spectroscopy use of the α-TOF detector, we present the results of TOF-decay correlation measurements for the short-lived nuclides $^{206/207}$Ra.

In Chapter 4, we report the results of the mass measurement of ^{257}Db, which was the first direct mass measurement of a superheavy element, and conclude with a discussion of future work.

Chapter 2

Development of the α-TOF detector

This chapter describes the details and procedures for developing the α-TOF detector.

2.1 Concept of the α-TOF detector

The α-TOF detector is based on a commercial MagneTOF[1] detector as shown in Fig. 2.1. It consists of an impact plate, internal circuitry to generate a suitable electric field, permanent magnets, and an electron multiplier.

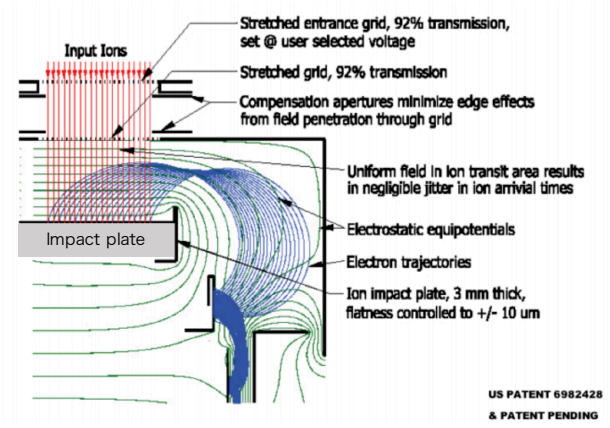

Figure 2.1: Schematic view of the MagneTOF detector. This figure taken from [86].

When an ion hits the impact plate of the MagneTOF detector, sec-

[1] https://www.etp-ms.com

ondary electrons are emitted and those electrons are isochronously guided, by crossed electric and magnetic fields, to the electron multiplier amplifying section of the detector to provide a fast timing signal for the ions.

We replaced the central portion of the impact plate with a silicon surface barrier detector (SSD, hamamatsu S-3590), as shown in Fig. 2.2. The surface of the SSD was coated with a particular material which has high secondary emission probability. After incoming ions are implanted on the surface of the SSD, then subsequent α-decays or spontaneous fissions can be detected by the SSD.

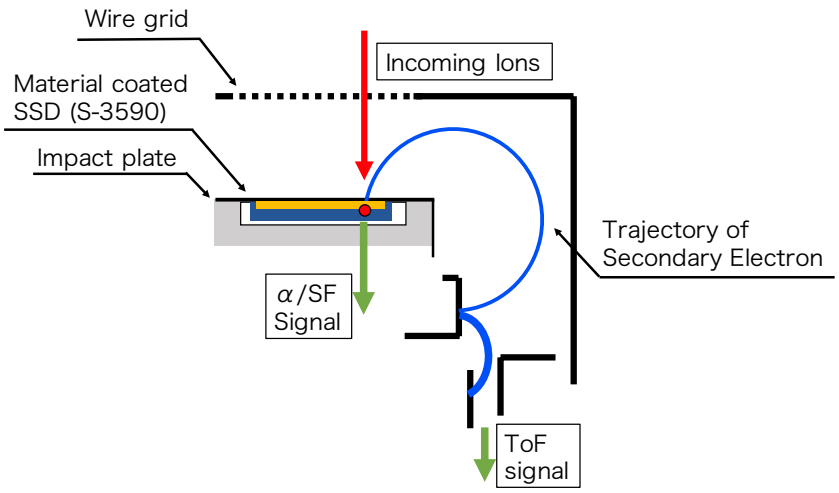

Figure 2.2: Schematic view of the α-TOF detector. Embedded within the MagneTOF impact plate is a specially coated silicon surface barrier detector.

2.2 Fabrication of modified impact plate

In order to provide the MagneTOF with an α-ray detection function, a modified impact plate was fabricated. To keep the potential of the impact plate uniform, the surface of the SSD was coated with gold. The gold coated surface area was then wire-bonded to a terminal on the front side of the SSD, which is electrically connected to the impact plate. In order to provide efficient secondary electron emission, a further coating was applied to the gold-coated SSD surface.

Secondary electrons are emitted from the surface of the target due to inelastic scattering of an incident particle which strips the outer-shell electron of atoms in the target material. The secondary electron emission rate is determined by the material composition and lattice orientation of the material,

and many studies have been done in the past to determine the secondary electron emission rate. Both MgO and Al_2O_3 are materials known to have high secondary electron emission probabilities [87, 88, 89] and no deliquescence [90]. We compared the performance of MgO with that of Al_2O_3.

The materials coating was done in three steps as shown in Fig. 2.3. The detector surface was first coated with gold and then the anode electrode was wire bonded to the gold surface. After the wire bonding, the secondary electron emitter – either MgO or Al_2O_3 – coating was applied.

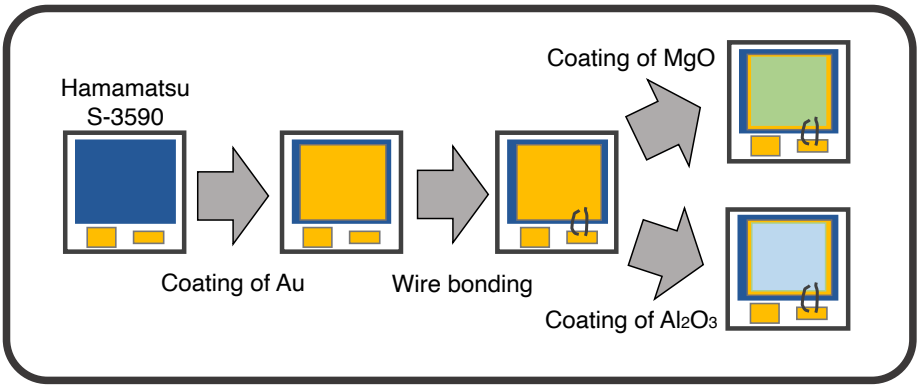

Figure 2.3: Process of material coating. The detector surface was coated with gold and the anode electrode was wire bonded to the gold surface. The secondary electron emitter MgO/Al_2O_3 was then coated.

2.2.1 Coating of material on SSD

Coating of Au

Gold coating was accomplished by a vacuum evaporation method. In the vacuum evaporation method a thin film is formed by heating an evaporation source (gold in this case) in a vacuum chamber and allowing it to deposit on an object. As the melting point of gold is 1064°C, it is easy to form a thin film by this vacuum evaporation method.

If gold were to coat the exclusion zone of the SSD shown in Fig. 2.4, the p-side and n-side would short-circuit, and the detector would not work. Therefore, we designed a mask for use in the vacuum evaporation to prevent gold from entering the area during the coating process.

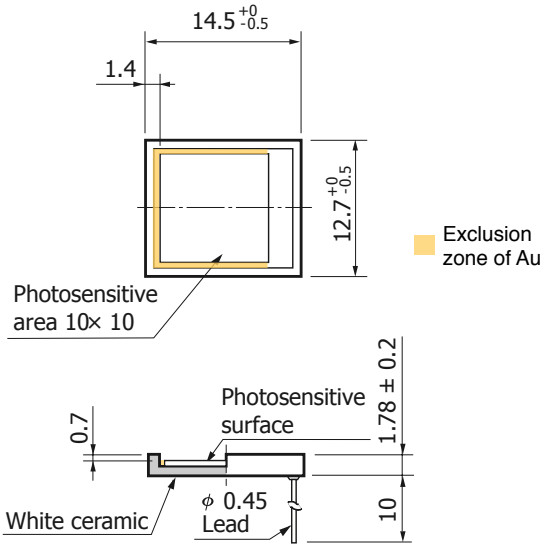

Figure 2.4: The schematic view of SSD (S-3590).

A Schematic view of the mask is shown in Fig. 2.5. The photosensitive area of the SSD is 10 mm×10 mm. The mask was designed to be 9 mm × 9 mm. The photographs of masks are shown in Figs. 2.6 and 2.7.

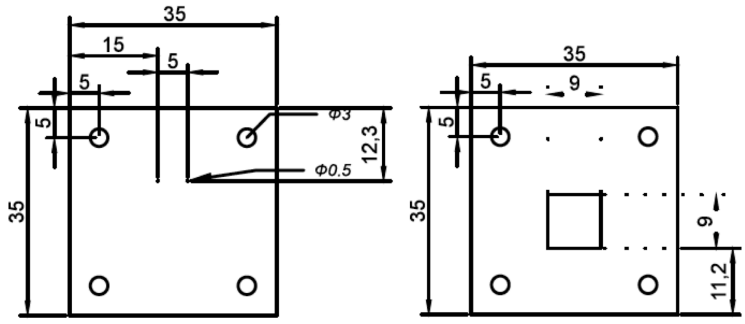

Figure 2.5: A drawing of the mask for SSD.

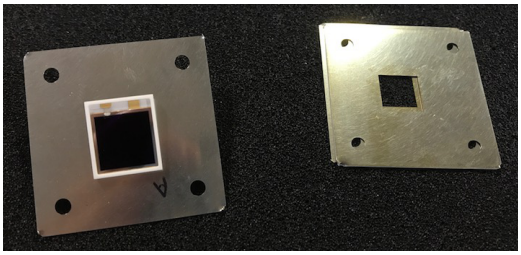

Figure 2.6: A photograph of the mask.

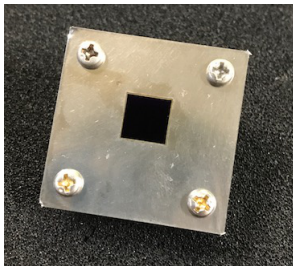

Figure 2.7: The SSD equipped with mask prior to vacuum deposition of gold.

The instrumentation of the vacuum evaporation system was as shown in Fig. 2.8 with the top plate suspended from the ceiling and the SSD covered with a mask. The top plate is set at same height as a thickness gauge. We confirmed evaporation Au on the surface of the SSD to a thickness of about 100Å with the use of the thickness gauge reading. Figure 2.9 shows the SSD after the gold coating and wire-bonding.

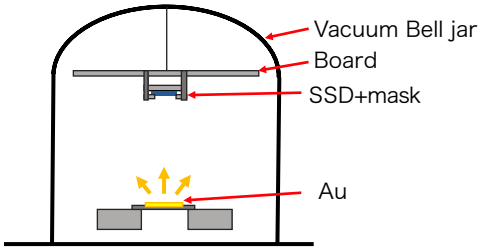

Figure 2.8: Schematic of the vacuum evaporation system setup.

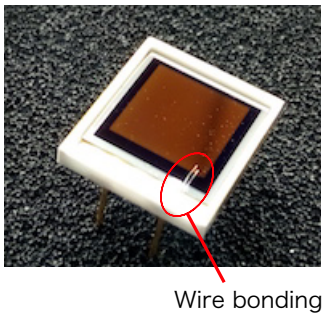

Figure 2.9: The Au coated SSD after wire bonding.

Coating of Al_2O_3

As aluminum has a melting point of 660°C, it also easily forms a thin film by vacuum evaporation. The Al was coated using vacuum evaporator in the same manner as the Au coating. The Al was also coated to 100Å , similar to the gold. Since Aluminum is an easily oxidized metal, a thin coating of Al will quickly change to Al_2O_3 when exposed the air.

Coating of MgO

Unlike gold and aluminum, MgO has a melting point of 2852°C, making it difficult to form a coating using a vacuum evaporation method. Thus, the coating was done by using a sputtering method; specifically, magnetron sputtering. Permanent magnets are placed underneath the sputtering sample. After initial evacuation of the chamber, a small amount of argon is introduced ($P_{\mathrm{Ar}}<$ 1kPa). Application of an RF electric field creates a plasma from the argon gas. The magnetic field binds the charged plasma, forcing it to impact the source material. These impacts ionize the source material, which is then deposited (an neutralized) on the object to be coated. A schematic overview of the magnetron sputtering equipment is shown in Fig. 2.10.

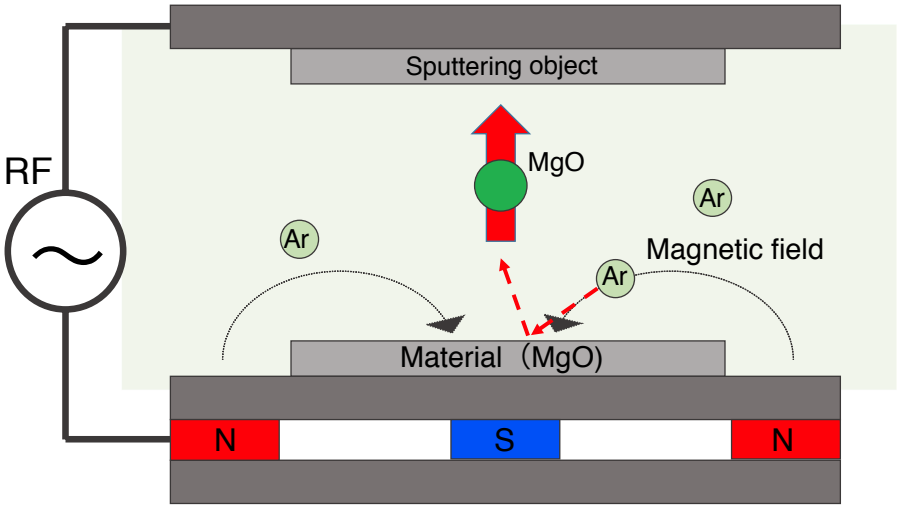

Figure 2.10: Schematic overview of the radio-frequency magnetron sputtering equipment.

Calibration of the thickness gauge

In order to calibrate our thickness gauge, an aluminum foil with the same area as the mask was prepared prior to MgO coating by sputtering. The calibration of the thickness gauge was performed by comparison with the thickness of this foil as determined by weighing it before and after the coating, and using the density of MgO (3.58 g/cm^3) to convert from weight to thickness. The correlation between the calculated thickness of MgO and thickness gauge readings is shown in Fig. 2.11.

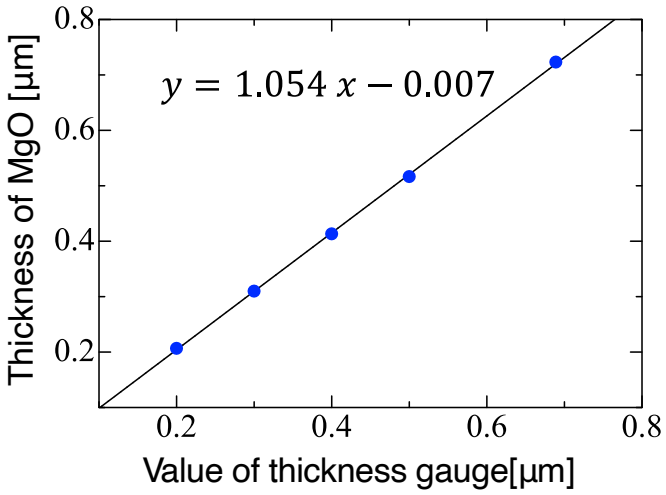

Figure 2.11: Thickness gauge calibration curve.

The data points in Fig. 2.11 were fitted with a linear function, and the thickness was determined using the resulting calibration equation. The RF power of the sputtering equipment was set to 300 W and the flow rate of Ar gas was set to 2 sccm. The SSD was coated with MgO to a thickness of 100Å based on the thickness gauge reading.

2.2.2 Embedded to impact plate

The secondary electron emitter coated SSDs were installed in impact plates such as the one shown in Fig. 2.12.

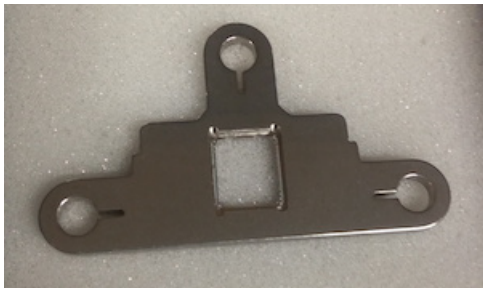

Figure 2.12: The impact plate with a hole for embedding of SSD.

A rectangular hole was machined at the center of the impact plate as shown in Fig. 2.12, and Au+MgO/Al_2O_3 coated SSDs were embedded in it. The SSDs were fixed with a two-liquid mixture sealant. The impact plates were installed into MagneTOF detectors by the *ETP Ion Detect.*

Corporation. An impact plate and α-TOF detector are shown in Fig. 2.13. Both terminals of the SSD on the α-TOF are accessible by SMA connectors. A cross-sectional view of the α-TOF is shown in Fig. 2.14.

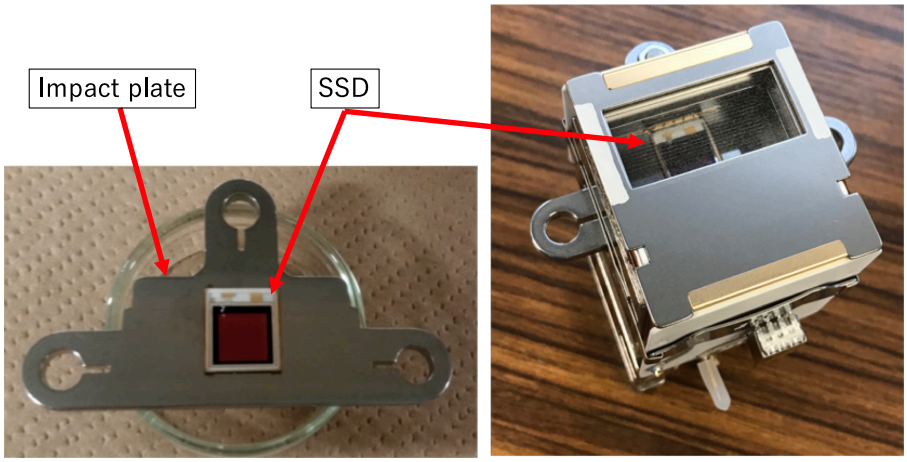

Figure 2.13: Photographs showing the impact plate with SSD installed (left) and a fully assembled α-TOF detector.

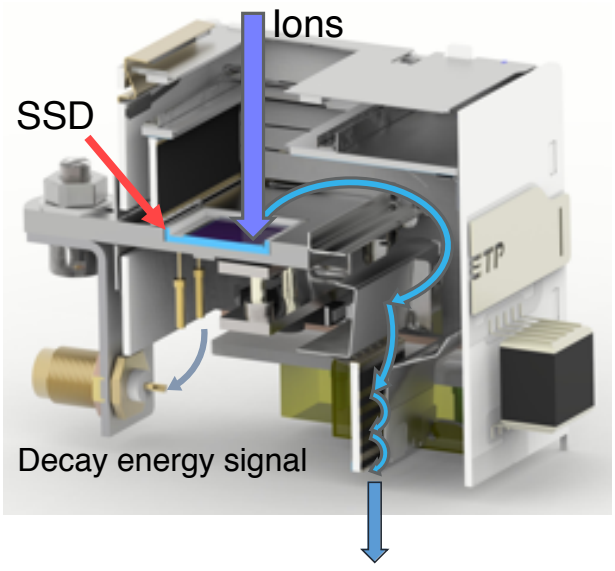

Figure 2.14: Cross-section of the α-TOF detector. This figure taken from [91].

2.3 Design of front-end circuit board

In normal operation, the α-TOF detector's impact plate must be placed at a negative high potential, approximately -2 kV. Since the SSD is also placed on the impact plate potential, an optically isolated circuit was developed to both provide a bias voltage for the SSD and amplify the decay signals.

A sketch of the design for such an optical isolation system is shown in Fig. 2.15. The signal from the Si detector is amplified by two charge sensitive pre-amplifiers having different gains: a high-gain one for α-ray signals and a low-gain one for spontaneous fission signals. The amplified analog signals are sent to shaping amplifiers on ground potential through an optical transceiver. The data from the Si detector and the time-of-flight data are separately recorded event by event with absolute time stamps.

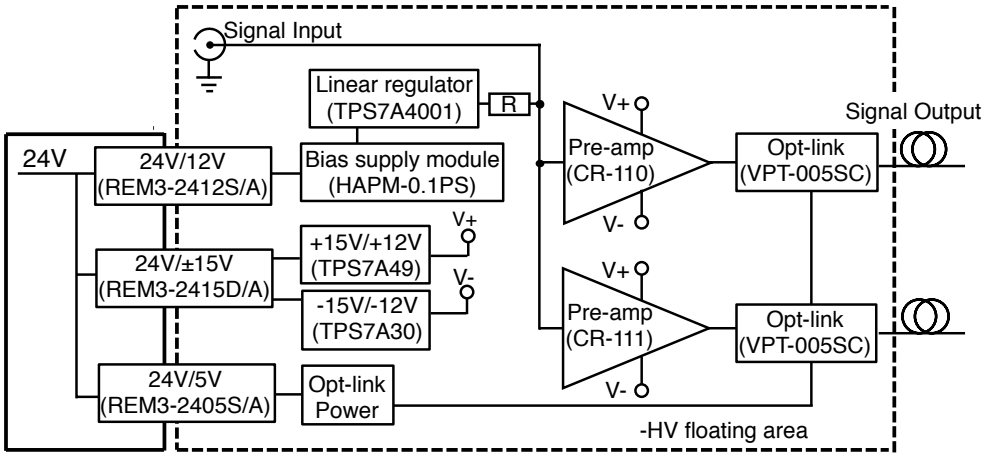

Figure 2.15: Sketch of the floating signal processing front-end circuitry. The area surrounded by the broken line is on the high voltage ground plane. This circuit consists of a high-gain preamplifier (Cremat CR-110, 1.6 V/pC) and a low-gain preamplifier (Cremat CR-111, 0.16 V/pC), ultra low noise voltage regulators (Texas Instruments, TPS7A49/30) for the preamplifiers, a -70 V power supply for the SSD bias (Matsusada, HAPM-0.1PS) with high voltage linear regulator (Texas Instruments, TPS7A4001), and optically isolated "Opt-link" signal transceivers (Nanaboshi, VPT(R)-005SC). The electric power for the isolated circuits are supplied by DC/DC converters rated for 5 kV isolation (RECOM, REM3 series).

The circuit of Fig. 2.15 was used in the offline and online characterization and performance evaluation test of the α-TOF detector described in this chapter. In the characterization test described below, the energy resolution

was evaluated to be σ_E=141.1(9) keV, which is about twice that of a typical Si detector. In addition, we found that random noise was appeared to the time-of-flight spectrum when we operated the detector. This random noise can be suppressed by increasing the threshold level of the detection system, but at the cost of reduced ion signal detection efficiency; as low as possible threshold level is desirable.

We set the MRTOF-MS to single-pass measurement mode (no reflection) to evaluate the threshold voltage at which the random noise disappears. It was found to require a threshold of 52.3 mV, as compared to the 20 mV threshold typically used with the conventional MagneTOF detector. By changing the 24 V primary power supply of the front-end circuit from a switching power supply to a stabilized power supply (KIKUSUI), the threshold level required to suppress the noise was reduced to 35 mV. Therefore, as the noise was presumed to be caused by the switching noise from power supply, we made some improvements. A sketch of the improved circuit diagram is shown in Fig. 2.16.

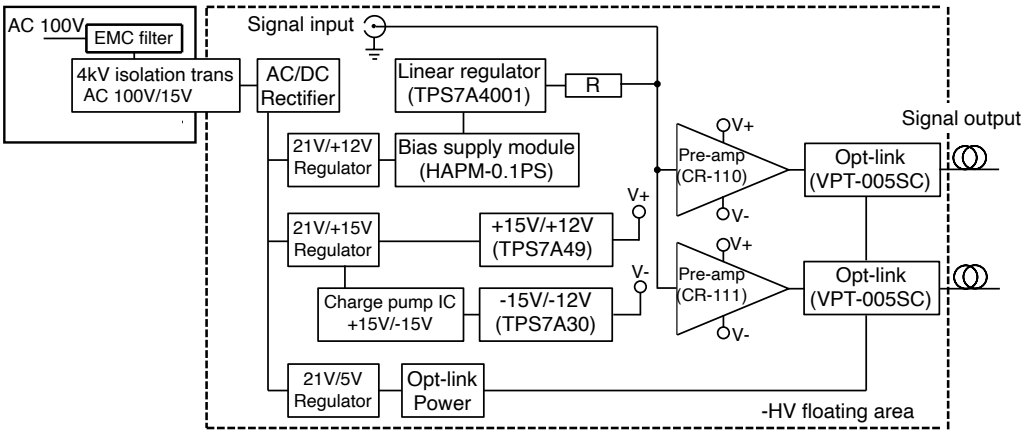

Figure 2.16: Sketch of the improved front-end circuitry. The area surrounded by the broken line is on the high voltage ground plane. An isolation power supply transformer is installed instead of the isolation DC/DC module in Fig. 2.15, and the AC voltage stepped down from the commercial 100V AC is rectified on the high-voltage ground plane for use in the circuit.

In the initial circuit (Fig. 2.15), a 5 kV isolated DC/DC converter was placed on the board. This DC/DC produced switching noise that is thought to be the noise source of the circuit. In the improved circuit, a toroidal isolation power transformer is installed instead of an isolation DC/DC converter. After passing the 100 V AC (Alternating Current) mains supply through the EMC (Electro Magnetic Compatibility) filter, the voltage is step down from 100 V_{rms} AC to 15 V_{rms} AC by using a high-voltage isolation transformer.

After being rectified to produce 21 V DC, the regulator and charge pump IC installed on the board produce the DC ±12V and DC +5V required for the circuit board. In this way, we could reduce the noise of the power supply circuit.

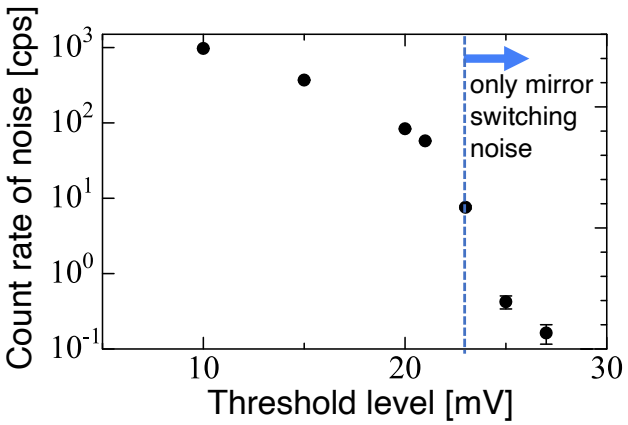

Figure 2.17: The noise count of the circuit is shown as a function of the threshold level of the measurement system. The noise is the sum of the switching noise caused by the opening and closing of the mirror and the random noise caused by the circuit, which appears in the time-of-flight signal when the single-pass measurement mode is selected. When the threshold level is 23 mV, the random noise disappears and only the switching noise when the mirror is open/close appears.

Figure 2.17 shows the measurement results of the threshold level using the improved circuit. The sum of the switching noise caused by the opening and closing of the mirror and the random noise caused by the circuit, which appears in the time-of-flight signal when the single-pass measurement mode is selected, is normalized by the measurement time and shown as a function of the threshold level. At a threshold voltage of 23 mV, the random noise disappeared and only switching noise due to the opening and closing of the mirror was observed. This threshold level is equivalent to that of the conventional MagneTOF detector.

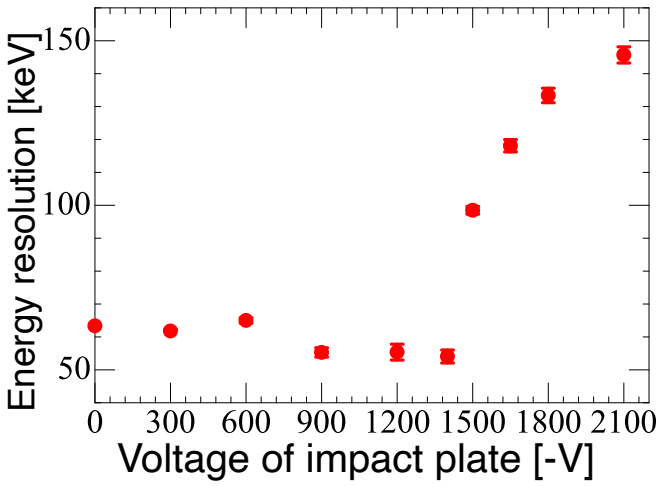

Figure 2.18: The energy resolution of α-TOF detector as a function of the voltage applied to the impact plate. The energy resolution drastically deteriorates when the applied voltage exceeds 1500 V. This voltage corresponds to the switch-on voltage of the Zener diode built into the MagneTOF.

On the other hand, there was no improvement in the energy resolution of α-TOF detector. This suggests that the cause of the worsening resolution of the α-TOF is not the front-end circuitry, but the internal circuitry of the α-TOF itself. Figure 2.18 shows the relationship between the energy resolution of α-TOF and the voltage applied to the impact plate. It can be seen that the energy resolution of α-TOF drastically deteriorates when the applied voltage exceeds 1500V. This voltage corresponds to the switch-on voltage of the Zener diode built inside the MagneTOF. This Zener diode is predicted to be the cause of the worsening in energy resolution, but it cannot be removed because of its role in building a stable potential structure. In general, Zener noise should only occur up to the switch-on voltage (-1500 V in this case), after which it should disappear if enough current flows. However, the noise that seemed to be Zener noise did not dissipate even after supplying up to 2200V, and the energy resolution was not improved. However, it is sufficient to our needs in most cases, such as the discrimination of the alpha decay energy in superheavy element region. This improved circuit system was used in the ^{206,207}Ra and ^{257}Db experiments described in Chapters 3 and 4.

2.4 Characterization test of α-TOF with α-source

The new detector was thoroughly characterized offline. In particular, the detection efficiency and timing resolution were characterized and found to be sufficient to perform atomic mass measurements. In addition, the

new detector's fitness for particle identification was confirmed by α-energy correlated time-of-flight (E_α-TOF) measurements. The setup of the characterization test is shown in Fig. 2.19.

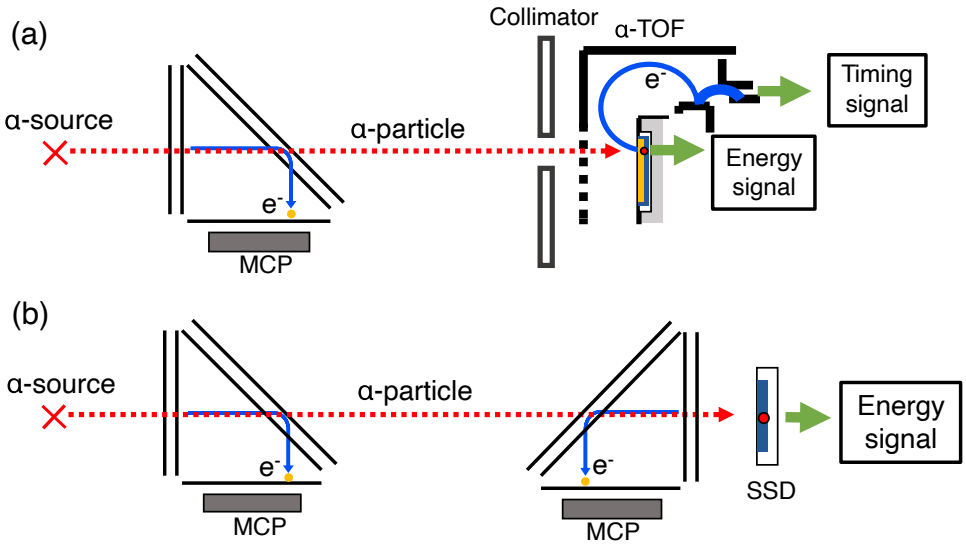

Figure 2.19: (a) Configuration of the setup used in the offline tests. For detection efficiency and time resolution measurements, a ^{241}Am source was used, while for correlation measurement, a mixed α-source was used. (b) Configuration of the setup used to determine the intrinsic time resolution of the triangle-roof detector (see text).

2.4.1 TOF detection efficiency

We characterized the detection efficiency of the α-TOF detector by using collimated 5.48 MeV α-rays from a ^{241}Am source. As the SSD should have near unity detection efficiency for 5.48 MeV α-rays, the efficiency was defined as the ratio of coincident TOF signals to the α-singles counts. A TOF signal was considered to be coincident with an α-ray when the timing signal and α signal were detected within 500 ns of each other. The α-singles signals were limited to those signals with an SSD signal amplitude commensurate with ^{241}Am α-rays. Table 2.1 and 2.2 shows the coincident signal and detection efficiency measured for both MgO and Al_2O_3 surface coatings as functions of the high-voltage potential applied to the impact plate. The detection efficiencies with MgO and Al_2O_3 surface coatings are plotted as functions of applied voltage in Fig. 2.20. At the nominal operation potential of -2100 V, the efficiency was more than 90% for both surface coatings. For subsequent measurements, only the MgO-coated detector was used.

As the SSD should have near unity detection efficiency for such energetic

alpha particles, they provide an excellent means for measuring the absolute detection efficiency of the TOF signals, the relative performance of the two coatings, and our ability to correlate TOF and energy signals. The TOF signal detection efficiency was determined using energetic (5.48 MeV) alpha particles. While the average number of secondary electrons emitted from the surface by such alpha particles may be slightly higher than in the case of $\sim$2 keV/q heavy ions, the probability to emit at least one electron is not dissimilar [92]. Thus, while the heavy ions may require operating the detector at a higher gain, the detection efficiency should be similar.

Table 2.1: Table of coincidence counts for MgO type α-TOF detector.

Voltage [V]	Coincident signal [cps]	α-signal [cps]	Coincidence efficiency
-2200	6.694±0.114	6.929 ± 0.083	0.966 ±0.020
-2150	6.445±0.099	6.976 ± 0.072	0.924 ±0.017
-2100	6.243±0.106	6.966 ± 0.083	0.896 ±0.018
-2050	5.602±0.082	6.748 ± 0.081	0.830 ±0.016
-2000	4.749±0.080	7.041 ± 0.091	0.674 ±0.014
-1950	2.775±0.043	6.936 ± 0.095	0.400 ±0.008
-1900	0.388±0.015	6.840 ± 0.080	0.056 ±0.002
-1850	0.005±0.003	7.004 ± 0.118	0.001 ±0.001

Table 2.2: Table of coincidence counts for Al_2O_3 type α-TOF detector.

Voltage [V]	Coincident signal [cps]	α-signal [cps]	Coincidence efficiency
-2200	6.431±0.102	6.796 ± 0.093	0.946 ±0.020
-2150	6.394±0.108	6.861 ± 0.116	0.932 ±0.022
-2100	6.303±0.061	6.878 ± 0.099	0.916 ±0.016
-2050	5.849±0.100	6.965 ± 0.084	0.840 ±0.017
-2000	4.908±0.081	6.791 ± 0.112	0.723 ±0.017
-1950	3.114±0.053	6.877 ± 0.105	0.453 ±0.010
-1900	0.713±0.035	6.934 ± 0.074	0.103 ±0.005
-1850	0.031±0.007	7.004 ± 0.118	0.004 ±0.001

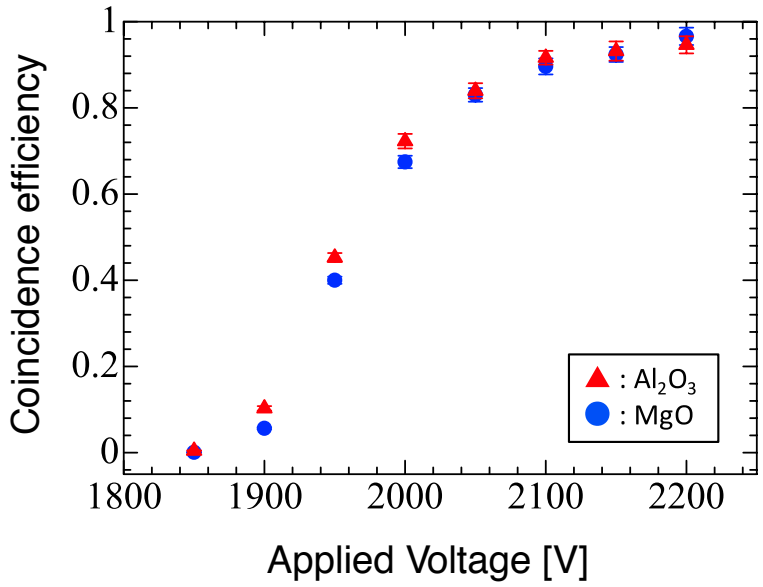

Figure 2.20: Implantation signal detection efficiencies measured for 5.48 MeV α-rays as functions of impact plate potential. Red triangles and blue circles designate results for Al_2O_3 and MgO coatings, respectively.

2.4.2 Time resolution

The reference timing signals for the time-of-flight measurements were provided by a Busch type triangle-roof time-of-flight detector [93, 94] located 27 cm upstream from the α-TOF detector, as shown in Fig. 2.19 (a). The time resolution was determined from the time-of-flight spectrum. In general, the time resolution σ_{A-B} of a system consists of detectors A and B with a time resolution $\sigma_{A,B}$ which can be expressed by the convolution of these two as in Eq. (2.1),

$$\sigma_{A-B} = \sqrt{\sigma_A^2 + \sigma_B^2}. \tag{2.1}$$

In the following discussion, the time resolution of the triangle-roof detector and the α-TOF detector are indicated as σ_{tri} and $\sigma_{\alpha\mathrm{TOF}}$, respectively, while $\sigma_{\mathrm{tri}-\alpha\mathrm{TOF}}$ is the measured time resolution, a convolution of these two contributions.

The directly measured time resolution was $\sigma_{\mathrm{tri}-\alpha\mathrm{TOF}} = 413.7(33)$ ps using the start signal given by the triangle-roof detector and the stop signal from the α-TOF detector. However, to disentangle the effect of the triangle-roof detector's start timing from the stop timing of the α-TOF, a comparison setup has been used as shown in Fig. 2.19 (b). Two triangle-roof detectors of

the same type have been placed opposite to each other, where one has been used as the start and the other as the stop signal. An SSD was placed behind the triangle-roof detector to produce a trigger signal as in the detection efficiency measurement. The standard deviation of the time differences was found to be $\sigma_{\mathrm{tri-tri}} = 465.5(40)$ ps.

From this the resolution of a single triangle-roof detector was deduced to be $\sigma_{\mathrm{tri}} = \frac{1}{\sqrt{2}}\sigma_{\mathrm{tri-tri}} = 329.2(28)$ ps. Using this value, we then determined the intrinsic time resolution of the α-TOF detector to be $\sigma_{\alpha\mathrm{TOF}} = \sqrt{\sigma^2_{\mathrm{tri}-\alpha\mathrm{TOF}} - \sigma^2_{\mathrm{tri}}} = 250.6(68)$ ps.

2.4.3 TOF-E correlation measurement by using mixed triplet α-source

In order to make an offline confirmation of the ability to utilize the α-TOF detector to perform a correlated E_α-TOF measurement under rudimentary conditions, a mixed α-source comprising ^{244}Cm (5804 keV), ^{241}Am (5485 keV) and ^{237}Np (4788 keV) was utilized.

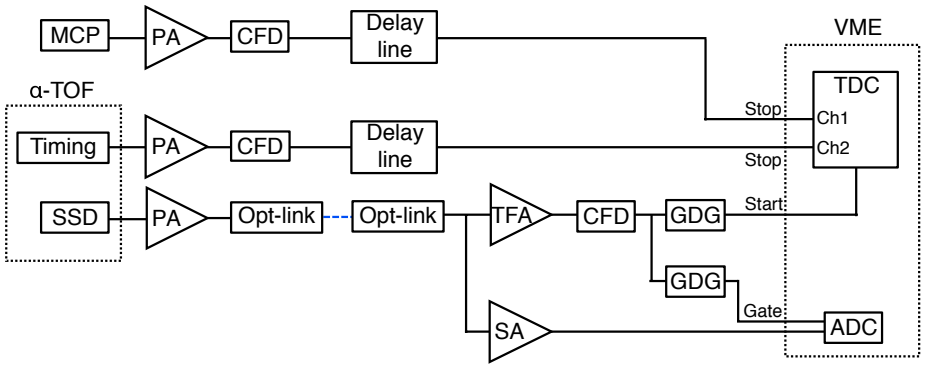

Figure 2.21: Sketch of data acquisition system for the correlated E_α-TOF measurement. PA: Pre Amplifier, CFD: Constant Fraction Discriminator, SA: Shaping Amplifier, TFA: Timing Filter Amplifier, GDG: Gate and Delay Generator, ADC: Analog to Digital Converter, TDC: Time to Digital Converter.

Due to its unity detection efficiency, the signal from the SSD was again used to trigger the data acquisition system (Fig. 2.21), as the common start signal of the time-to-digital converter (TDC), and to provide α-ray energies. Because the SSD response is slow, the timing signal of the triangle-roof detector and of the α-TOF detector each connected to stop inputs of the TDC through analog delay lines. The true TOF was determined from the time difference between the two stop signals.

A VME based data acquisition system, with an analog to digital converter module (MADC-32) for energy signals and a TDC module (MTDC-32) for timing signals, was used. The TDC have time resolution of 80 ps. Figure 2.22 shows the E_α-TOF correlated data measured using the mixed α-source. The incident α-ray rate could be set to be as low as $\approx$0.1 s by using a collimator. The projection of the two-dimensional spectrum (Fig. 2.22 (c)) onto the horizontal axis yields the singles time-of-flight spectrum. In the singles TOF spectrum, the three different α-ray signals are not resolved. However, by using the correlated energy spectrum, a 2D spectrum can be constructed. In the 2D spectrum, it is possible to resolve the three species and disentangle the TOF spectrum of ^{244}Cm from that of ^{241}Am.

The energy resolution for the 5.48 MeV α-rays was determined from the energy spectrum (Fig. 2.22 (b)) to be 141.1(9) keV.

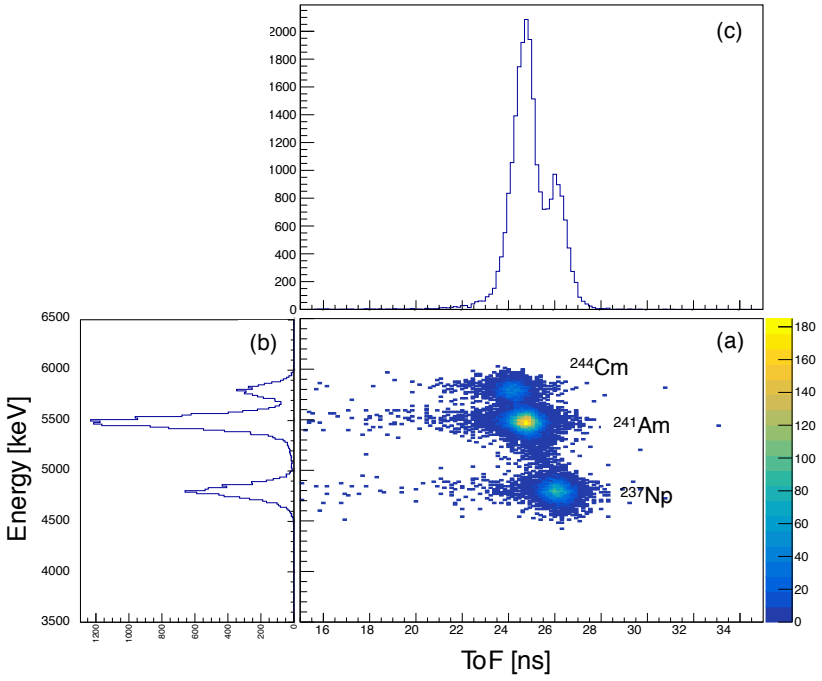

Figure 2.22: (a) Two dimensional spectrum showing a correlated E_α-TOF measurement obtained from mixed α-source. (b) Projection onto the E_α axis. (c) Projection onto the time-of-flight axis. The TOF was measured from triangle-roof detector to α-TOF detector.

2.5 Offline test

A more realistic performance test using an MRTOF-MS equipped with an α-TOF detector was performed offline with a ^{224}Ra source.

2.5.1 Decay correlated TOF measurement with radioactive ^{224}Ra progenitor

The decay scheme of the ^{224}Ra progenitor is shown in Fig. 2.23. The source was produced from a $^{232}Th(NO_3)_4$ $4H_2O$ solution by a chemical separation process [95]; a photograph of the ^{224}Ra source is shown in Fig. 2.24. It was installed inside the cryogenic gas cell (see Fig.2.25).

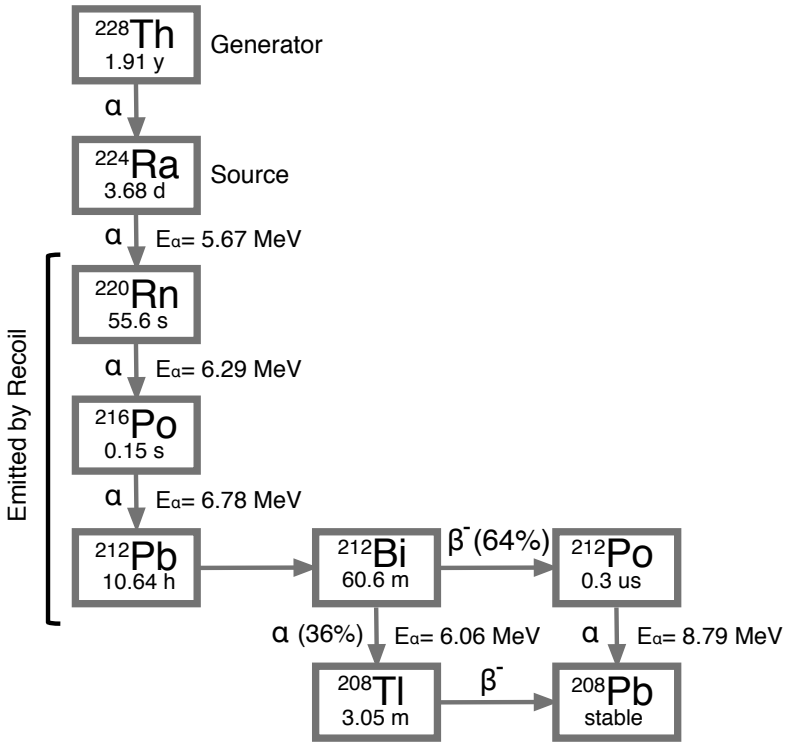

Figure 2.23: Decay scheme of the ^{224}Ra radio-active source.

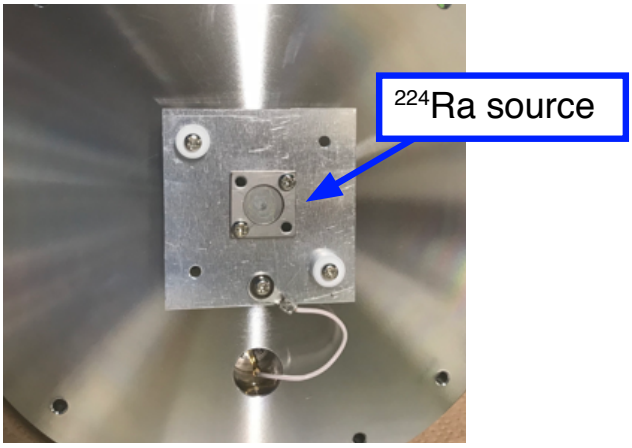

Figure 2.24: Photograph of the ^{224}Ra radioactive source.

Ions of the radioactive nulcide ^{220}Rn, produced in the α-decay of ^{224}Ra, and its decay daughter ^{216}Po, were thermalized in and extracted from the gas cell, transported to the MRTOF-MS preparation traps, and then injected into the MRTOF-MS for correlated TOF and α-decay measurements. The two nuclides have half-lives of 55.6 s and 145 ms with characteristic α-rays of 6.29 MeV and 6.78 MeV, respectively. For this preliminary measurement the MRTOF-MS was operated such that the ions made only 2 laps inside the MRTOF-MS reflection chamber. This was sufficient to unambiguously determine the A/q value with a mass resolving power of $R_m \approx 1500$ while still providing a wide mass bandwidth.

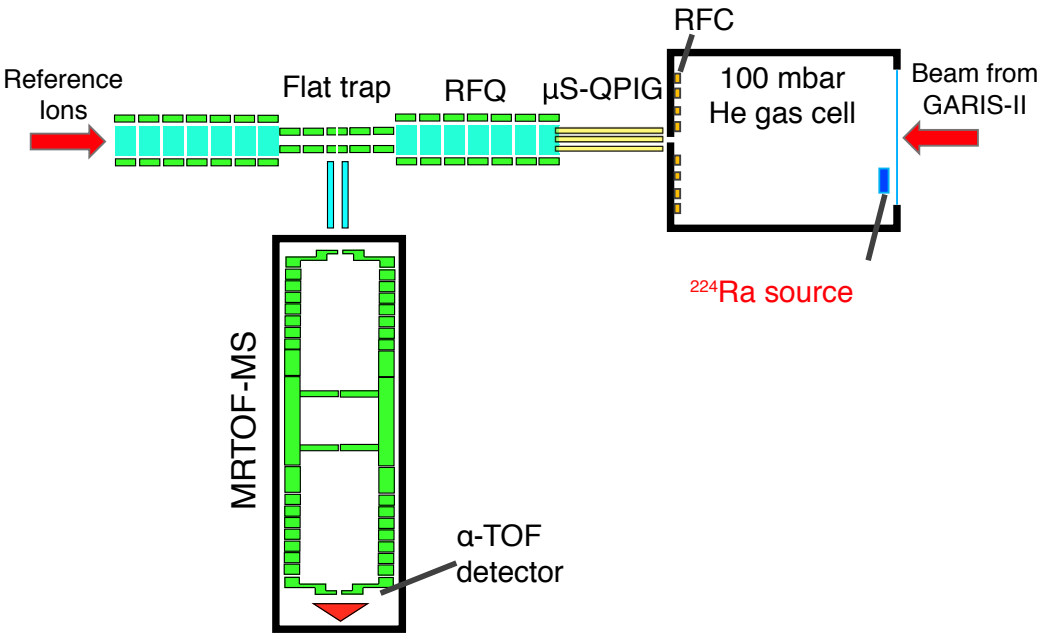

Figure 2.25: Setup for an offline measurement. The ^{224}Ra source is installed into the gas cell chamber.

2.5.2 Results

The α-singles spectrum is shown in Figure. 2.26. Peaks corresponding to the short-lived nuclides ^{220}Rn and ^{216}Po, and the long-lived ^{212}Bi were observed.

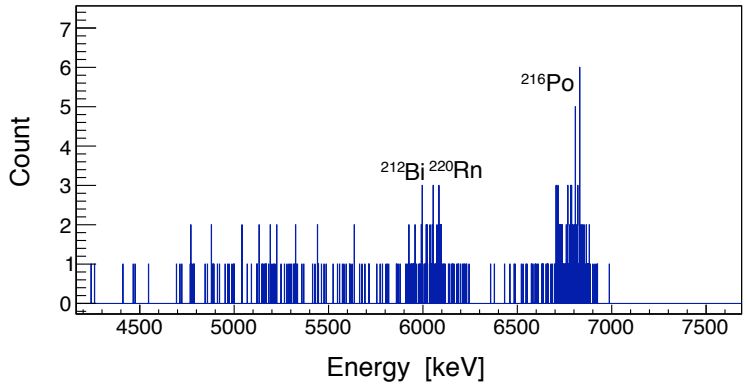

Figure 2.26: A singles α-spectrum of measurement.

A conceptual diagram explaining the analysis of decay-correlated events is shown in Figure. 2.27. The analysis begins with identifying candidate events by selecting α-ray signals in the energy range consistent with α-decays for the candidate nuclide. A TOF spectrum is then constructed from TOF events occurring in a "coincidence time" prior to the α-decay signal. The coincidence time is chosen according to the half-life of the analyte nuclei. If there are two or more candidate time-of-flight signals in the same region of the α-ray, it is not possible to distinguish which is responsible for the decay signal. Therefore, in order to correlate decay in an event-by-event manner, the incoming ion rate must at least 5 times lower than the inverse half-life of the nucleus is required:

$$f_{\text{ion}} \leq \frac{1}{5 \cdot T_{1/2}} \tag{2.2}$$

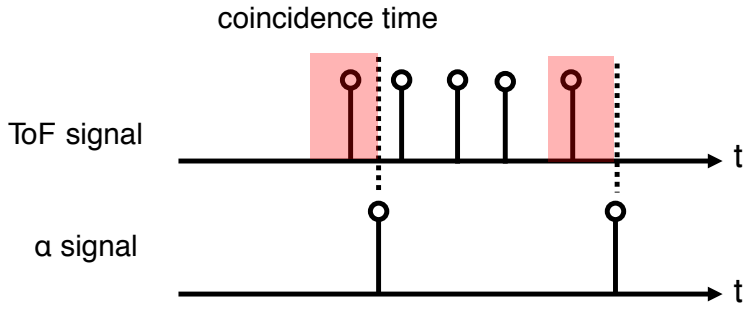

Figure 2.27: Conceptual diagram of decay-correlated analysis. We exclude time-of-flight events which do not occur in the coincidence time prior to an α-decay event.

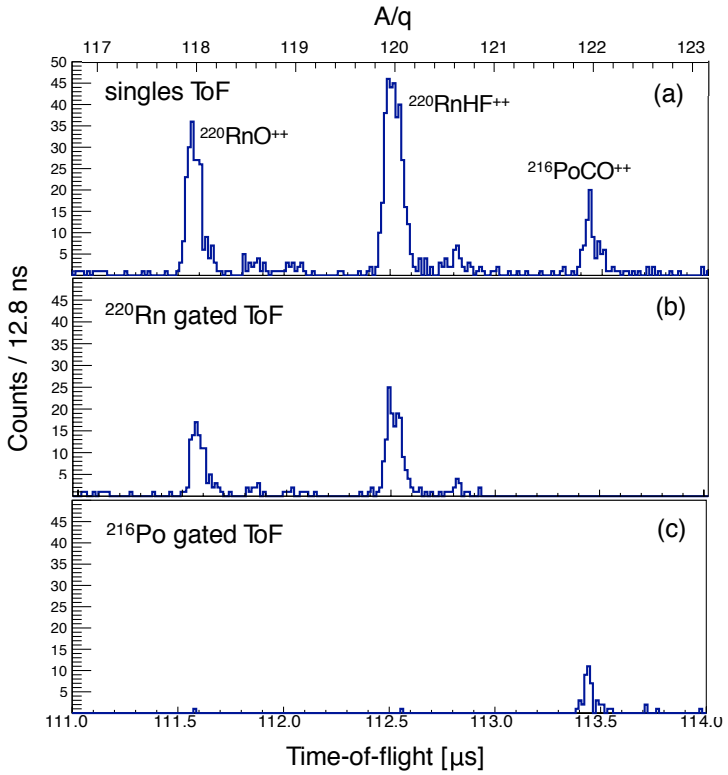

Figure 2.28: TOF spectra in the range of $A/q = 117 \sim 123$ after 12 hours of measurement. (a) Singles TOF spectrum, (b) TOF spectrum in coincidence with ^{220}Rn α-decays, using a coincidence time gate of $T_c = 180$ s and (c) TOF spectrum in coincidence with ^{216}Po α-decays, using a coincidence time gate of $T_c = 450$ ms.

Figure 2.28 shows the results of a 12 hour measurement using the ^{224}Ra radioisotope progenitor. TOF signals and α-decay signals were recorded event by event with absolute time stamps. The top panel of Fig. 2.28 shows the TOF-singles spectrum centered around the most intense peaks observed. By the use of a coincidence time gate (T_c) prior to detection of a given α-decay energy signal it is possible to discriminate between TOF events corresponding to ^{220}Rn and those corresponding to ^{216}Po, as shown in the middle and bottom panels, respectively. To identify peaks from ions constituted from ^{216}Po, a $\pm$150 keV gate was made on α-decay signals around 6.78 MeV with $T_c = 450$ ms. To identify peaks from ions constituted from ^{220}Rn, a similar gate was made on 6.29 MeV α-decay signals with $T_c = 180$ s.

Using correlated E_α-TOF measurements, it was possible to unambiguously determine that the TOF spectral peaks corresponding to $A/q = 118$ and 120 resulted from ions with a ^{220}Rn constituent, while the peak corre-

sponding to $A/q = 122$ resulted from ions with a ^{216}Po constituent. Unfortunately, the limited mass resolution of the wide mass bandwidth measurement precluded precise molecular identification. However, based on past experience we have tentatively assigned the $A/q = 118$ and 120 TOF spectral peaks to be ^{220}RnO^{++} and ^{220}RnHF^{++}, respectively, and the $A/q = 122$ spectral peak to be ^{216}PoCO^{++}.

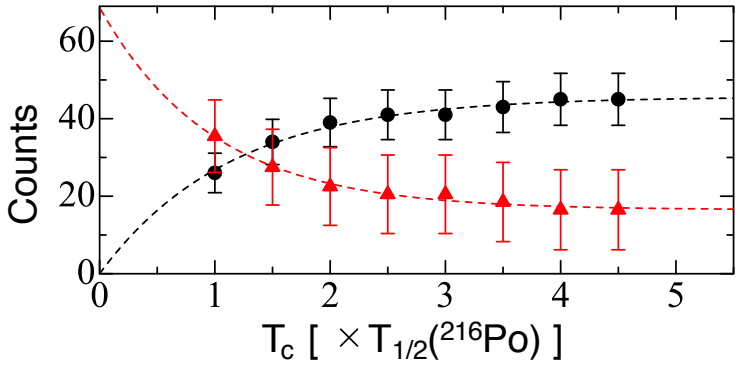

Figure 2.29: Number of correlated TOF events for ^{216}Po (black circle) and the missing TOF events (red triangle) as functions of the coincidence time in units of the half-life of ^{216}Po ($T_{1/2}$≈150 ms). The dotted lines indicate the fitted growth and decay curves. The asymptotic number of ^{216}Po events indicates an effective α detection efficiency of 44(8)%, while the asymptotic number of missing TOF events indicates a TOF detection efficiency of 84(9)%.

The data shown in Fig. 2.28 were used to determine the effective α-decay detection efficiency. Every TOF event from a radioactive ion should be followed by a subsequent α-decay. Comparing the TOF-singles counts with the E_α-TOF coincident counts in each TOF spectral peak we find that 44(8)% of TOF-singles corresponding to radioactive ions are followed by subsequent α-decays. This is consistent with the expectation of 50% effective detection efficiency based on detector solid angle.

In order to determine the TOF detection efficiency, we must consider the inverse problem: how frequently is an α-decay signal detected without a preceding conjugate TOF signal. We use the ^{216}Po for this as it is detected as a singular molecular ion and has a conveniently short half-life. Figure 2.29 shows the number of E_α-TOF correlated events and the number of α-decay events with missing TOF events as functions of the coincidence time gate. In this plot, the number of α-decay events with missing TOF events has been corrected to account for the ^{216}Po produced by decay of ^{220}Rn on

the detector, resulting in the relatively large uncertainties shown. As an internal check on the validity of the background correction, the sum of E_α-TOF correlated events and α-decay events with missing TOF events is noted to be constant as a function of the coincidence time gate duration. The TOF detector efficiency can be taken to be the ratio of the asymptotic number of E_α-TOF correlated events to the total corrected ^{216}Po α-decay events, found to be 84(9)%. This is in good agreement with the value obtained in Sec. 2.4.1.

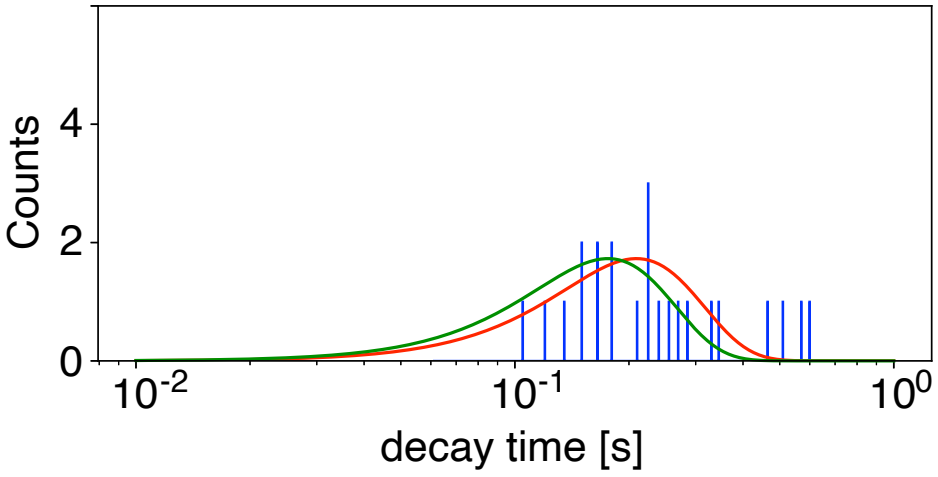

Figure 2.30: Distribution of time between TOF signal from ^{216}PoCO^{++} and subsequent α-decay signal, designated as "decay time" on the abscissa. The red line indicates a distribution curve drawn with a literature value of $T_{1/2}$ = 145 ms [96]. The green line indicates a distribution curve drawn with the experimentally obtained value of $T_{1/2}$ = 123(22) ms.

Finally, by defining the decay time as the interval between the observation of a TOF signal from a given radioactive ion and the subsequent detection of its α-decay, we demonstrate the ability to measure half-lives with the α-TOF detector. Figure 2.30 shows a plot of measured decay times for ^{216}PoCO^{++} ions along with the expected decay time distribution function based on the literature value of the half-life [96]. The maximum likelihood value of the decay constant is well-determined by the mean value of the individual decay times [97]. In this case, the mean value was determined to be τ=177(31) ms, corresponding to $T_{1/2}$=123(22) ms, which is in good agreement with the literature value of 145(2) ms [96].

2.6 Online testing

The first online experiment using the α-TOF detector was performed by using fusion evaporation products from the ^{159}Tb(^{51}V, 3n)^{207}Ra reaction.

2.6.1 Experimental setup

The setup used in the online experiment, performed at SHE-Mass-II which is a part of RIBF facility, is shown in Fig. 2.31. A primary beam of ^{51}V was prepared through MIVOC (metal ions from volatile compounds), pre-accelerated by the linear accelerator RILAC-II, and injected into the RIKEN ring cyclotron (RRC) where it was accelerated up to the 6.0 MeV/nucleon and transported to GARIS-II. The charge state of the ^{51}V beam was 13^{+}.

The ^{159}Tb targets, with an average thickness of 460-μg/cm^2 average, were produced by the sputtering method, with the terbium material deposited onto a 3.0-μm thick Ti backing foil. The ^{159}Tb targets were mounted on a 16-sector rotating target wheel, which rotated at 2000 rpm during the beam irradiation. A primary beam energy of 6.0 MeV/u is higher than optimal incident beam energy. However, the RRC could not deliver a lower energy beam and thus we also mounted 12.5-μm Al foils in the target wheel as energy degraders (Fig. 2.32) [98]. After passing through the energy degraders, the primary beam energy was 219.1 MeV at center of the targets. The typical primary beam intensity was 1.0 pμA.

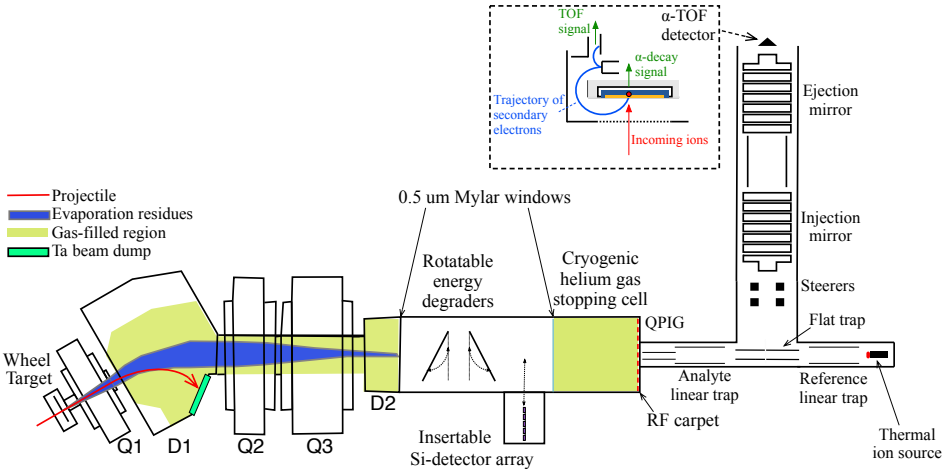

Figure 2.31: Apparatus used in online measurements. The area highlighted in yellow is the filled with He gas.

Reaction products of ^{207}Ra were efficiently transported and separated in-flight from the projectile and other background products. The magnetic rigidity of GARIS-II was set 11.5 kGauss, while the He-gas pressure was set

to 71 Pa. A secondary beam degrader composed of Mylar foils was installed in the focal plane chamber of GARIS-II. The details of the degrader are described in Chapter 3. The ERs were captured in a cryogenic He gas catcher and extracted by an rf-carpet before being further transported to the MRTOF-MS via a series of RF ion guides and multiple RF ion traps. The setup of the apparatus after the gas catcher was the same as that used in offline tests reported in Section 2.5. In this experiment, the MRTOF was optimized for 150 laps.

During these test measurements, a thermal ion source was heated inside the cryogenic-gas cell to increase the amount of background. This allowed maximum demonstration of the noise reduction capability of the α-TOF detector.

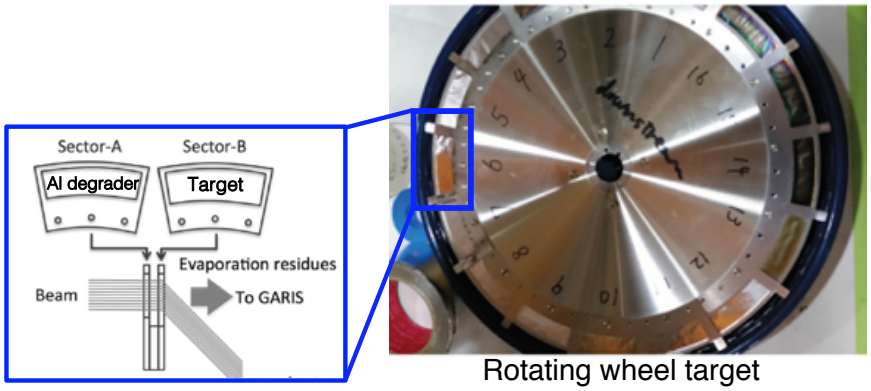

Figure 2.32: Double-layered rotating target wheel. Aluminum degraders were installed in the first layer to reduce the energy of the primary beam to an optimal incident energy.

2.6.2 Result

The α-singles spectrum obtained from the α-TOF detector is shown in Fig. 2.33. We observed the alpha signal of evaporation product ^{207}Ra and the daughter nuclide ^{203}Rn. The reaction of ^{51}V+^{159}Tb produces not only ^{207}Ra but also ^{206}Ra and ^{206,207}Fr isotopes. However, the production cross-section of ^{206}Ra is $\approx$10 times lower than that of ^{207}Ra, while Francium isotopes would not have been transported due to the RF ion trap conditions. Therefore, we could cleanly observe ^{207}Ra and its daughter nuclide.

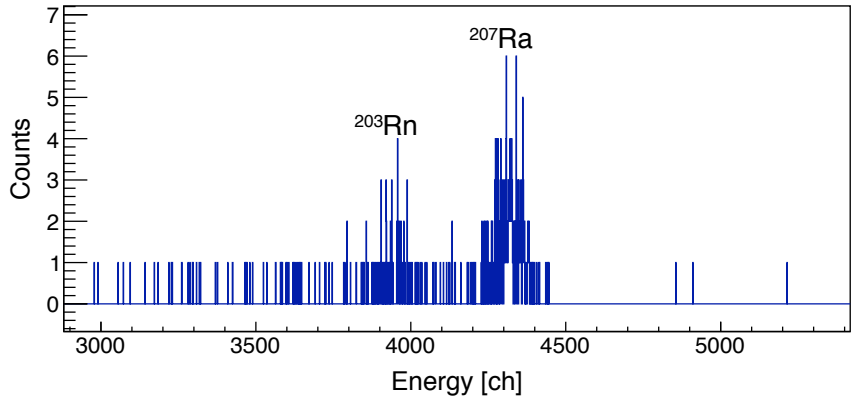

Figure 2.33: A α-singles spectrum of measurement.

The singles TOF spectrum around $^{207}Ra^{2+}$ is shown in Fig. 2.34 (a). Many background counts are seen in the raw spectrum due to the thermal ion source inside the gas-cell side. The noise count N was defined as the number of background counts in a 60 ns time-of-flight region, corresponding to the time-of-flight width of $^{207}Ra^{2+}$, near $A/q = 103.5$. The signal counts S were obtained by subtracting the noise count N from the total number of counts in the 60 ns region centered on $^{207}Ra^{2+}$. The signal-to-noise ratio (S/N) of the raw singles spectrum was 2.1.

Next, we analyzed the TOF events coincident with α-decay events from ^{207}Ra. By gating the spectrum with a coincidence time of 2.8 seconds, corresponding to two half-life periods, such backgrounds were greatly reduced. The S/N increased to 14.9, which is 7 times greater than the raw singles TOF spectrum. The gated resulted in the gated event number decreasing to 36% of the total true events, which agrees with the solid angle of the Si detector and the $2T_{1/2}$ coincidence time.

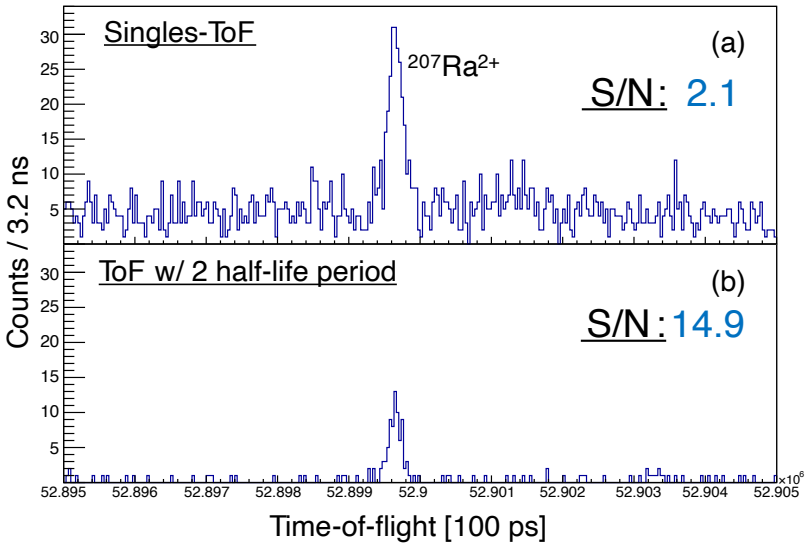

Figure 2.34: A part of the time-of-flight spectrum of ^{207}Ra. (a) The raw spectrum. (b) TOF events coincident with α-rays from ^{207}Ra observed within a coincidence time of two half-lives of ^{207}Ra.

Figure 2.35(a) shows the α-decay coincident $^{207}Ra^{2+}$ TOF counts plotted as a function of coincidence time. The rightmost circle indicates the number of $^{207}Ra^{2+}$ TOF singles counts. From this figure, it can be seen that the number of radiums increases exponentially with increasing coincidence time. This is explained by typical radioactive decay. When the coincidence time is set to 4.5 half-life periods, the coincident counts are 48.6(49)% of TOF singles counts. This agrees with the detection efficiency of 50% due to the solid angle of Si detector and the 44(8)% obtained in the offline ^{224}Ra progenitor measurements (Section 2.5).

The Figure-of-Merit(FOM) of the α-TOF detector was evaluated. The FOM is a performance index evaluated from the ratio of the detector signal to noise, especially for low counting radioisotope measurements. It is defined by Eq. (2.3). The FOM expresses the degree of the counting rate in units of the error of background count, the derivation of the equation is described in Appendix A,

$$\mathrm{FOM} = \mathrm{S}/\sqrt{\mathrm{N}}. \tag{2.3}$$

Figure 2.35 (b) shows the FOM as a function of the coincidence time. Beyond the 3.5 half-life period, the FOM decreases due to the proportion of accidental coincidences. The results indicate that a coincidence time of 2 to 3 half-life periods are appropriate in such a high background condition.

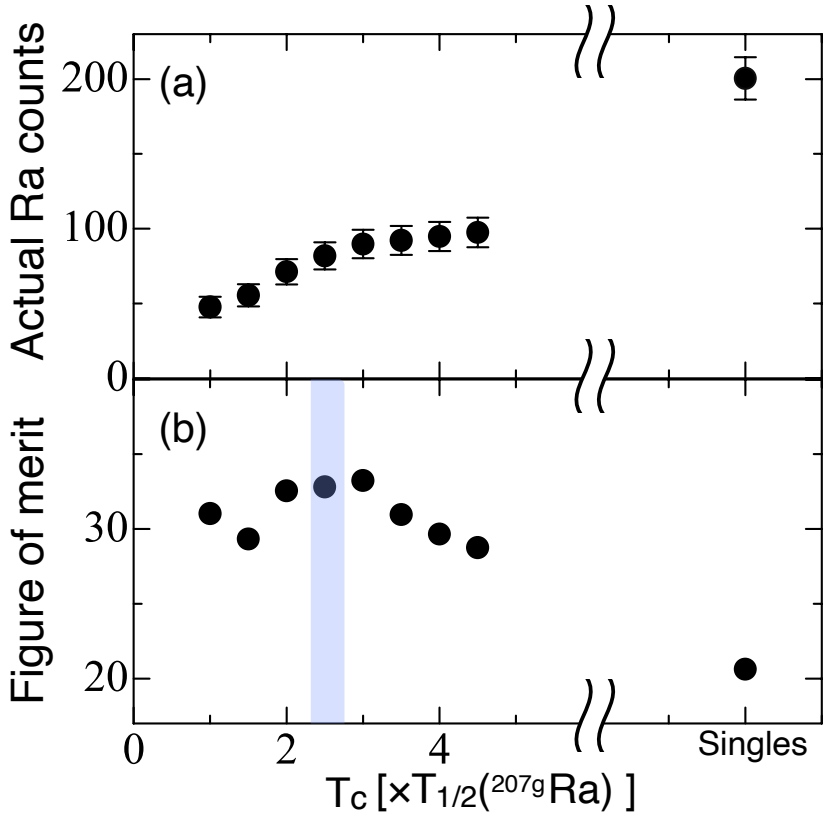

Figure 2.35: (a) Counts of ^{207}Ra as a function of T_c. (b) Figure-of-merit evaluated from these measurements.

Figure 2.36 shows the decay-correlated TOF spectrum with 4.2 second coincidence time corresponding to 3 half-life periods. The spectrum was fitted using a Gaussian-hybrid function (Eq. (2.4)),

$$f(t) = \begin{cases} Ae^{t_s(2t_c-2t+t_s)/2\sigma^2} & (t \leq t_c + t_s) \\ Ae^{-(t-t_c)^2/2\sigma^2} & (t \geq t_c + t_s) \end{cases}, \tag{2.4}$$

where A is the Gaussian peak height, t_c is the Gaussian centroid and σ is the standard deviation, t_s is the distance from t_c to the exponential tail switchover point. The peak shape parameters were determined from the spectral peak of ^{85}Rb$^+$ used as a reference ion. The result of the measurements are shown in Table 2.3. The mass excess of ^{207}Ra was determined to be 3615(83) keV which agree with the literature value of 3540(50) keV from the 2016 Atomic Mass Evaluation [25]. The statistical relative mass uncertainty was $\delta m/m$=2.1×10^{-6} in this measurement. However, the mass

excess determination included the contribution of an inseparable isomeric state. A more precise follow-up measurement is described in Chapter 3.

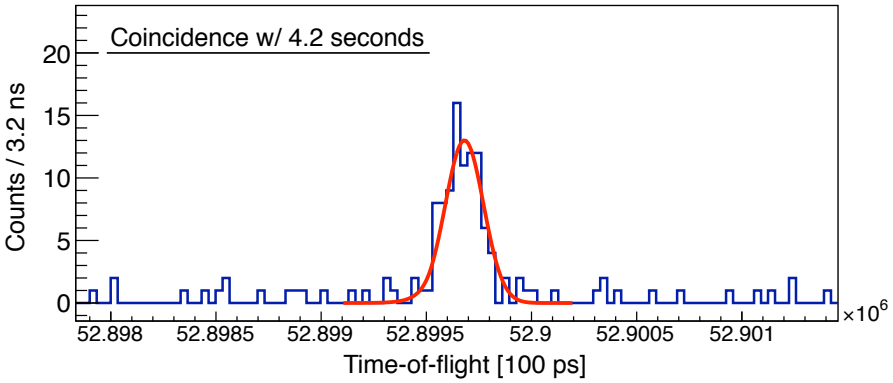

Figure 2.36: Time-of-flight spectrum from coincidence evaluation with coincidence time of 4.2 seconds, corresponding to 3 half-life periods of ^{207g}Ra.

Table 2.3: Mass excess of ^{207g}Ra determined in this measurement, AME16 literature value, and deviation between our measurement and the literature value.

	ME_{EXP} [keV]	ME_{AME2016} [keV]	ΔME [keV]
^{207g}Ra	3615(83)	3540(50)	75(83)

Figure 2.37 shows the logarithmic distribution of the decay times for decay-correlated TOF events. The red and green curves represent expected distributions based on literature values. Although ^{207m}Ra cannot be discriminated due to its small α-branching ratio, the decay time distribution does agree with that expected for ^{207g}Ra. Based on this distribution, we evaluated the decay time to be 1.91(19) seconds, which corresponds to a half-life of 1.33(13) seconds, in good agreement with the literature value of 1.35(22) seconds. From the online test, we confirmed that the α-TOF detector can reduce the background in a time-of-flight spectrum and obtain decay properties of short-lived nuclei. This allows for both accurate mass and half-life measurements from decay correlated events.

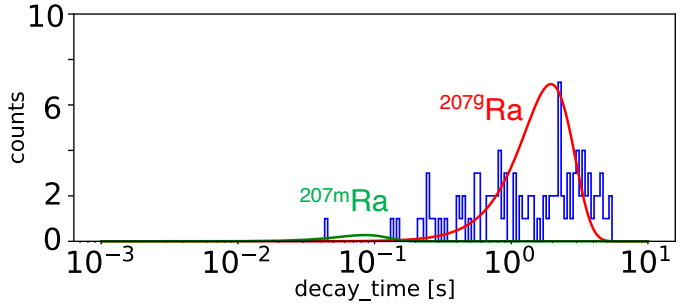

Figure 2.37: The decay time distribution of ^{207}Ra events.

2.6.3 Anticipated application for nuclear decay spectroscopy

Let us consider possible applications to nuclear spectroscopy study by correlation measurement of mass and decay properties using the α-TOF detector. Using all the information, i.e. time-of-flight, decay energies, and decay times obtainable using the α-TOF detector, if one or more states - ground state and/or isomeric state - undergo alpha decay, it is possible to discriminate in cases where the energy of the alpha decay differs from other alpha particle energies – background or other states – by at least 150 keV. When multiple states undergo alpha decay, there is furthermore the ability to separate states with sufficiently different half-lives. To understand the limits of these abilities, we performed numerical simulations using the performance parameters measured in the characterization tests. An example data set is made into a three-dimensional parameter space diagram in Fig. 2.38. These nuclides are clearly separated, as is evident from the 3D diagram. By application of appropriate gates, it would be possible to determine the mass of a single state and derive the excitation energy from the decay-correlated mass measurements.

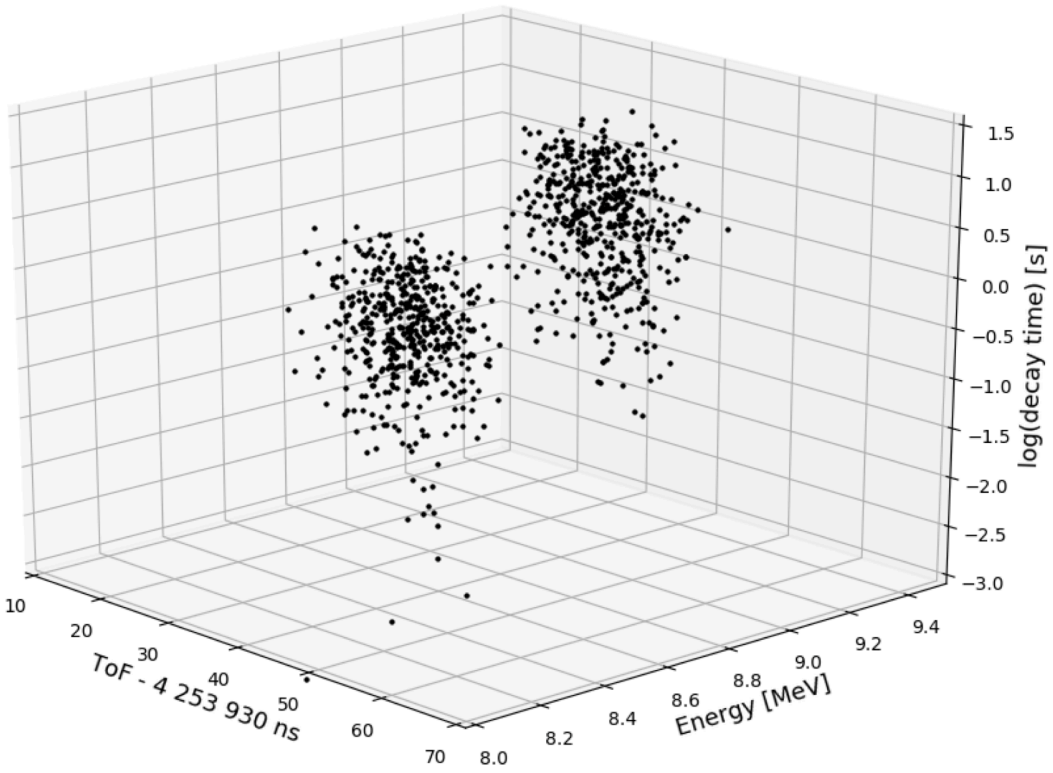

Figure 2.38: Three-dimensional mapping of numerical simulation. The postulated nucleus having an isomeric state at 500 keV above the ground state, with the two states having similarly differing α-decay energies of 8.5 MeV and 9.0 MeV, and with the half-lives of the ground state and isomer being 0.67 seconds and 5.0 seconds, respectively. Decay properties (decay energies and decay time) and time-of-flight can be considered independently in an event by event analysis.

Although nuclear spectroscopy measurements by such a decay-correlation method have a vast range of applicability for any α-decaying nuclides, we will limit ourselves to consideration of candidate nuclides to be measured in the region of superheavy nuclei in order to fully utilize the discrimination capability in such rare events by use of the α-TOF detector. The decay properties of the candidate are shown in Table 2.4. Numerical simulations were performed to show the possibility of using their decay properties to resolve the ground state from isomeric states in the time-of-flight spectra of ^{263}Sg and ^{267}Hs, and thereby disambiguate the state ordering. Since superheavy nuclei are expected to be extracted from the gas cell in a doubly charged [73], we performed simulations based on doubly charged ions.

Table 2.4: Candidate nuclides for spectroscopic measurement with MRTOF+α-TOF detector in the superheavy elements region. Observed α-decay energies and the half-lives are listed.

Nuclide	E_α [MeV]	$T_{1/2}$	Ref.
^{267g}Hs	9.88	52^{+13}_{-8} ms	[99, 100]
^{267m}Hs	9.73	$0.8^{+3.8}_{-0.37}$ s	[99, 100]
^{262a}Bh	10.06	83±14 ms	[101]
^{262b}Bh	10.37	22±4 ms	[101]
^{263a}Sg	9.06	$0.82^{+0.37}_{-0.19}$ s	[102, 103]
^{263b}Sg	9.25	310^{+160}_{-80} ms	[102, 103]
^{257g}Rf	8.78	5.5±0.4 s	[104]
^{257m}Rf	9.02	4.9±0.7 s	[104]

Simulation of ^{263}Sg

^{263}Sg isotopes are reported to exhibit two distinct α-decays, with energies of 9.06 MeV and 9.25 MeV. However, which decay is from the isomeric state and which is from the ground state has not been determined. These two energy states are tentatively classified as ^{263a}Sg and ^{263b}Sg. Lacking contrary evidence, in the numerical simulations we performed, it was presumed that the mass difference between the two states was equal to the difference in α-particle energies; it was further presumed that ^{263a}Sg represents the ground state and ^{263b}Sg represents the isomer. The isomeric state population was presumed to be 10%. The simulation results for 100 events are shown in Fig. 2.39.

For an MRTOF-MS operating with a mass resolving power of R_m=200,000, the $^{263a,b}Sg^{2+}$ peak in the time-of-flight spectrum would be fully unresolved. However, the α-decay spectrum would be resolvable, as shown in Fig. 2.39 (b). By either correlation of TOF signals based on α-decay energy or use of a two-dimensional Gaussian fit (Fig. 2.39 (c)), it would be possible to discern the atomic mass of each state and assign state ordering unambiguously.

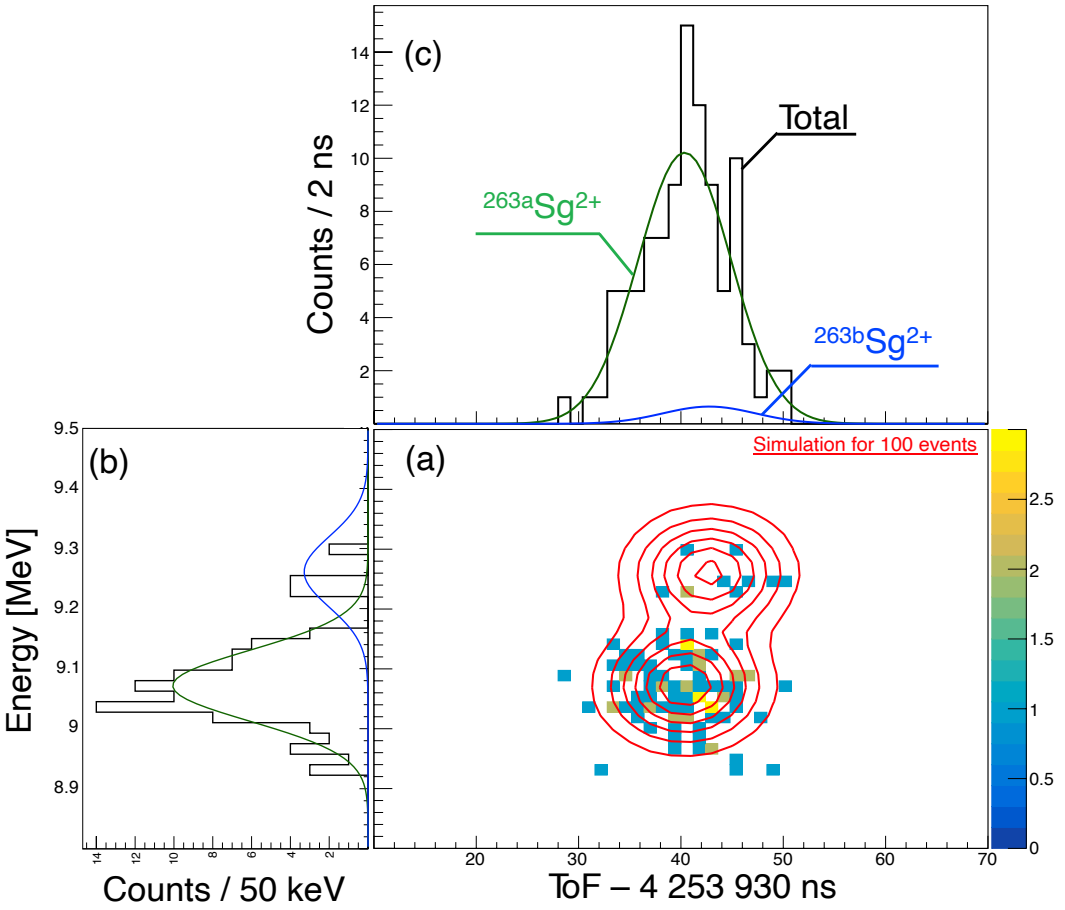

Figure 2.39: Numerical simulation of ^{263}Sg showing (a) the simulated two dimensional mapping of time-of-flight and α-energy, and the projection to (b) α-decay energy and (c) time-of-flight spectra. The red lines in (a) are equal intensity contours resulting from the two-dimensional fit. In (b) and (c) the green lines indicate the excited state and blue line indicates the ground state.

Simulation of ^{267}Hs

Let us next consider the ^{267}Hs isotope. In the case of this nuclide, the α-decay energies of 9.88 MeV and 9.73 MeV emitted from the two states ^{267a}Hs and ^{267b}Hs would not be sufficiently resolvable by present α-TOF detector. However, since the half-lives of the ground state and the isomeric state are different greatly – 52 ms and 0.80 s – it is possible to distinguish between the two states based on the difference in their half-lives. Figure 2.40(a) shows the numerical simulation data in terms of a scatter plot of the TOF versus decay time of ^{267}Hs^{2+}, where the decay time is again defined to be the time

interval between the ion impact signal (TOF event) and the alpha decay signal. Within 200 ms of the arrival of the ions at the α-TOF detector, 94% of the ^{267g}Hs will decay. At the same time, less than 20% of the ^{267m}Hs will decay. Thus, by gating on the alpha events that occur more than 200 ms after the TOF signal is observed, the TOF spectrum produced by the ^{267m}Hs ion can be generated as shown in Fig. 2.40 (b), and the excitation energy of the isomer can be directly determined.

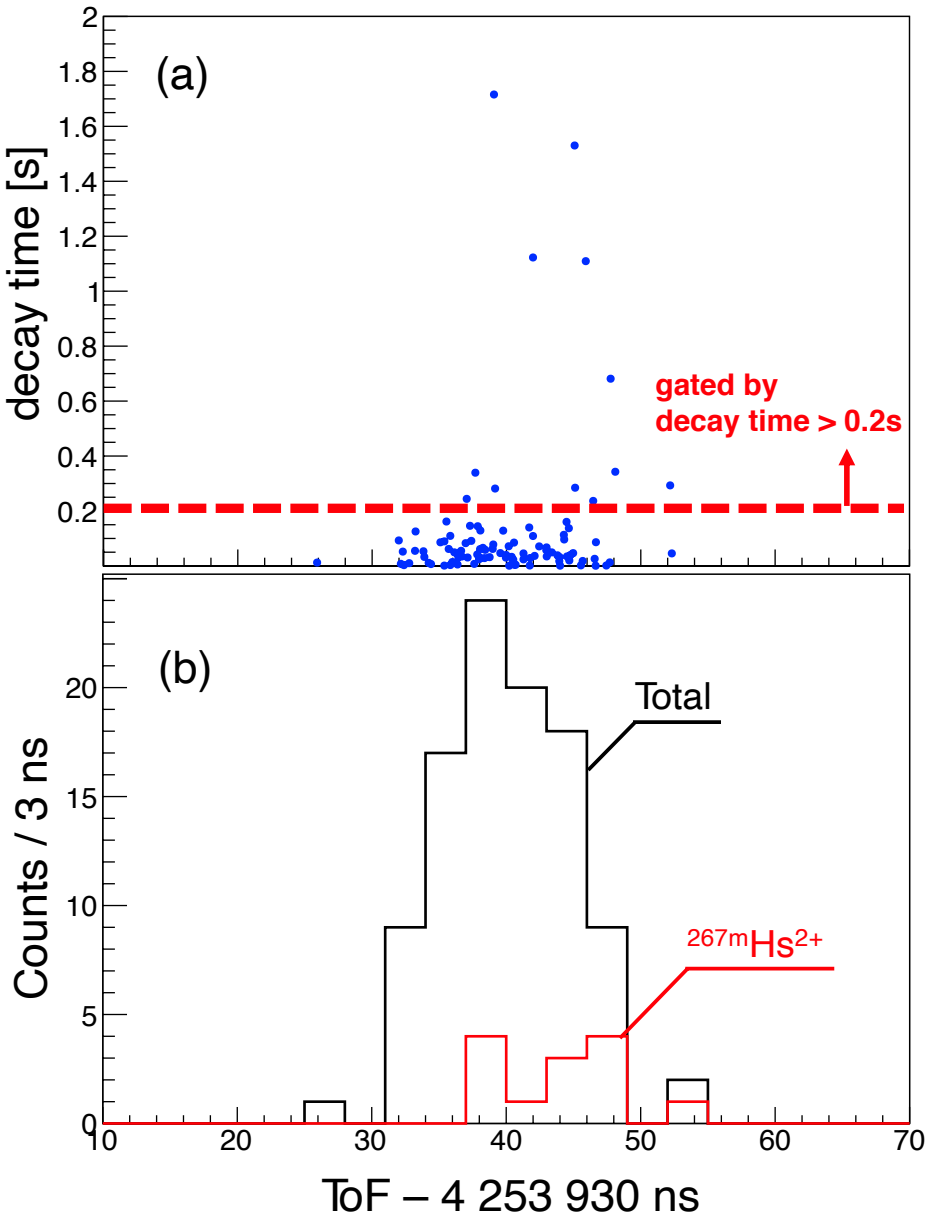

Figure 2.40: Numerical simulation of ^{267}Hs for time-of-flight and decay time. (a) Two dimensional scatter plot of time-of-flight and decay time, red dashed line indicates a lower gate line to extract isomeric state components. (b) Time-of-flight spectra without decay time gating (black) and with decay time gate of t_{decay}>200 ms (red).

There is a long history of decay spectroscopy using mass separators [105, 106, 107]. These measurements have always been continuous, and the mass

spectrometer has provided a one-way advantage for the application of decay spectroscopy. Here, we demonstrate a paradigm shift in which mass spectrometry and decay spectroscopy work synergistically to benefit each other. Mass measurement and decay spectroscopy can now be performed simultaneously, and correlations between the two can be used to accurately identify rare events and improve the reliability of their mass and half-life measurements.

Chapter 3

Mass measurement of ^{206,207}Ra

In the online experiments described in Chapter 2, the capability of the α-TOF detector was evaluated from the mass and decay correlated measurement of ^{207}Ra produced by the ^{51}V+^{159}Tb reaction. However, there are some isomeric states in ^{207}Ra that are difficult to separate with the current mass resolving power of MRTOF-MS ($R_m \approx 200,000$).

In this chapter, to further demonstrate the possibility for nuclear spectroscopy with mass and decay correlated measurements, the excitation energy of the ^{207m}Ra is directly determined by combination of the TOF information with the correlated α-decay properties obtained using the α-TOF detector.

3.1 Decay properties of $^{207g/m}$Ra

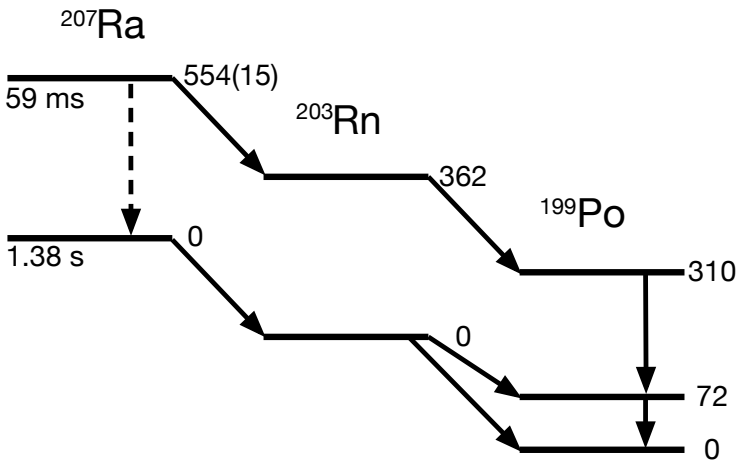

Figure 3.1: Decay scheme of ^{207}Ra. The half-lives of ^{207}Ra isomer and ground state, and the excitation energy of each nuclear state are taken from [108].

The decay scheme of ^{207}Ra is shown in Fig. 3.1. The mass of ^{207}Ra is indirectly determined from two sequential α-decays leading to ^{199}Po whose mass has been directly determined. The production ratio ^{207g}Ra/^{207m}Ra is known to be 0.75/0.25 in the reaction system of ^{154}Sm + ^{58}Fe [109]. Based on α-decay spectroscopy studies of ^{207m}Ra, it is suggested that the primary decay mode is internal conversion to the ground state. Similar to the mass of the ground state, the excitation energy of ^{207m}Ra has only been indirectly determined by two sequential α-decays to and two γ-decays from ^{199}Po. The spin-parity of the isomeric state was tentatively assigned to J^{π}=13/2 based on systematics [108] .

3.2 Experiment

An experiment was performed using the same setup and reaction presented in Section 2. In this follow-up study, the MRTOF was optimized for 266 laps. For the event-by-event correlation of ^{207m}Ra, the incoming rate at the MRTOF was limited to about 0.2 cps by controlling the primary beam current at approximately 100 pnA.

3.2.1 Energy calibration of α-TOF detector

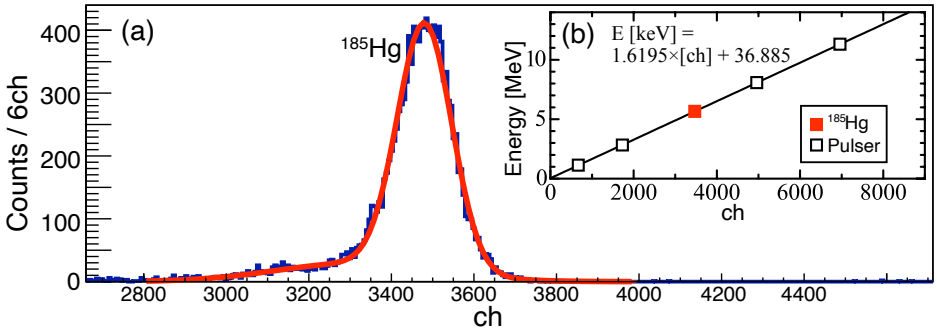

Figure 3.2: (a) Measured alpha-decay spectrum of ^{185}Hg produced in the ^{139}La(^{51}V, 5n) reaction and used for energy calibration of the α-TOF detector. (b) The calibration curve with fitting results. The red dot indicates the decay energy of ^{185}Hg. The black dots were obtained by using a pulser for energy calibration.

For energy calibration of the α-TOF detector and tuning of the MRTOF system, ^{185}Hg was produced by the ^{139}La(^{51}V, 5n) reaction with ^{nat}La targets and transported to the MRTOF. Despite the alpha decay branching ratio of ^{185}Hg being only 6%, the high fusion cross section of a few millibarn allowed for efficient data acquisition for tuning and energy calibration. The α-decay spectrum measured by the α-TOF detector is shown in Fig. 3.2 (a). Using a pulser, we generated a signal equal to a constant multiplication of the alpha decay energy of ^{185}Hg in order to make the energy calibration. The calibration curve is shown in Fig. 3.2 (b). The calibration equation obtained from linear fitting was

$$\text{Energy[keV]} = 1.6195 \times [\text{ch}] + 36.885. \tag{3.1}$$

The energy of an α-decay detected by the α-TOF detector is determined from this equation. Based on a comparison with the yield of ^{185}Hg acquired at the focal plane of GARIS-II, the transport efficiency of the MRTOF system was estimated to be 4%∼5%.

3.2.2 Secondary energy degrader optimization

The first step in the online tuning of the system is to optimize the thickness of the Mylar foil degrader in the focal plane chamber to maximize ion stopping efficiency in the cryogenic gas cell. The thickness of the Mylar foil

was scanned and rate of desired analyte ions detected in the MRTOF time-of-flight spectrum recorded for each degrader thickness. The result is shown in Fig. 3.3 in terms of relative intensity as functions of degrader thickness.

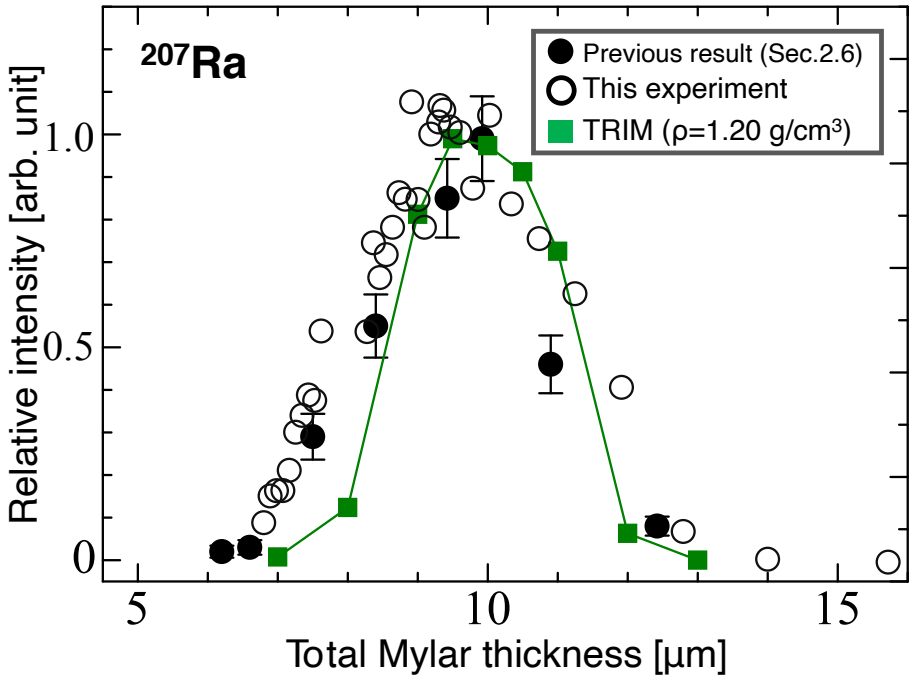

Figure 3.3: The result of scanning the thickness of the Mylar secondary energy degrader for ^{207}Ra.

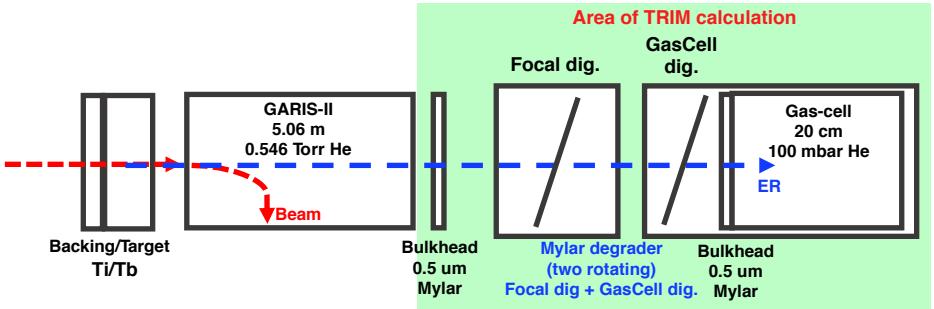

Figure 3.4: Configuration of the TRIM calculation. The green highlighted region was used for the TRIM calculation, which simulates the energy degradation of the particles after passing through GARIS-II.

The closed black circles in Fig. 3.3 are the data obtained in the online test experiment presented in Chapter 2, while the open circles are the data

acquired in this experiment. Although the absolute transport efficiencies in the two experiments are different, both experimental results show the same trend. Green squares are the result of a Monte Carlo simulation using TRIM [110]. The TRIM calculations were performed based on a Mylar density of 1.2 g/cm^3 (standard value is 1.4 g/cm^3) in order to reproduce the experimental values. The simulation configuration used in the TRIM calculation is shown in Fig. 3.4. The Green highlighted area indicates the region of calculation. Total Mylar thickness in Fig. 3.3 is defined as the sum of the variable Mylar foil in the focal plane and the GARIS-II vacuum bulkhead and gas cell bulkhead Mylar foils (Both of 0.5μm). Based on these results the experiment was performed with the total Mylar thickness set to 9.6 μm.

3.3 Results

The full range time-of-flight spectrum at two different lap numbers are shown in Fig. 3.5. Initially, the MRTOF was set to release ions to the α-TOF detector after $^{207}Ra^{2+}$ made 266 laps. Such data were accumulated for 6 hours. Afterwards, in order to confirm the spectra, we changed the MRTOF timing to release ions after 265 laps and accumulated data for 1 hour. The time-of-flight drift during the measurement was compensated for by concomitantly measured $^{85}Rb^{+}$ ions from a thermal reference ion source, using the method in Fig. 1.27 (a), using 7.5 s correction periods. It was possible to identify $^{207}Fr^{2+}$, $^{207}Ra^{2+}$ and $^{206}Fr^{2+}$, $^{206}Ra^{2+}$ in the spectra at both numbers of laps. The α-spectrum after the 6 hour measurement is shown in Fig. 3.6. Directly transported ^{207}Fr, $^{207g/m}$Ra, and ^{206}Fr, ^{206}Ra, and their daughters/granddaughters, Rn, Po, and At isotopes were observed. Figures 3.6 (b) and (c) show the α-decay spectra correlated with the TOF signals of $^{207}Ra^{2+}$ and $^{206}Ra^{2+}$, where the gate of the correlation is set $E_\alpha \geqq$7.0 MeV to avoid contamination by the random correlation with the decays of ^{207}Fr. The decay energies of $^{207g/m}$Ra and ^{206}Ra were measured to be 7.132(92) MeV, 7.346(92) MeV, and 7.250(140) MeV, respectively. These values are tabulated in Table 3.1. These measurements are in agreement with literature values derived from precise α-decay measurements.

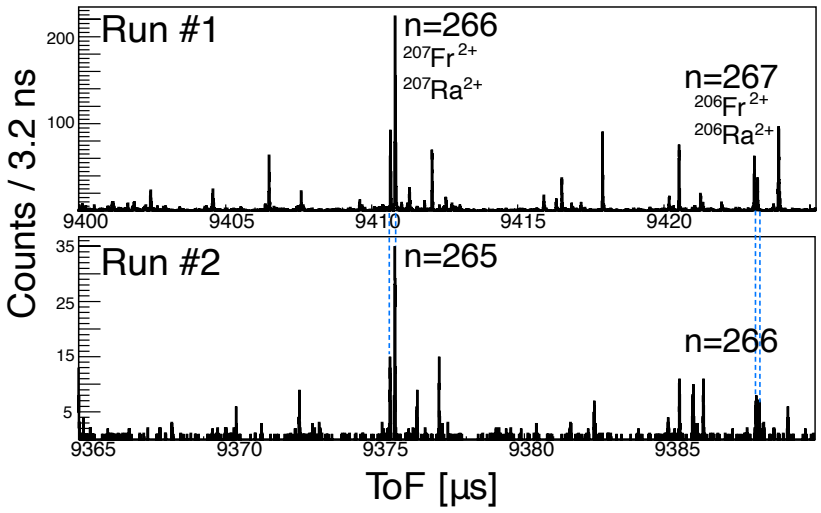

Figure 3.5: The full-range time-of-flight singles spectra after two different numbers of laps in the MRTOF. The upper panel shows the result of a 6 hour measurement and the lower panel shows the result of a 1 hour measurement. Many peaks from stable molecular contaminants were observed; typically they are making a different number of laps and none of them were correlated with α-decay energy gates.

Table 3.1: The decay energies of Ra isotopes obtained in this experiment. The literature values are taken from [111].

	$E_{\alpha,\mathrm{EXP}}$ [MeV]	$E_{\alpha,\mathrm{Lit}}$ [MeV]
^{206}Ra	7.250(140)	7.269(4)
^{207g}Ra	7.132(92)	7.131(5)
^{207m}Ra	7.346(92)	7.320(20)

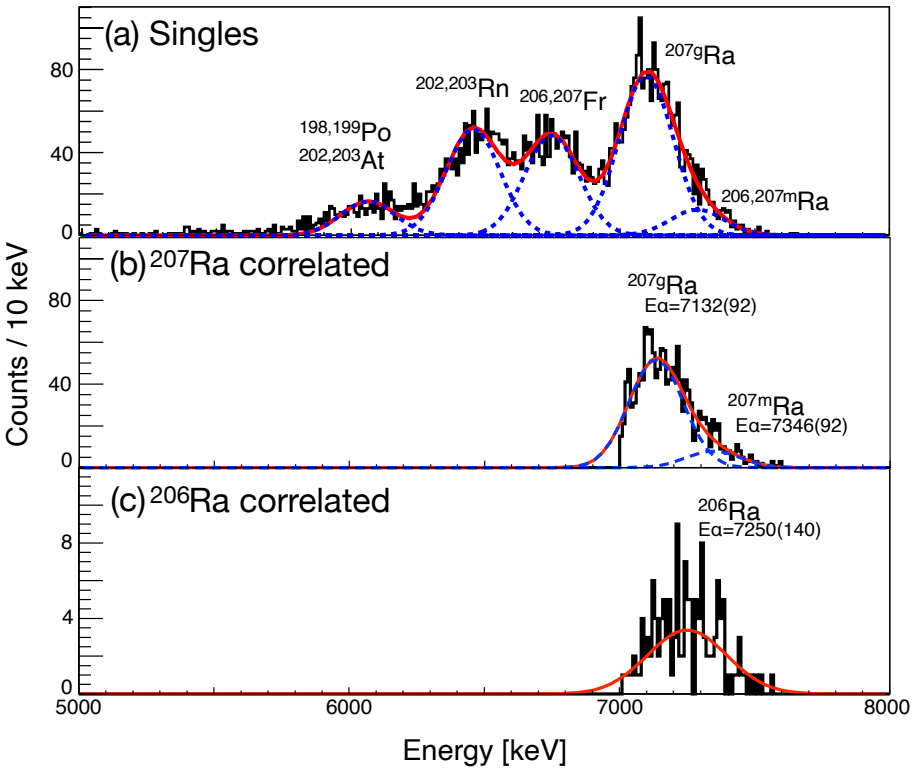

Figure 3.6: The alpha-decay spectra obtained from the α-TOF detector during a 6 hour measurement. (a) The α-decay singles spectrum. (b) The α-decay spectrum correlated with TOF signal of $^{207}Ra^{2+}$. (c) The α-spectrum correlate with TOF signal of $^{206}Ra^{2+}$.

3.3.1 Analysis of ^{206}Ra

Figure 3.7 shows the time-of-flight spectra around $^{206}Fr^{2+}$, $^{206}Ra^{2+}$ isotopes with different two laps. Black histogram indicate the singles spectrum and blue histogram indicate the decay correlated time-of-flight histogram.

The reported half-life of ^{206}Ra is 240(20) ms, hence the coincidence time was set to 1 second corresponding to about 4 half-life periods. There were 162 decay-correlated TOF events out of 327 TOF singles events. The fraction of correlated events was 49(5)%, agreeing with the α-TOF efficiency as reported in Chapter 2.

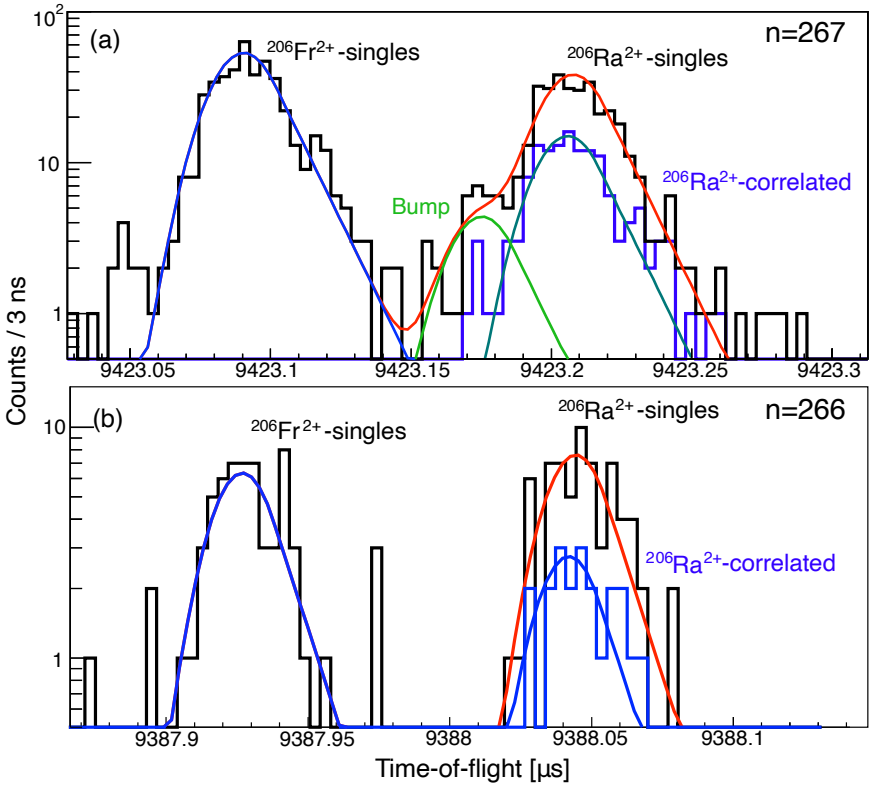

Figure 3.7: The TOF singles (black) and ^{206}Ra α-decay gates (blue) spectra in the vicinity of ^{206}Ra region for two different numbers of laps: (a) 267 laps and (b) 266 laps.

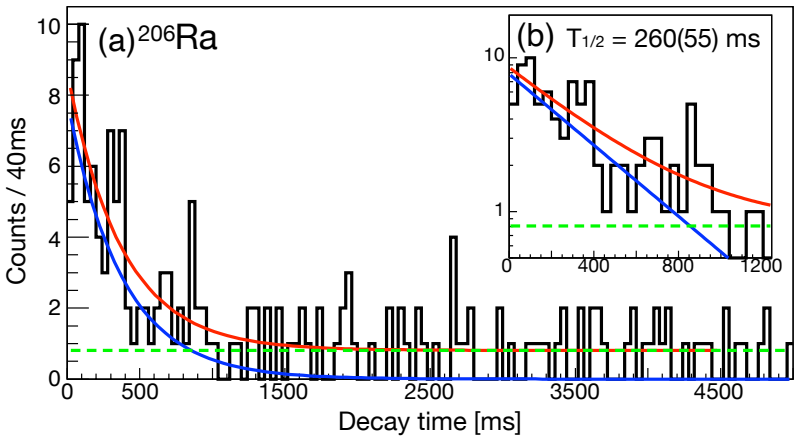

Figure 3.8: Decay time spectrum as a histogram of the time interval between the time-of-flight signal and the correlated α-energy signal. The half-life of ^{206}Ra was determined to be 260(55) ms by fitting this data to an exponential plus constant background (red curve).

The time-of-flight spectra were fitted using an asymmetric Gaussian-hybrid function [112],

$$f(t) = \begin{cases} Ae^{\delta_L(2t-2t_c+\delta_L)/2\sigma^2} & (t \leq t_L) \\ Ae^{-(t-t_c)^2/2\sigma^2} & (t_L < t < t_R) \\ Ae^{\delta_R(-2t+2t_c+\delta_R)/2\sigma^2} & (t \geq t_R) \end{cases}, \tag{3.2}$$

where A is the Gaussian peak height, t_c is the Gaussian centroid and σ is the standard deviation, onto both side of Gaussian shape the function changes smoothly into exponential curves at switching point, $t_L = t_c - \delta_L$ on the left side and $t_R = t_c + \delta_R$ on the right side, respectively. At 267 laps, a spurious spectral peak (labeled "Bump" in Fig. 3.7(a)), which is presumed to be a stable molecular ion making a different lap numbers, was found on the left side of ^{206}Ra^{2+}. Therefore, the fitting of singles spectrum include a bump structure. In order to preclude any mass-dependent systematic errors, ^{206}Fr^{2+} was used as an isobaric reference. The fitting was done for ^{206}Fr^{2+} and ^{206}Ra^{2+} and bump structures at once to determine the shape of the fitting function and the time-of-flight ratio (ρ) and their fitting errors at the same time. The ROOT macro for this fitting is describe in Appendix B.1.

The results of fitting the 267 laps TOF singles spectral peaks of ^{206}Fr^{2+} and ^{206}Ra^{2+} yielded a TOF ratio $\rho = 1.000012462(142)$, which corresponds to a mass excess of 3540(54) keV/c^2. Repeating the fitting procedure using decay-correlated TOF spectrum yielded a TOF ratio ρ =1.000012256(270), corresponding to a mass excess of 3461(103) keV/c^2. Additionally, a half-life analysis was performed using the TOF-gated decay time spectrum. The

Table 3.2: The measured time-of-flight ratio ρ of $^{206}Ra^{2+}$ ion to the reference ion ($^{206}Fr^{2+}$) and the obtained mass excess (ME) of ^{206}Ra with different two laps. The mass deviations (ΔME) are comparisons with the literature value ME_{Lit} in AME2016 [25].

laps(gate)	ρ	ME_{EXP} [keV]	ΔME [keV]
267(singles)	1.000012462(142)	3540(54)	−26(54)
267(correlated)	1.000012256(270)	3461(103)	−105(103)
266(singles)	1.000012604(340)	3594(130)	28(130)
266(correlated)	1.000012249(556)	3458(213)	−107(213)

decay times of all correlated events are compiled in Fig. 3.8 as a histogram. The exponential fitting gives a half-life of $T_{1/2}$=260(55) ms. This confirms that the α-decay signals which were correlated with the time-of-flight spectral peak definitively originated from ^{206}Ra.

The same mass analysis was performed for the 266 lap spectrum for confirmation. The time-of-flight ratios in this case were evaluated to be ρ=1.000012604(340) from singles TOF spectrum and ρ=1.000012249(556) from decay correlated time-of-flight signal, corresponding to mass excess of 3594(130) keV and 3458(213) keV, respectively.

Table 3.2 summarizes the mass analysis results for $^{206}Ra^{2+}$. For the results of 267 laps with the higher statistics, the deviation from the literature value of mass excess, 3540(54) keV/c^2, was −26(54) keV in singles events and −105(103) keV in decay correlated events. In both cases, the result agrees with literature values within statistical error, indicating that accurate masses can be derived from decay correlated TOF spectra.

3.3.2 Analysis of ^{207}Ra

Figure 3.9 shows the time-of-flight spectra near the expected time-of-flight for $^{207}Fr^{2+}$ and $^{207}Ra^{2+}$ making 266 laps (Run #1). In the spectrum, we show the singles events overlapped with the decay correlated events of ^{207}Ra. As the incoming rate of ^{207g}Ra was slightly excessive compared the decay rate, we could not perform decay-correlated time-of-flight spectroscopy for that species. Therefore, we focused on ^{207m}Ra, which has been reported to have a short half-life. To avoid contamination by ground state, an energy gate of E_α>7.32 MeV was used, corresponding to 2σ from the center of the alpha decay energy of the ground state of ^{207}Ra. The coincidence time gate was set to T_c<180 ms, corresponding to three half-life periods of ^{207m}Ra.

The fitting of the TOF spectrum was done simultaneously for $^{207g/m}Ra^{2+}$ TOF singles, decay-tagged $^{207m}Ra^{2+}$ events, and $^{207}Fr^{2+}$ TOF singles which

served as the isobaric mass reference in one function, to determine the fitting shape and the center position of the each states of ^{207}Ra. By sharing parameters between the singles ^{207}Ra and the decay correlated ^{207}Ra, the position of the isomer is determined with high accuracy from the decay tagged event as fitting with high statistics singles events determined the shape parameters with high-precision. The ROOT macro for this fitting is described in Appendix B.2. The decay tagged ^{207}Ra spectrum is mostly attributed to the isomeric state, however a 14% ground state contribution is estimated from the energy and decay time gates. Therefore, the fitting took into account this admixture of the ground state.

Since the ratio of ground state to isomer can be unambiguously determined from the TOF spectrum, it is also possible to derive the alpha-decay partial half-life of the isomer. Identical fittings were performed for different decay time gates. Figure 3.10(a) shows the mass excess of ^{207g}Ra obtained by fitting, and Fig. 3.10 (b) shows the excitation energy of ^{207m}Ra as a function of coincidence time gate. Black circle indicates the literature value and the area highlighted in green indicates the error band of literature value. With appropriate fitting, the results are consistent within the error obtained at any coincidence time. Figure 3.10 (c) shows the reduced chi squared for each fitting. Based on chi-squared analysis, the value when the coincidence time is 180 ms, corresponding to 3 half-life periods, was adopted. The results were analyzed with a coincidence time of 180 ms, yielding a time-of-flight ratio of ρ=1.000016550(38) with reference species ^{207}Fr^{2+} and a mass excess and excitation energy of ^{207m}Ra of 3538(15) keV/c^2 and 552(42) keV, respectively. These values are consistent with those determined indirectly by α-decay spectroscopy. A summary of mass analyses is shown in Table 3.3.

Furthermore, a half-life of ^{207m}Ra was determined by decay correlated TOF events. The decay time distribution for an energy gate of $E_\alpha \geq 7.32$ MeV is shown in Fig. 3.11. The fitting result showed the half-life of ^{207m}Ra to be 55(9) ms. This value agrees with the literature value of 59(4) ms [108].

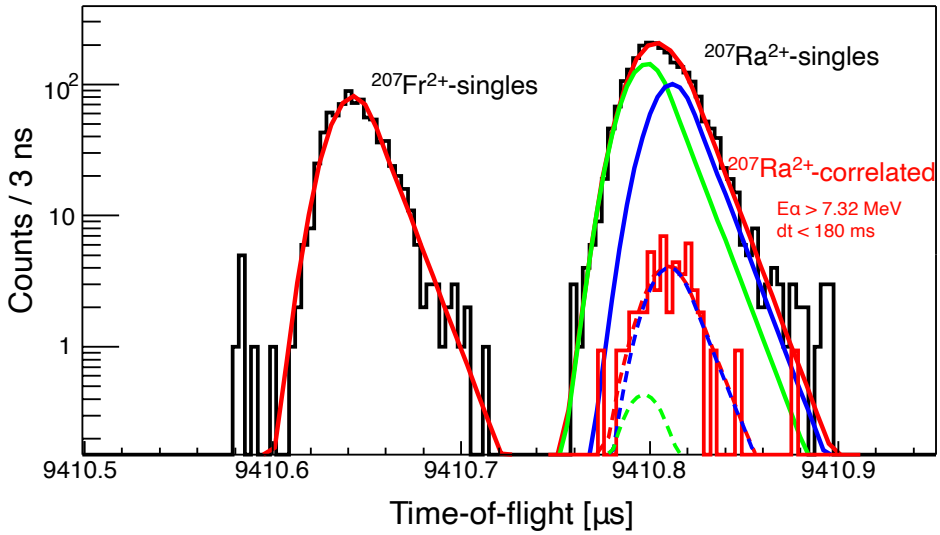

Figure 3.9: The time-of-flight spectrum around $^{207}Ra^{2+}$ region along with the fitting results. The dashed blue line indicates the decay tagged events with E_α above 7.32 MeV and decay time below 180 ms.

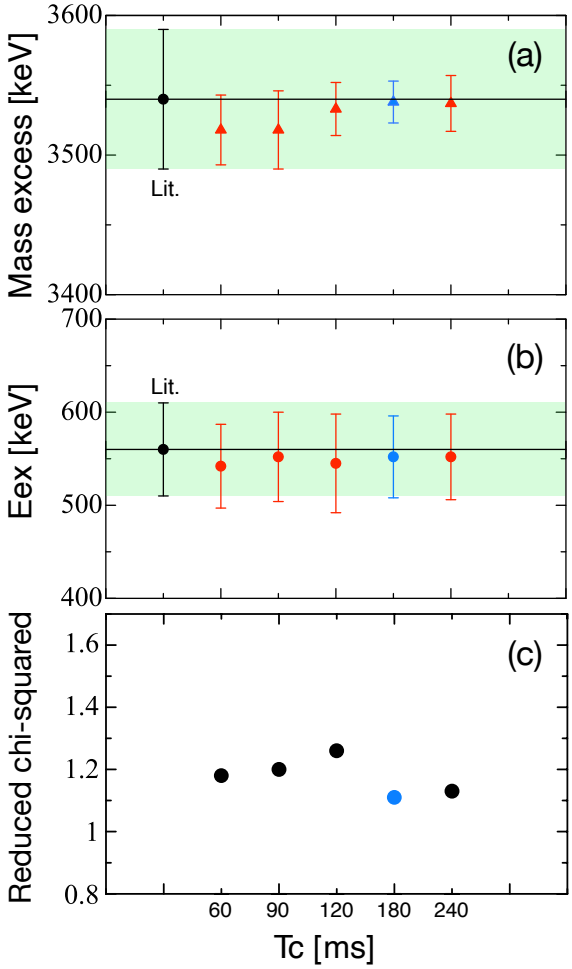

Figure 3.10: (a) The mass excess of ^{207m}Ra as a function of T_c. (b) Excitation energy of ^{207m}Ra obtained by mass decay correlated analysis. (c) Reduced-χ^2 of each fitting.

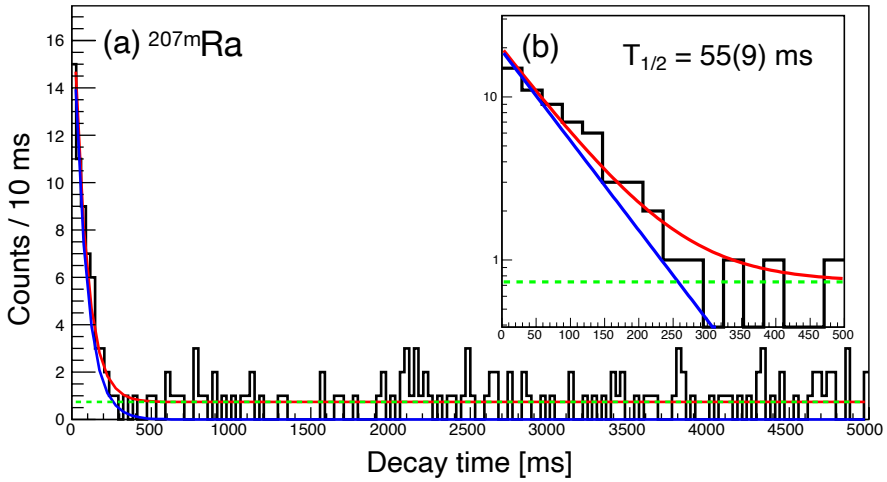

Figure 3.11: The decay time distribution of ^{207m}Ra gated by $E_\alpha \geq 7.32$ MeV. The dashed green lines indicate the constant background events while the solid blue lines indicate the analyte component of ^{207m}Ra and the solid red line represents their sum. (a) Full range spectrum up to 5 seconds, linear scale. (b) First 500 ms, logarithmic scale.

Table 3.3: The measured time-of-flight ratio (ρ) and calculated mass excess of ^{207m,g}Ra.

	Ref.	T_c [ms]	ρ	ME_{EXP} [keV]	E_{ex} [keV]	χ^2_ν
$^{207g}Ra^{2+}$	$^{207}Fr^{2+}$	60	1.000016501(64)	3518(25)		1.18
$^{207m}Ra^{2+}$			1.000017905(97)	4060(37)	542(45)	
$^{207g}Ra^{2+}$	$^{207}Fr^{2+}$	90	1.000016500(74)	3518(28)		1.20
$^{207m}Ra^{2+}$			1.000017932(102)	4070(39)	552(48)	
$^{207g}Ra^{2+}$	$^{207}Fr^{2+}$	120	1.000016539(50)	3533(19)		1.26
$^{207m}Ra^{2+}$			1.000017952(131)	4078(50)	545(53)	
$^{207g}Ra^{2+}$	$^{207}Fr^{2+}$	180	1.000016550(38)	3538(15)[a]		1.11
$^{207m}Ra^{2+}$			1.000017983(109)	4090(42)	552(42)[a]	
$^{207g}Ra^{2+}$	$^{207}Fr^{2+}$	240	1.000016548(52)	3537(20)		1.13
$^{207m}Ra^{2+}$			1.000017979(102)	4089(42)	552(46)	
			$ME_{AME2016}$ [keV]	ΔME [keV]	$E_{ex,lit}$ [keV]	ΔE_{ex} [keV]
			3540(50)	-2(15)	554(15)	2(42)

a. Adopted value

α-branching ratio of ^{207m}Ra

The α-branching ratio of ^{207m}Ra is estimated from the data obtained using the α-TOF detector. According to the fitting result of the alpha singles spectrum (Fig. 3.6), the total number of α-decay events from ^{206}Ra and ^{207m}Ra was N_{all}= 305±21.4. According to the TOF-correlated α-decay

analysis gating on $^{206}Ra^{2+}$ we find that N_{206Ra} =162 of these events were from ^{206}Ra. Thus, the number of ^{207m}Ra in the singles α-spectrum was N_{207mRa}= N_{all}-N_{206Ra} = 143±24.89 counts. Using the α-detection efficiency ε_α and the 16(9)% probability for having detected an alpha decay but missed the corresponding TOF signal (the inverse of the TOF detection efficiency shown in Chapter 2), the corrected α-decay counts for ^{207m}Ra is found to be $N_{cor,207mRa}$=(143/0.49)×(1-0.16)=245 ±49.5. Next, the denominator of ^{207m}Ra is determined. The production ratio of ground to isomer is 0.6/0.4 from the fitting of TOF spectra shown in Fig. 3.9. The area count of ^{207m}Ra was 945 counts. The α-branching ratio of ^{207m}Ra is evaluated to be (245/945)×100 = 26(20)%. This value is in agreement with the value of 25% previously reported by Hessberger, et al. [109] from α-decay spectroscopy.

Confirmation of ^{207}Ra with 265 laps

The TOF spectrum focused on the expected time-of-flight of $^{207}Ra^{2+}$ having made 265 laps is shown in Fig. 3.12. The red event was correlated with E_α above 7.32 MeV and decay time below 180 ms. While these are low statistics, there is one event in this gate, and it is consistent with the number assumed from the production and alpha branching ratios. There are 317 TOF singles events, and the expected correlated events based on gate width and detection efficiency would be 2.6 events. When considering the Poisson distribution, the probability of getting less than one event when 2.6 events are expected is 27%, which is statistically reasonable. Unfortunately, however, a similar analysis to that of 266 laps data is not possible. Therefore, the data obtained from 265 laps were used primarily to confirm the identify of $^{207}Fr^{2+}$ and $^{207}Ra^{2+}$ based on their unchanging relative times-of-flight.

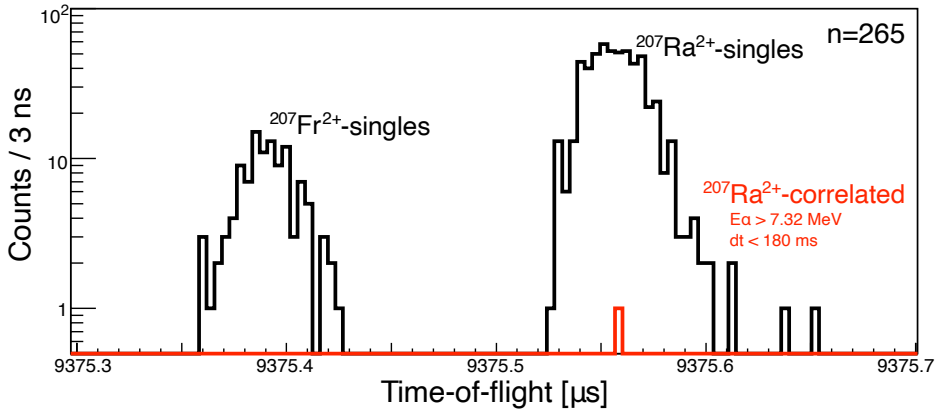

Figure 3.12: The time-of-flight spectrum centered on $^{207}Ra^{2+}$ having made 265 laps. The red histogram indicates decay tagged events with E_α above 7.32 MeV and decay time below 180 ms.

Influence of binning on mass analysis

We consider the error in the mass due to the bin width of the spectrum. Figure 3.13 shows the mass excess of ^{207g}Ra and excitation energy of ^{207m}Ra when the bin width is varied. These errors are fitting errors and are mostly contributed by statistical errors since we are using the isobaric reference. When the bin size is changed, there is a slight change in the mass, but the value is smaller than the standard deviation based on the statistical accuracy obtained in this experiment, and any effect of the bin size on the results can be ignored.

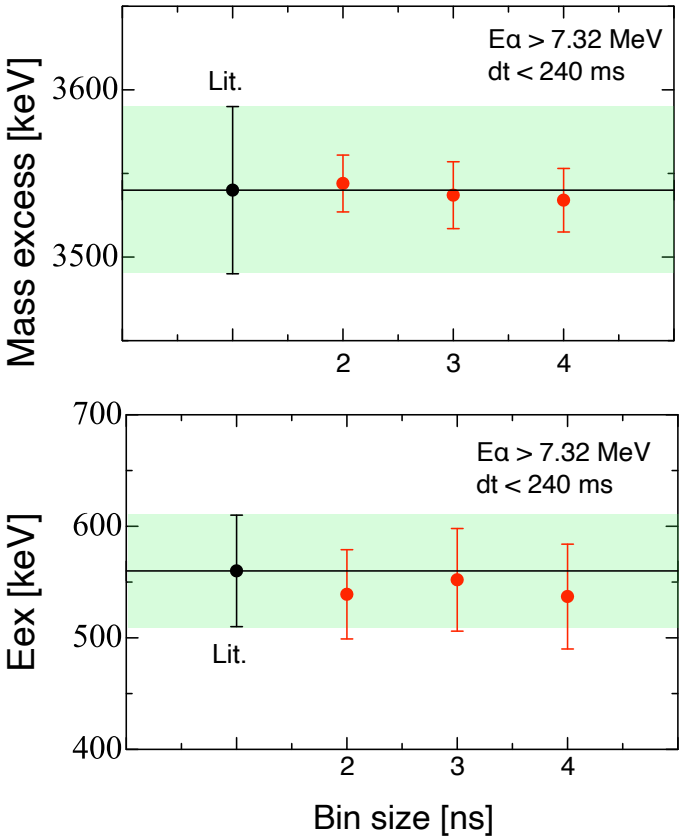

Figure 3.13: Mass excess of ^{207g}Ra and the excitation energy of ^{207m}Ra with different bin size. Regardless of the bin size, the values are within the range of statistical fluctuations.

3.4 Discussion

The spin-parity of ^{207m}Ra is tentatively assigned to J^{π}=13/2^{+}, based on the systematics of the neighboring nuclei. The single particle level diagram for odd Ra and Rn nuclei are shown in Fig. 3.14.

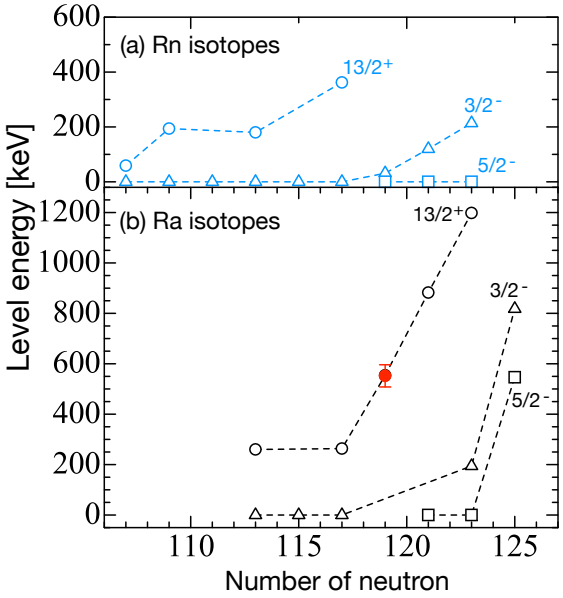

Figure 3.14: The single particle level diagram for odd Ra and Rn nuclides. Red circle indicate the measurement data for this experiments.

The solid red circle in Fig. 3.14 is the excitation energy of ^{207m}Ra obtained from our decay correlated mass analysis. It is agrees with the prior study from alpha-decay spectroscopy. The systematics continue to suggest that it is J^{π}=13/2^{+} as before. The spin-parity of ^{207g}Ra is assigned to either J^{π}=3/2^{-} or 5/2^{-} based on systematics, If J_{π}=3/2^{-}, then configuration =$((\pi h_{9/2})^{+6}_{0+}(\nu p_{3/2})^{-1})$ and if J_{π}=5/2^{-} configuration=$((\pi h_{9/2})^{+6}_{0+}(\nu f_{5/2})^{-1})$ [111]. However, the spin of ^{207g}Ra cannot be determined from this experiment.

The reduced alpha width δ^2 of ^{207m}Ra is evaluated to be 50^{+62}_{-41} keV according to the Rasmussen method. The decay energy and half-life were taken from the literature value [108]. Table 3.4 describes the reduced alpha width of 13/2^{+} and 3/2^{-} states in the neighboring nuclei ^{203}Ra and ^{205}Ra. Prior to our study, the reduced alpha width of ^{203}Ra and ^{205}Ra were reported to be around 60 keV for both states [111, 113]. The ^{207m}Ra is suggested to be 13/2^{+} not only in terms of single particle level systematics, but also from the reduced alpha width systematics. The reduced width is consistent with that of the neighboring nuclides, indicating that the α-decay of ^{207m}Ra is not forbidden. If the reduced alpha width is calculated using only the decay properties obtained using the α-TOF, it would be 43^{+158}_{-39} keV. Although the error is large, the spin assignments are same in both case.

This experiment shows that the correlation measurements of mass decay properties by MRTOF+α-TOF prove that not only the unique determination of the excitation energy of an isomeric state, but also its branching

ratio and partial half-life can be derived simultaneously. The results are in agreement with the historical α-spectroscopy measurements, and successfully demonstrate MRTOF+α-TOF spectroscopy.

Table 3.4: Summary of the spin-parity, decay properties and reduced alpha width (δ^2) of odd $^{203-207}$Ra isotopes. b_α is the branching ratio of α-decay.

Isotope	J^π	E_α [keV]	$T_{1/2}$ [ms]	b_α	δ^2 [keV]	Ref.
^{203g}Ra	$3/2^-$	7575(10)	50^{+40}_{-15}	1.0	45^{+37}_{-14}	[113]
^{203m}Ra	$13/2^+$	7607(8)	37^{+37}_{-12}	1.0	48^{+48}_{-16}	[113]
^{205g}Ra	$3/2^-$	7340(20)	210^{+60}_{-40}	1.0	50^{+24}_{-17}	[111]
^{205m}Ra	$13/2^+$	7370(20)	170^{+60}_{-40}	1.0	48^{+27}_{-18}	[111]
^{207g}Ra	$3/2^-$	7131(5)	1380^{+220}_{-110}	0.86	37^{+5}_{-6}	[111]
^{207m}Ra	$13/2^+$	7320(20)	59(4)	0.26(20)	50^{+62}_{-41}	this work
^{207m}Ra	$13/2^+$	7346(92)	55(9)	0.26(20)	43^{+158}_{-39}	this work[a]

a. All decay properties were obtained using the α-TOF.

Chapter 4

Mass measurement of ^{257}Db

Following the ^{206,207}Ra mass measurements, first direct mass measurement of the superheavy element ^{257}Db was performed.

4.1 History of the element $Z = 105$

In 1967 element Z=105 was discovered at about the same time in two laboratories – the Joint Institute for Nuclear Research (JINR) in USSR and Lawrence Berkeley National Laboratory (LBNL) in USA. The JINR group produced ^{261}105 and ^{260}105 by the 4, 5n reaction of ^{22}Ne+^{243}Am. The LBNL group identified ^{260}105 as the 4n evaporation channel of the ^{15}N+^{249}Cf [114] reaction. However, their results were inconsistent with the decay properties which JINR had reported. The JINR group followed up with a chemical experiment on element-105. Gas chromatography revealed that the chlorides of the fusion-evaporation product roughly matched the properties of $NbCl_5$ rather than $HfCl_4$, i.e. they were group 5 elements, further indicating that they were element-105. Both laboratories came forward with the naming of element-105, but they were unable to settle on any mutually agreeable name; the name Dubnium was adopted by IUPAC in 1994, with both laboratories sharing the credit for the discovery .

4.1.1 Previous study of ^{257}Db

The isotope ^{257}Db was first discovered at GSI in 1985, produced in the ^{50}Ti+^{209}Bi reaction [115]. Subsequently, α- and α-γ- nuclear spectroscopy studies were performed at GSI [101, 116] and GANIL [117]. Currently, the decay scheme of ^{257}Db is proposed to be as shown in Fig. 4.1.

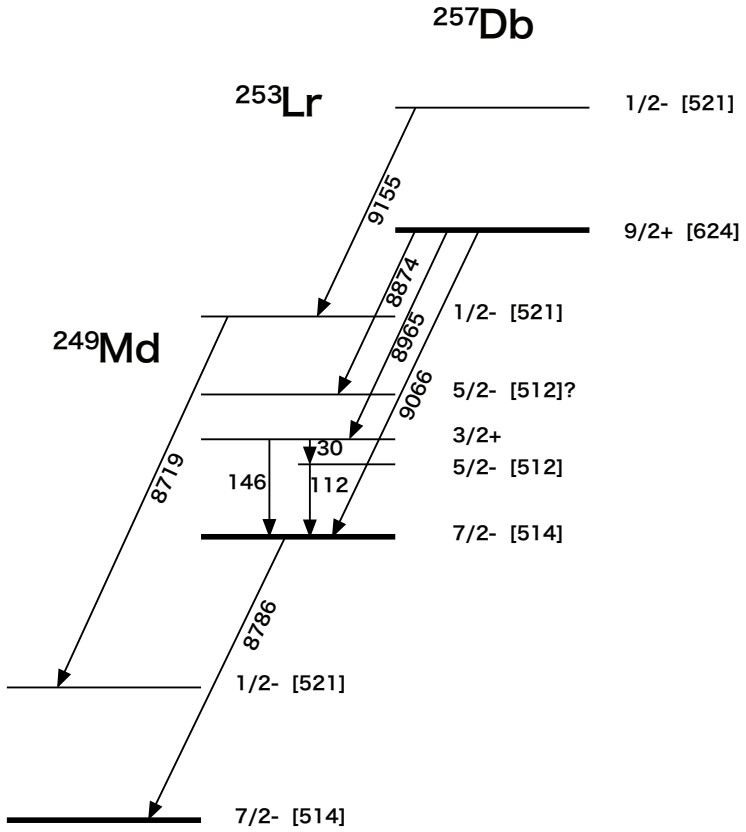

Figure 4.1: Currently proposed ^{257}Db decay scheme.

Despite several nuclear spectroscopic studies having been performed, the decay properties of ^{257}Db remain uncertain. It has been reported that three α-decay energies – 8.965 MeV, 9.066 MeV, and 9.155 MeV –are dominant. Through a series of studies, the decay properties of the ^{257}Db decay chain – decay energy, decay modes, half-lives and branching ratios – came to be understood to be as summarized in Fig. 4.2. The intensity of the known α-decay channels of ^{257}Db and ^{253}Lr are tabulated in Table 4.1.

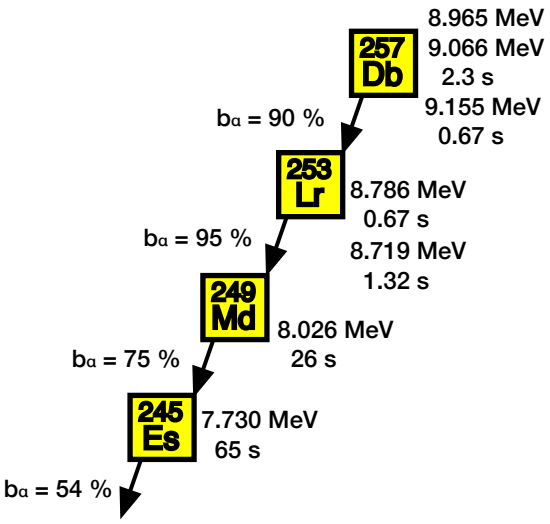

Figure 4.2: Properties of the ^{257}Db decay chain.

Table 4.1: Alpha decay energies, half-lives, and relative intensities for ^{257}Db and ^{253}Lr. This data taken from [101, 118].

Isotope	E_α [MeV]	$T_{1/2}$ [s]	Intensity [%]
^{257}Db	8.874(20)	$3.43^{+2.34}_{-0.99}$	4
	8.965(20)	2.32(16)	40
	9.066(20)	2.32(16)	37
	9.155(20)	0.67(6)	19
^{253}Lr	8.62	$1.09^{+0.86}_{-0.33}$	5
	8.719(15)	1.32(14)	28
	8.786(15)	0.67(6)	67

The masses of superheavy elements have never been measured directly before, and ^{257}Db is no exception. Recently, ^{249}Md, the granddaughter of ^{257}Db was measured directly by our group [80], and the mass excess of ^{257}Db was determined indirectly to be 100 234(224) keV/c^2, using known Q_α values and the presumed level schemes of the relevant nuclides.

4.2 Experiments

4.2.1 Setup

The setup used was the same as in the ^{206,207}Ra experiment described above (Fig. 2.31). A $^{51}V^{13+}$ beam was pre-accelerated by RIKEN RILAC-II and further accelerated to 6 MeV per nucleon by the RRC before being transported to GARIS-II. Targets of 99.6% enriched ^{208}Pb, having an average thickness are 360 μg/cm^2 vacuum deposited onto a 30 μg/cm^2 carbon backing were used. The targets were mounted on a 16-sector, double-layered, rotating target wheel along with 12 μm aluminum beam degraders; during beam irradiation the wheel rotated at 2000 rpm. During the experiment, the maximum beam intensity was 0.5 pμA. The incident energy at the target center was E_{lab} = 243 MeV. The strength of the D1 magnetic field was set to 14.2 kG, corresponding to a magnetic rigidity of 2.04 Tm.

4.2.2 Degrader optimization for ^{257}Db

The stopping power of a charged particle in the material is derived from Bethe-Bloch formula, which is proportional to the atomic number and inversely proportional to the mass number and the square of the velocity (energy) of the charged particle, as shown in Eqs. (4.1) and (4.2). For a particle with speed v, charge z, and energy E, traveling a distance x into a target material of electron number density n and mean excitation potential I, the rate of energy loss can be written

$$-\frac{dE}{dx} = \frac{4\pi n z^2}{m_e v^2}\Big(\frac{e^2}{4\pi\varepsilon}\Big)^2\Big[\ln(\frac{2m_e v^2}{I})\Big] \quad (4.1)$$
$$\Big(n = \frac{N_A Z \rho}{A M_u}\Big),$$
$$-\frac{dE}{dx} \propto \frac{Z}{A}\frac{1}{v^2}, \quad (4.2)$$

where ρ, A, and Z are the density, atomic mass number, and atomic number, respectively, of the target material, N_A is Avogadro's number, and M_u the Molar mass constant.

The SRIM/TRIM calculation commonly used to calculate such energy losses, has only been implemented for projectile particles up to uranium. Thus the energy loss experienced by nuclei above uranium must be determined by extrapolation from scaling of the atomic and mass numbers. In previous experiments on the chemistry of superheavy elements conducted at Dubna, the stopping power of heavy particles stopping in Ar gas and passing through Mylar films has been measured. By extrapolating the stopping power of the superheavy nuclei from the comparison of SRIM calculations

with experimental data, they have successfully measured the chemical properties of the Fl isotope produced in the ^{244}Pu(^{48}Ca, $3n$) reaction [119]. We assumed the kinetic energy of U, which is equivalent to the kinetic energy of Db, scaled by the mass and the atomic number of Db (Z=105, A=257), as in Eq. (4.3), and simulated using modified $E_{\mathrm{U}}(mod)$,

$$E_{\mathrm{U}}\frac{A_{\mathrm{U}}}{Z_{\mathrm{U}}} = E_{\mathrm{Db}}\frac{A_{\mathrm{Db}}}{Z_{\mathrm{Db}}},$$
$$E_{\mathrm{Db}} = E_{\mathrm{U}}\left(\frac{A_{\mathrm{U}}}{Z_{\mathrm{U}}}\right)\left(\frac{Z_{\mathrm{Db}}}{A_{\mathrm{Db}}}\right). \tag{4.3}$$

Figure 4.3 shows the results of the TRIM calculations. Red circles indicate the results of the calculation with ^{257}Db as $E_{\mathrm{U}}(mod)$ and blue circles indicate with ^{238}U. In both calculations, the maximum value is obtained with a total Mylar thickness of about 8 μm. In the ^{206,207}Ra experiment, the TRIM-calculated value and experimental result were in agreement with each other, therefore we trusted the calculated results and set the degrader thickness to 8 μm.

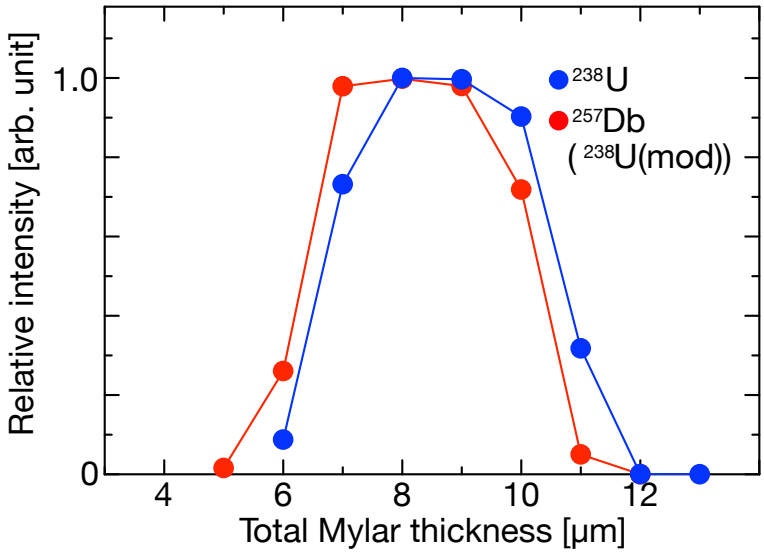

Figure 4.3: Result of TRIM calculation for Mylar degrader thickness. The blue circle is the result of calculation for ^{238}U, and the red circle is the result of scaling from ^{238}U such that the kinetic energy is equivalent to ^{257}Db.

4.2.3 Yield estimation

Prior to our study, the LBNL group reported a maximum fusion cross section of ^{257}Db in the ^{51}V+^{208}Pb reaction to be 1.6 nb [120]. The excitation

function is shown in Fig. 4.4. Note that the horizontal axis is the beam energy, not the mid-target energy.

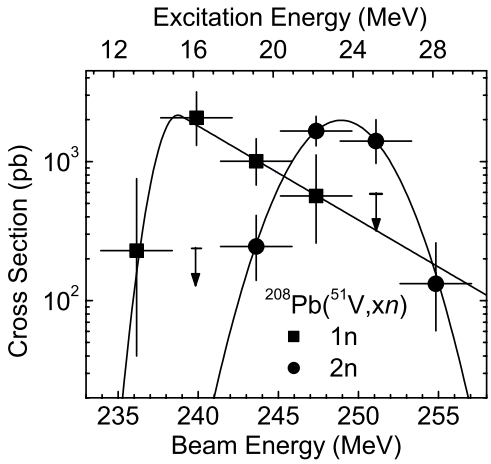

Figure 4.4: Excitation function of ^{208}Pb(^{51}V, xn) reaction system. This figure taken from [120].

Prior to our experiment, the synthesis of ^{257}Db by the ^{51}V+^{208}Pb reaction was carried out in the GARIS-II setup using RRC at RIKEN. The beam from RRC has a sizable energy spread and due to the vagaries of cyclotron operations can only deliver beam a specific energies, necessitating the use of aluminum energy degraders – further increasing the energy spread – to achieve the desired energy at target center. Despite the large energy spread, with a beam intensity of 0.4 pμA about 5.6 ^{257}Db events per hour were observed at the focal plane detector using the same experimental condition as the mass measurement. This rate corresponds to about 140 events per day. Assuming an efficiency of 4% for delivery to the MRTOF, we could expect 5.6 TOF singles events per day and 2.8 decay correlated events per day using α-TOF detector. These values are summarized in Table 4.2.

Table 4.2: Yield estimation of ^{257}Db based on the prior experiment at GARIS-II.

	$Y_{\mathrm{GARIS-II}}$ [cpd]	Y_{MRTOF} [cpd]	$Y_{\alpha-\mathrm{TOF}}$ [cpd]
^{257}Db	140	5.6	2.8

4.2.4 The charge state of ^{257}Db ion

Based on our previous experience [73, 80, 112], the system was initially configured to measure $^{257}Db^{2+}$ with $^{133}Cs^{+}$ reference ions. However, after a beam irradiation period of ≈36 hours, with a total beam dose on target of 4.7×10^{17} particles, no correlated event candidates were observed. In the NIST Atomic Spectra Database [75], the 3^{rd} ionization potential of dubnium is listed as 23.6±1.6 eV compared to the 24.6 eV first ionization potential of helium, which means that dubnium ions could possibly be extracted as triply-charged ions. Therefore, the system was reconfigured to measure $^{257}Db^{3+}$ using $^{85}Rb^{+}$ as the reference ion. In such a setting, TOF-α correlated events from $^{257}Db^{3+}$ were observed within 24 hours, and we continued the measurement with the system configured for $^{257}Db^{3+}$. The data were taken with a $^{257}Db^{3+}$ undergoing a variety of lap numbers of MRTOF: 300, 325, 324, 327, and 331 laps. A total dose of 1.1×10^{18} particles were irradiated on the target in 4.5 days beam time.

4.3 Results

The singles time-of-flight spectra for all runs are shown in Fig. 4.5. The green highlighted area shows the expected position of $^{257}Db^{3+}$. The intense peaks are attributed to molecular ions produced in the cryogenic gas cell, and the transfer products of ^{208}Pb target. Figure 4.6 shows the singles alpha spectrum measured by α-TOF detector. This spectrum is the sum of 4.5 days of accumulation. The relatively high intensity spectra observed around 7.5 MeV were attributed to the transfer product ^{211}Po (E_α=7.45 MeV). Energies from 7.8 MeV to around 9.5 MeV correspond to the decays of ^{257}Db and its decay chain: ^{253}Lr, ^{249}Md and ^{245}Es along with the transfer products ^{212}Po, ^{213}Po. In addition, three events were observed around 11 MeV, which are consistent with the decay energy of ^{212m}Po. The decay schemes of these transfer products are shown in Fig. 4.7.

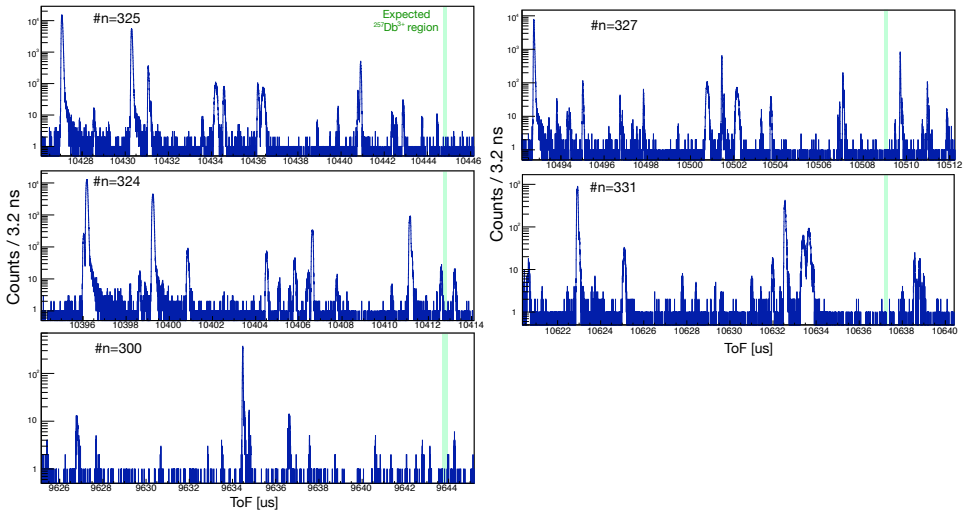

Figure 4.5: Singles time-of-flight spectra for all measured lap numbers. The green highlighted region indicates the area where $^{257}Db^{3+}$ is expected to be observed.

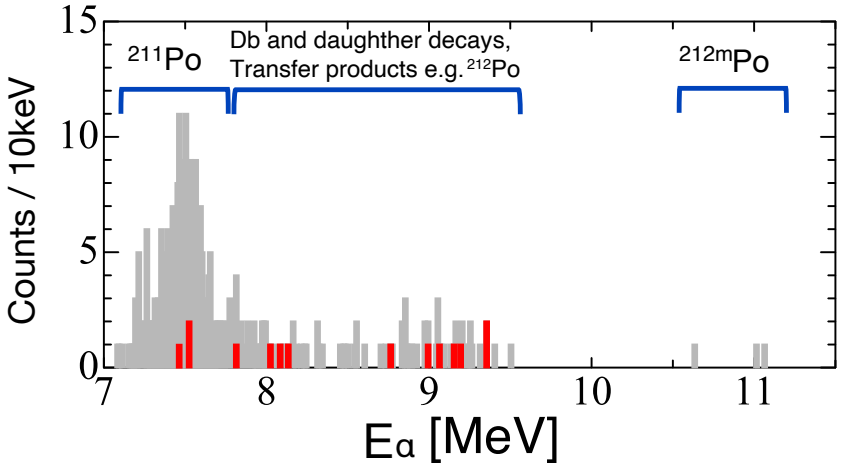

Figure 4.6: The singles α-decay spectrum is shown in grey. Events in red are those correlated with the time-of-flight signal (see text). The peak of ^{211}Po, a transfer product from the ^{208}Pb target, can be seen around 7.5 MeV. The decay signal of ^{212m}Po is also seen near 11 MeV.

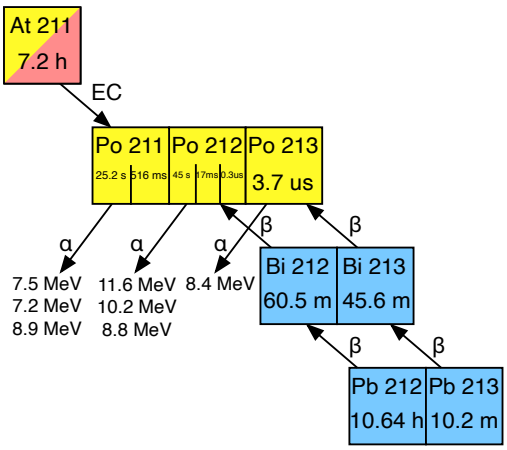

Figure 4.7: Decay scheme of the candidates of the transfer products. A part of the α-decay from 7.5 MeV to 9 MeV is presumed to be contributed by the Po isotopes shown in figure. These are surmised to originate from β/EC decays from Bi, and Pb, At isotopes.

In total, 14 correlated TOF-decay event candidates were observed during 105 hours of measurement. Figure 4.8 plots each decay correlated event in terms of detected α-decay energy and time between implantation and subsequent α-decay; events are named based on chronological order of observation. The right panel of Fig. 4.8 shows the anticipated decay time probability distribution [97] for each nuclide; multiple curves are shown for ^{257}Db and ^{253}Lr to represent known isomers. The upper panel shows the expected energy distribution for each alpha decay which could be observed in the ^{257}Db decay chain, with the α-decay singles spectrum superimposed. The correlated events appear to fall into two clusters corresponding to ^{257}Db or ^{253}Lr (E1, E5, E6, E9, E12, E13, E14) and ^{249}Md or ^{245}Es (E2, E3, E4, E7, E8, E10, E11). Table 4.3 tabulates the decay energies and decay times of the 14 TOF-decay correlated events.

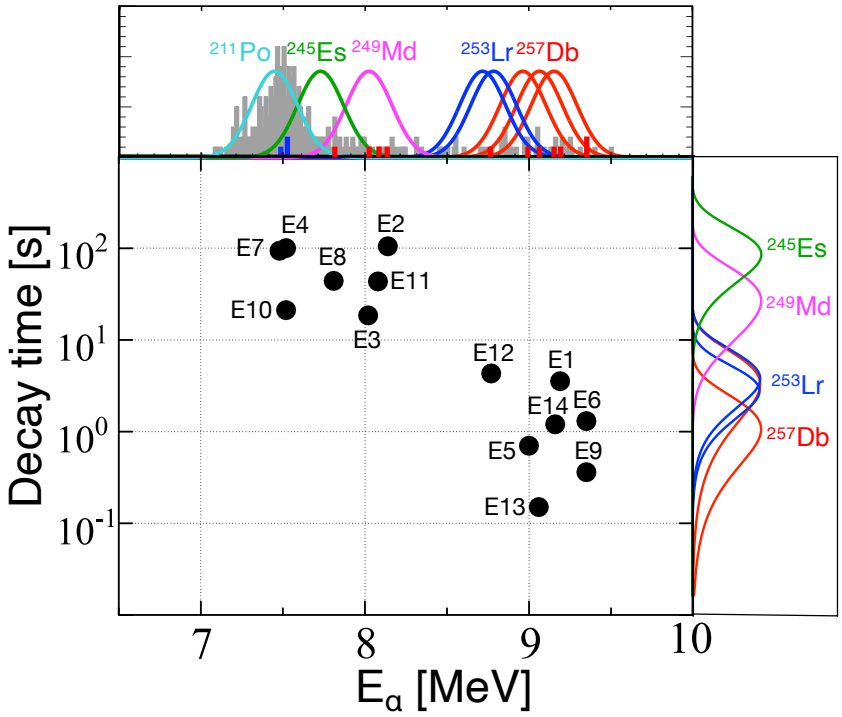

Figure 4.8: Two dimensional distribution of TOF-correlated α-decay events in terms of decay energy and decay time.

Table 4.3: Observed decay energies and decay times of the 14 correlated TOF-decay events.

Event	Laps	E_α [MeV]	Decay time [s]
E1	300	9.19	3.54
E2	300	8.14	105
E3	300	8.02	18.5
E4	325	7.52	100.2
E5	325	9.00	0.7
E6	325	9.35	1.3
E7	325	7.48	93.9
E8	324	7.81	44
E9	324	9.35	0.36
E10	324	7.52	21.1
E11	327	8.08	43.4
E12	327	8.77	4.3
E13	331	9.06	0.15
E14	331	9.16	1.2

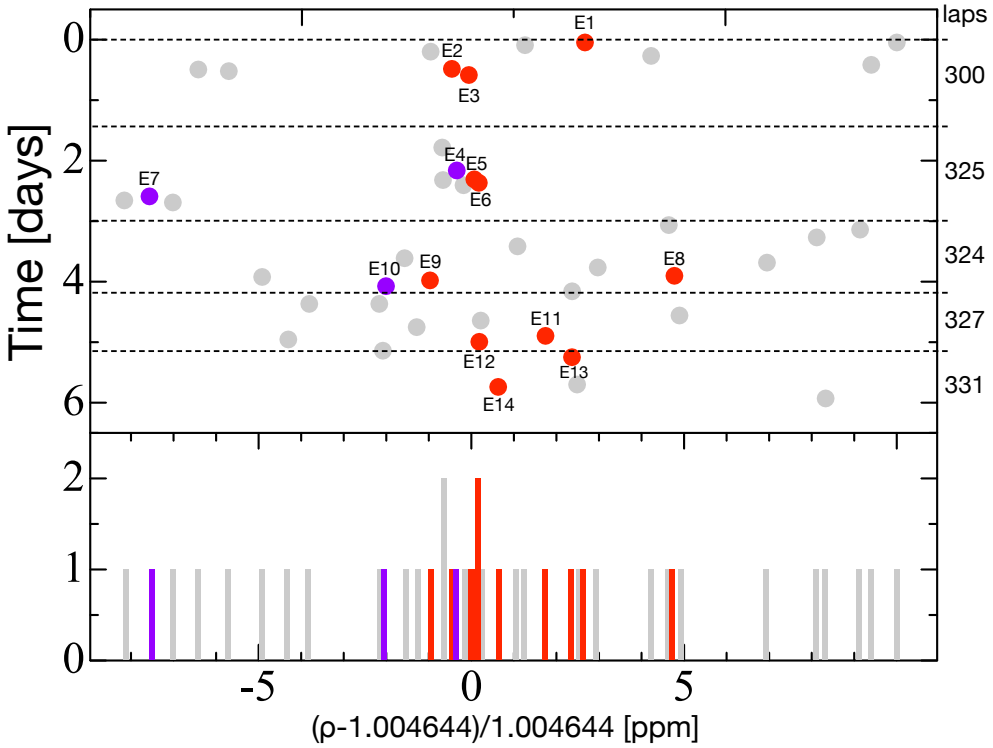

Figure 4.9: The time-of-flight spectrum and the time evolution of events near the $^{257}Db^{3+}$. In order to normalize the flight time for different lap number, we plot the time-of-flight ratio to the reference ion $^{85}Rb^{+}$. The absolute time-of-flight is about 10 ms and the domain of the plot, ± 10 ppm, is about 200 ns. The red color indicates the decay correlated events with the ^{257}Db decay chain, and the purple color indicate the accidental correlated events with the transfer products (see text).

The time-of-flight spectrum in the vicinity of $^{257}Db^{3+}$ is shown in Fig. 4.9. The upper part of figure shows the time of arrival of the events, in chronological order of observation. The times-of-flight are plotted in terms of the TOF ratio ρ, which is the ratio to $^{85}Rb^{+}$ used for reference to normalize the values at different lap numbers. These reference TOF were determined by the slice-by-event analysis method (Fig. 1.27(b)) in order to compensate for the TOF drift in long-term measurements. The reference signal of $^{85}Rb^{+}$ accumulated for 7.5 s before and after each decay correlated event was fitted by the Eq. (3.2). As examples, the reference TOF spectrum of E1 and E12 are shown in Fig. 4.10.

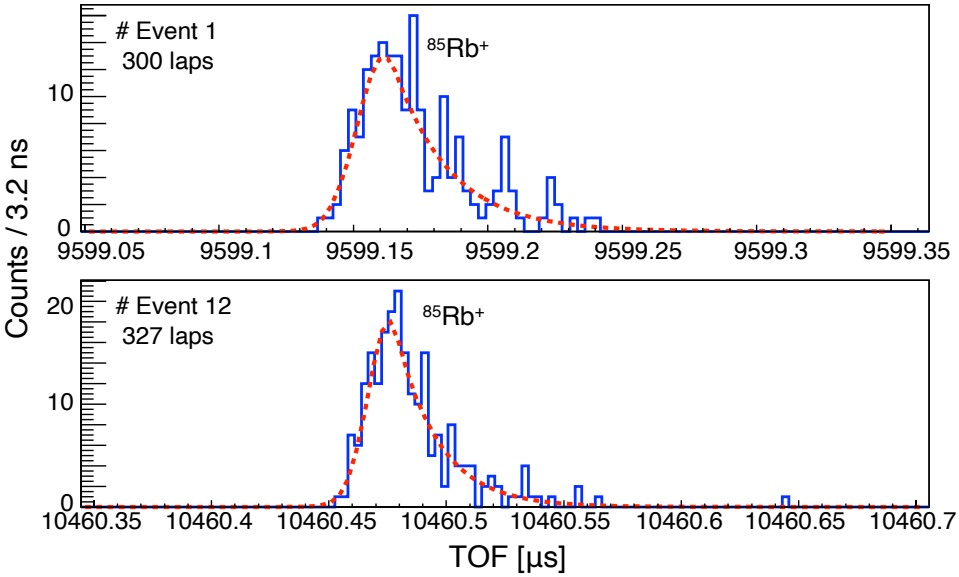

Figure 4.10: The reference spectrum of E1 and E12. Each reference signal was acquired 7.5 seconds before and after the event.

4.3.1 Coincidental probability

In this experiment, the coincidence time (T_c) for TOF-α-decay correlations was set to 120 s, which covers the decay time of the granddaughter ^{245}Es. Using this T_c, the total number of alpha-decay singles events in the analyte energy region (N_{alpha}) and the total measurement time (T_{total}), we estimated the random correlation probability P_{random}, defined by Eq. (4.4),

$$P_{random} = \frac{N_{alpha} \times T_c}{T_{total}} \times 100 \quad [\%]. \tag{4.4}$$

The random correlation probability in the energy region of ^{211}Po was thereby estimated to be 7.3%. This estimation is based on the 120 s coincidence time and 235 observed α-decay counts in ^{211}Po energy region. There were 27 TOF singles events observed in the time-of-flight spectra in a 60 ns wide region centered on the expected TOF for $^{257}Db^{3+}$ – the range corresponds to the full width at tenth maximum (FWTM) of the spectral peak based on the peak shape of the $^{85}Rb^{+}$ reference ion. Therefore, we expect to observe ≈2 accidental correlations with ^{211}Po. Similarly, the accidental correlation probabilities for islands in the ^{257}Db, ^{253}Lr energy region and islands in the ^{249}Md, ^{245}Es energy region are shown in Table 4.4.

Table 4.4: Number of singles α-signal N_{alpha} and accidental coincidence probability P_{random} in each α-decay energy region.

Energy region	N_{alpha}	P_{random} [%]
^{257}Db-^{253}Lr	51	1.6
^{249}Md-^{245}Es	41	1.3
^{211}Po	235	7.3

4.3.2 Accuracy of each event

Probability density function $f(x)$ for standard normal distribution $N(0,1)$ is expressed by

$$f(x) = \frac{1}{\sqrt{2\pi}} \exp\left(\frac{x^2}{2}\right). \tag{4.5}$$

The area $g(x)$ of a random variable x when integrated from 0 to z is calculate by

$$g(x) = \int_0^z \frac{1}{\sqrt{2\pi}} \exp\left(\frac{x^2}{2}\right) dx. \tag{4.6}$$

For example, the area corresponding to a standard deviation of 1σ corresponds to 68.3% of the total area. Where the confidence level is written as $1 - g(x)$. In other words, when the acquired data point is 1σ away from the central value, its confidence level $P(0:1)$ is $P = 1 - 0.683 = 0.317$.

When there are N systems in parallel, each of which has a confidence level of X_i, the confidence level of the system as a whole, Φ, can be written as follows

$$\Phi = 1 - \Pi_{i=1}^{n}(1 - X_i). \tag{4.7}$$

This evaluation is often used to evaluate the reliability of an entire system, such as a parallel circuit consisting of multiple systems [121]. The α-decay energy and decay time of one event obtained are compared to an arbitrary state of the nucleus of interest to evaluate the accuracy of the event. When the confidence level of the decay energy is set to P_{ene} and the confidence level of the decay time is set to P_{dt}, the accuracy of the acquired single event is evaluated as $X_{\mathrm{state}} = 1 - (1 - P_{\mathrm{ene}})(1 - P_{\mathrm{dt}})$ from the convolution by these parallel systems. The reliability block diagram (RBD) based on this concept is shown in Fig. 4.11 (b).

The nucleus to be compared is one of several excited states, but in a system like Db, where the states are unknown and complex, it is difficult to

distinguish individual states even from our mass resolving power and energy resolution. Thus, we assume that each state exists in parallel, as shown in Fig. 4.11(a), the certainty of the acquired event Φ_X can be expressed as a convolution of the accuracy of each state $X_{\rm state}$,

$$\Phi_X = 1 - \Pi^n_{\rm state=1}(1 - X_{\rm state}). \tag{4.8}$$

In the case of ^{257}Db, three decay modes are intermingled, as shown in Fig. 4.2, but this calculation allows us to evaluate the Db like of the event itself, taking all states into account. Likewise, ^{253}Lr case can estimate the accuracy from the convolution of the two states.

Table 4.5 tabulates the certainty Φ_X of each of the 14 decay correlated events. This was derived from the confidence level of the energy and decay time compared to the decay chain of ^{257}Db and the multinucleon transfer product ^{211}Po. The accuracy and confidence level of each state is tabulated in Appendix A. Based on the reported decay properties, the states of ^{257}Db corresponding to decay energies of 9.155 MeV, 9.066 MeV, and 8.965 MeV are tentatively assigned to ^{257}Db(1), ^{257}Db(2), and ^{257}Db(3), respectively, and the states of ^{253}Lr corresponding to decay energies of 8.719 and 8.786 MeV are tentatively assigned to ^{253}Lr(1) and ^{253}Lr(2), respectively. In the calculation, events with energy or decay time confidence less than 2.5σ, i.e., less than P=0.01, are excluded from the calculation. The ^{211}Po is due to accidental coincidence, so only the reliability of the energy is taken into account.

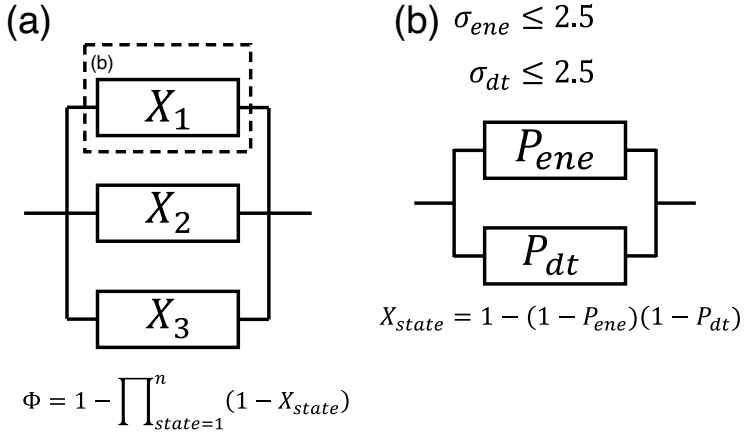

Figure 4.11: The reliability block diagram (RBD) of calculation for accuracy of each event. (a) RBD for each exited state. (b) The RBD for confidence level of observed energy and decay time.

Table 4.5: Summary of the reliability of each decay correlated event compared to the nuclides in the ^{257}Db chain.

	E_α [MeV]	dt [s]	$\Phi(^{257}\mathrm{Db})$	$\Phi(^{253}\mathrm{Lr})$	$\Phi(^{245}\mathrm{Md})$	$\Phi(^{245}\mathrm{Es})$	$\Phi(^{211}\mathrm{Po})$
E1	9.19	3.54	0.96	<0.01	<0.01	<0.01	<0.01
E2	8.14	105	<0.01	<0.01	0.56	<0.01	<0.01
E3	8.02	18.5	<0.01	<0.01	0.94	<0.01	<0.01
E4	7.52	100.2	<0.01	<0.01	<0.01	<0.01	0.38
E5	9.00	0.7	0.92	<0.01	<0.01	<0.01	<0.01
E6	9.35	1.3	0.92	<0.01	<0.01	<0.01	<0.01
E7	7.48	93.9	<0.01	<0.01	<0.01	<0.01	0.71
E8	7.81	44	<0.01	<0.01	<0.01	0.39	<0.01
E9	9.35	0.36	0.15	<0.01	<0.01	<0.01	<0.01
E10	7.52	21.1	<0.01	<0.01	<0.01	<0.01	0.38
E11	8.08	43.4	<0.01	<0.01	0.96	<0.01	<0.01
E12	8.77	4.3	0.92	0.99	<0.01	<0.01	<0.01
E13	9.06	0.15	0.82	<0.01	<0.01	<0.01	<0.01
E14	9.16	1.2	0.99	<0.01	<0.01	<0.01	<0.01

4.3.3 Event assignments

Based on the accuracy Φ_X shown in Table 4.5, the nuclide identification was performed for each of the decay correlated events. For the energy uncertainties, the resolution of the α-TOF detector was used.

Events 1, 5, 6, 9, 13, 14

For events 1, 5, 6, 9, 13, and 14 we measured alpha energies and decay times that are consistent with ^{257}Db. Event 1 has the same degree of confidence for both ^{257}Db(1) and ^{257}Db(2) states. Events 5, 14 have equal degrees of confidence for all states. Events 6, 9, 13 are consistent only with ^{257}Db(1), tentatively assigned as the J^π=1/2$^-$ isomeric state, from confidence calculations. The relative intensity of ^{257}Db(1) is reported to be 19%, the expected event to credit this intensity is 1.14 out of 6 events. Given a Poisson distribution with an expected value of 1.14 events, the probability that the observed event is more than 3 is 11%. However, since isomeric state cannot be separated based on the mass resolving power and energy resolution obtained in this experiment, the contribution of these states is included in the mass determination as a systematics error. In this case, we assume that the measured event was split almost evenly between the two states, and we account for this by adding a systematic uncertainty of 70 keV/c^2. Based

on the above reasoning, we determined that these 6 events were correlated with the decay of ^{257}Db.

Events 12

Event 12 agrees with the decay properties of ^{257}Db(3) and ^{253}Lr(1) and ^{253}Lr(2) with similar degrees of confidence. The confidence level was slightly higher for ^{253}Lr than for ^{257}Db, thus event 12 was identified as ^{253}Lr.

Events 2, 3, 11

The decay properties of events 2, 3, 11 are in good agreement with those of ^{249}Md, and the confidence levels of other nuclides are all below 0.01. Thus, we can clearly say that these three events are correlated with ^{249}Md decay.

Events 8

The decay property of event 8 is consistent with the decay properties of ^{245}Es, and is far from the decay energy of ^{211}Po, a multinucleon transfer reaction product. On the other hand, the detection probability for ^{245}Es is only 1.4%, as described below, and the expected number to be observed from 14 total events is 0.3. When the expected value is 0.3, the probability of observing one event is 22%, which is not a small enough probability to reject. Also, if we assume that this is the decay of ^{249}Md, the decay time is consistent, but the decay energy is 2.6σ away from the literature value. Regardless of the nuclide identification it is still an event correlated with the decay chain of ^{257}Db, but we decided to trust the confidence level and assume it was a correlation event with ^{245}Es.

Events 4, 7, 10

The decay energies of events 4, 7, and 10 are in good agreement with the transfer product ^{211}Po. The decay times for all events are close to those of ^{245}Es, but the energies are more than 2.5σ away. As discussed in Section 4.3.1, the number of accidental coincidences in this energy region is estimated to be about 2, which is consistent with the observed number. Based on these evaluations, we determine that these three events are accidental coincidence with ^{211}Po and exclude them from the mass analysis.

4.3.4 Consideration of the number of correlated events

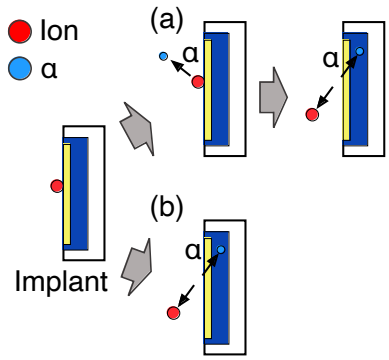

Figure 4.12: Conceptual view of alpha particle detection. (a) Alpha particle emission away from the Si detector. In this case, the implanted atom remains on the Si detector surface, and the next-generation decay might be observed. (b) Alpha particle emission into the Si detector. The implanted atom is removed from the detector surface by recoil energy of alpha decay and next-generation decay is precluded.

^{257}Db undergoes up to four α-decays, as shown in Fig. 4.2. The ions impact the α-TOF detector at an energy of 2 keV/q and are embedded at a depth of no more than a few angstroms. Therefore, the implanted atoms are ejected from the detector surface by decay recoil if the alpha particle is emitted toward the detector (E_{recoil} ~140 keV) as shown in Fig. 4.12 (b). Hence, it is not possible to observe successive α-particles along the decay chain. However, when α-particles are emitted away from the detector (Fig. 4.12 (a)), the daughter will generally not be removed from the detector surface, and the α-decay of the next generation can be detected. Since the detection efficiency per decay is 45% as evaluated in Chapter 2, the detection probability of ^{257}Db, $\epsilon_{\mathrm{det}}(^{257}\mathrm{Db})$, can be calculated from the detection efficiency and the alpha branching ratio (b_α) of ^{257}Db as shown in Eq. (4.9). The detection probability of ^{253}Lr and for its daughter can be further calculated from there, as shown in Eq. (4.10), from the detection efficiency and the α-branching ratio of ^{253}Lr,

$$\varepsilon(^{257}\mathrm{Db}) = \varepsilon_\alpha \times b_\alpha(^{257}\mathrm{Db}), \tag{4.9}$$

$$\varepsilon(^{253}\mathrm{Lr}) = \varepsilon(^{257}\mathrm{Db}) \times \varepsilon_\alpha \times \mathrm{b}_\alpha(^{253}\mathrm{Lr}). \tag{4.10}$$

In the same way, the detection probability can be evaluated up to ^{245}Es. Considering the branching ratio of the α-decay of each nuclide, the probability of detecting one of the α-decays in the ^{257}Db decay chain is 65%.

Including the number of α-decays that could not be detected, it is estimated that there should be $11/0.65 = 16.9$ time-of-flight signals for ^{257}Db in total. The branching ratios and α-decay detection probability for each nuclide, as well as the expected and experimentally observed number of events, are tabulated in Table 4.6. The observed number of events for all nuclides are in the 2-σ confidence interval of the expected number of observations.

Table 4.6: Table listing the alpha branching ratio b_α, detection efficiency ε_{det}, and expected counts for nuclides in the ^{257}Db decay chain, along with the observed number of events in the experiment.

	b_α	ε_{det}	N_{expect}	$N_{observed}$
^{257}Db	0.9	0.405	6.8±2.6	6
^{253}Lr	0.95	0.173	2.9±1.7	1
^{249}Md	0.75	0.058	1.0±1.0	3
^{245}Es	0.54	0.014	0.2±0.5	1

4.3.5 Number of background counts

A total of 27 single events for all runs were observed within ±30 ns of the anticipated flight time of ^{257}Db^{3+}, a range corresponding to the FWTM of ^{257}Db^{3+} spectral peak. Of these, 17 TOF singles events are attributable to ^{257}Db^{3+}, 11 of which were correlated to alpha-decay events. To examine the remaining 10 events, we consider the background rates for all runs. Sources of background would include dark current in the detector, cosmic rays, random β-rays from β-ray emitters produced in transfer reactions, or stable molecular ions making different numbers of laps.

In the TOF singles spectrum shown in Fig. 4.5, we counted the background in the region close to the A/q of ^{257}Db^{3+} to determine the total background per 60 ns. Intense peaks are excluded from this count to avoid overestimation. The evaluated background counts expected per 60 ns as evaluated for the data at each lap number are summarized in Table 4.7. With a total of 105 hours of measurements at five different lap numbers, there would be 11.6 expected number of background, on average, per 60 ns. This is consistent with the excess 10 events we observed.

Table 4.7: Background count per 60 ns for data at each lap number.

Number of laps	325	324	327	331	300	Sum
Background/60 ns	2.25	2.06	2.82	2.02	2.50	11.6

4.3.6 Mass analysis

Table 4.8 provides a tabulation of the TOF of the 11 α-decay correlated TOF events and the TOF of the respective reference ion $^{85}Rb^{+}$. In the time-of-flight spectrum in Fig. 4.9, the red plots are the events used in this mass analysis, and the three events shown in purple – the events coincidentally correlated with ^{211}Po alpha-decay – are excluded. The data for the α-decay correlated TOF events are tabulated in Table 4.10 along with the various characterizing qualities of each. The value ρ^2, defined as $\rho^2 = (\frac{t_{\text{analyte}}-t_0}{t_{\text{reference}}-t_0})^2$, represents the ratio of mass-to-charge ratios of $^{257}Db^{3+}$ and $^{85}Rb^{+}$. The inherent time offset t_0 was determined to be t_0 =75(4) ns from evaluations of $\rho(^{208}Pb^{2+}/^{85}Rb^{+})$ measured at the end of the experiment; the uncertainty of t_0 was determined from the values leading to an evaluated mass of of ^{208}Pb with deviation from AME2016 values within the error band of the measurement. The times-of-flight for $^{208}Pb^{2+}$ and $^{85}Rb^{+}$ used in the evaluation are shown in Table 4.9.

Table 4.8: The absolute time-of-flight of $^{257}Db^{3+}$ and $^{85}Rb^{+}$ ions for each decay correlated event.

Events	laps	TOF $^{257}Db^{3+}$ [ns]	TOF $^{85}Rb^{+}$ [ns]
E1	300	9 643 766.6	9 599 162.6(6)
E2	300	9 643 706.8	9 599 133.2(10)
E3	300	9 643 722.3	9 599 144.8(15)
E5	325	10 444 856.4	10 396 574.3(7)
E6	325	10 444 850.4	10 396 567.2(9)
E8	324	10 412 968.4	10 364 785.0(10)
E9	324	10 412 909.4	10 364 785.8(11)
E11	327	10 509 056.3	10 460 476.2(12)
E12	327	10 509 061.4	10 460 465.0(12)
E13	331	10 637 228.7	10 588 033.0(10)
E14	331	10 637 167.6	10 587 990.6(11)

Table 4.9: The times-of-flight for $^{208}Pb^{2+}$ and $^{85}Rb^{+}$ used for determination of the inherent offset time t_0. From these values t_0 was determined to be t_0=75(4) ns.

laps	TOF $^{208}Pb^{2+}$ [ns]	TOF $^{85}Rb^{+}$ [ns]
324	11 470 047.8(14)	10 364 705.8(1)

The times-of-flight t_{analyte} and $t_{\text{reference}}$ would typically be determined by fitting the analyte and reference ion's spectra such as was shown in the

$^{206/207}$Ra analysis. However, in this work, it was not possible to perform such fitting on the analyte ion's spectral peaks because the number of correlated events obtained for each lap number was only one or two. Therefore, we used the algebraic weighted average method to determine the A/q of $^{257}Db^{3+}$.

To ascertain the reliability of such an analysis technique, we used a data set comprising 3358 consecutive sets of 10 ions of $^{185}Au^{2+}$ accumulated during preparation for the $^{257}Db^{3+}$ measurements. For each set of 10 ions, the A/q was evaluated. A histogram of the deviation between evaluated A/q and the literature A/q value is shown in Fig. 4.13. To check the consistency of these statistical indeterminacy, the Birge ratio R [122] for each event was calculated. The Birge ratio is written as

$$R = \frac{\sigma_{out}}{\sigma_{in}}, \tag{4.11}$$

σ_{out} is the outer error, defined by the standard deviation of the measured data points

$$\sigma_{out} = \sqrt{\frac{\Sigma_i w_i (r_i - \overline{r})^2}{(N-1)\Sigma_i w_i}}, \tag{4.12}$$

where r_i is the square of the ratio of the analyte TOF to the reference TOF (ρ^2) for each point, w_i is the weight defined as $w_i = 1/\sigma_i$ where σ_i is related to the error of the ratio r_i, N is the number of data points, and $\overline{r}$ is the weighted average of r_i,

$$\overline{r} = \frac{\Sigma_i w_i r_i}{\Sigma_i w_i}. \tag{4.13}$$

The inner error σ_{in} is the weighted average error,

$$\sigma_{in} = \sqrt{\frac{1}{\Sigma_i w_i}}. \tag{4.14}$$

The Birge ratio R indicates whether the variance of the evaluated data adequately accounts for statistical uncertainty. A Birge ratio of 1 indicates that the evaluated data is consistent with statistical variability. If the Birge ratio is greater than one, it is likely that the error bars have been underestimated and the errors should be re-normalized by the Birge ratio. After multiplying the uncertainty of each of the 3358 A/q-values by their Birge ratio, we found that 51% were within 1σ of the AME16 value, 83% were within 2σ, and 95% were within 3σ (Fig. 4.13). This is acceptably close to the statistical expectations.

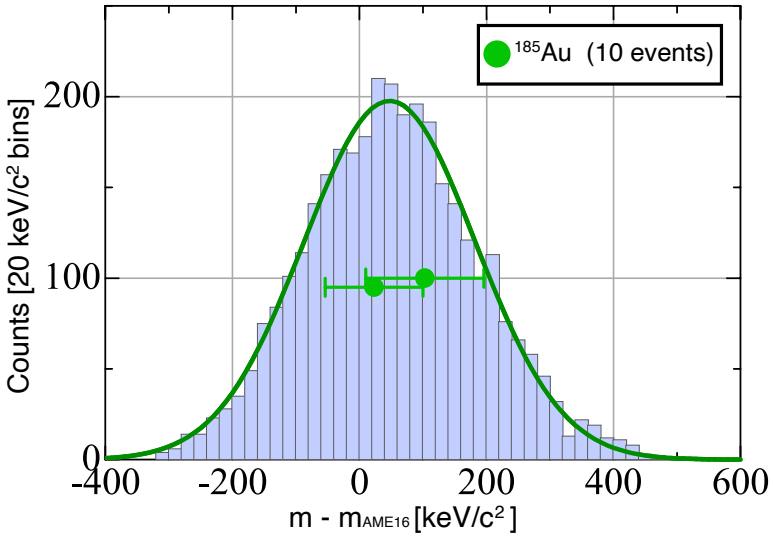

Figure 4.13: Distribution of ^{185}Au mass deviations evaluated from a set of 3358 measurements each comprising 10 events. The two green points with horizontal error bars are the results of two randomly selected 10-ion evaluations, showing that the masses derived by the weighted average of the 10 events are close to statistical expectations.

The lower part of Table 4.10 describes the ρ^2 obtained from the weighted average of 11 events, the Birge ratio and the ρ^2 that errors were renormalized by the Birge ratio. The renormalized weighted average ρ^2 of $^{257}Db^{3+}$ compared to $^{85}Rb^{+}$ was determined to be ρ^2=1.009 311 901(973)$_{stat}$(7)$_{sys}$. The systematic uncertainty derives from δt_0=4 ns. From this TOF ratio we derive a mass excess of 100 063(231)$_{stat}$(2)$_{sys}$ keV/c^2. The relative mass uncertainty is δm/m$\sim$9.7$\times$10^{-7}. The deviation from the indirectly determined value in our previous result is ΔME=171(231) keV [80].

Table 4.10: Summary of correlated TOF-α events. The laps column lists the number of times the $^{257}Db^{3+}$ reflects back-and-forth in the MRTOF-MS. The observed α-particle energy and the time between implantation and decay are listed in columns E_α and the decay time, respectively. The best estimate as to the nuclide which emitted the detected α-particle for the correlated event assignment is listed in the column labelled Nuclide. ME_{indirect} is the previously evaluated value from indirectly determined [80]. ΔME is the mass difference between our experimental data and literature values. See text for explanation of ρ^2.

Events	laps	E_α [MeV]	Decay time [s]	Nuclide	ρ^2
E1	300	9.19	3.54	^{257}Db	1.009314964(90)
E2	300	8.14	105.00	^{249}Md	1.009308647(157)
E3	300	8.02	18.50	^{249}Md	1.009309454(237)
E5	325	9.00	0.70	^{257}Db	1.009309712(91)
E6	325	9.35	1.30	^{257}Db	1.009309926(119)
E8	324	7.81	44.00	^{249}Md	1.009319206(155)
E9	324	9.35	0.36	^{257}Db	1.009307610(173)
E11	327	8.08	43.40	^{249}Md	1.009309949(156)
E12	327	8.77	4.30	^{253}Lr	1.009313092(150)
E13	331	9.06	0.15	^{257}Db	1.009314345(148)
E14	331	9.16	1.20	^{257}Db	1.009310844(144)
Weighted Average					1.009311901(40)
Birge ratio					24.4
Reweighted Average					1.009311901(973)
ME_{EXP} [keV/c^2]					100 063(231)(2)
ME_{Indirect} [keV/c^2]					100 234(224)
ΔME [keV/c^2]					171(231)

4.4 Discussion

4.4.1 Comparison with various mass models

The nuclide ^{257}Db is the alpha-decay daughter of ^{261}Bh. The mass excess of ^{261}Bh can be indirectly determined to be $ME_{261\text{Bh,ind}}$=112 988(236) keV/c^2 from the mass excess $ME_{257\text{Db}}$=100 063(231) keV/c^2 measured directly in this experiment and the reported Q_α=10 500(50) keV/c^2 [25]. A comparison between these mass excess and the global mass model: shell model DZ10 [123, 124], macroscopic-microscopic model FRDM12 [125] and WS4$^{\text{RBF}}$ [126], self-consistent mean-field models HFB32 [127], Weizsacker-Bethe WB03 [128], and phenomenological mass model KTUY05 [129], are shown in Fig. 4.14. The mass of ^{257}Db determined directly by this experiment and the indirectly determined mass of ^{261}Bh support the theoretical calculations for

macroscopic-microscopic mass model FRDM12 and WS4$^{\mathrm{RBF}}$. In particular, the WS4$^{\mathrm{RBF}}$ calculations have obtained the dispersion below 500 keV/c^2, which is in good agreement with both masses.

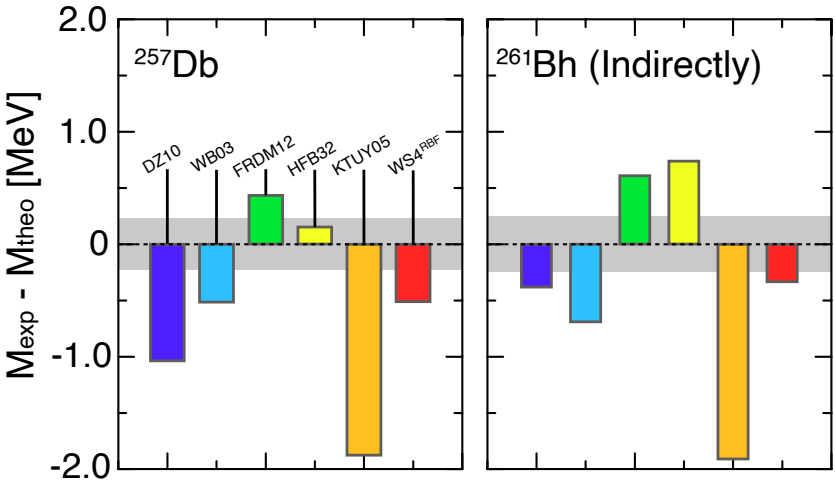

Figure 4.14: Comparison of the mass excess of ^{257}Db and ^{261}Bh with those calculated by various global mass models. Grey area indicates error bars in the experimental data, except for KTUY, where the discrepancies between calculated and experimental data are within 1 MeV/c^2. The experimental values support the macroscopic-microscopic calculation, FRDM12 and WS4.

4.4.2 Z determination from mass measurements

Let us consider the feasibility of identifying the synthesized superheavy nuclides (Z and A identification) by precision mass measurement. Figure 4.15 shows a plot of the mass excess of the A=257 isobars for atomic numbers Z= 94 to 106. The areas highlighted in blue are the range of predictions from a comprehensive selection of global mass models and the green highlights are the range of literature values listed in AME2016. We superimpose on that the mass excess measured for each of our TOF correlated α-decay events corresponding to ^{257}Db^{3+}

The nuclides having A=257 that can be produced by the ^{208}Pb(^{51}V, X) reaction system are restricted to ^{257}Db ($2n$ evaporation channel), ^{257}Rf ($1p1n$), and ^{253}Lr ($2p$). This range is designated by the red box in Fig. 4.15. Imposing such a condition, it is easy enough to make an unambiguous identification of the analyte ion as ^{257}Db. The mass excess of ^{257}Db is also consistent with the mass excess with ^{257}Am on the other side of the Heisenberg valley. However, were the reaction system able to populate such a nuclide, it could easily be distinguished from the decay properties by using

the α-TOF detector. This indicates that even rare superheavy nuclei, including those which may be produced by multinucleon transfer reactions, can be distinguished.

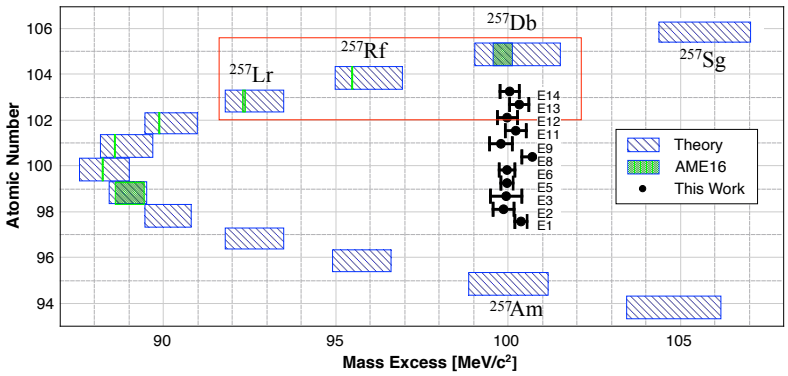

Figure 4.15: Mass excess determined for each alpha decay correlated TOF event in this work compared to mass excess ranges for A=257 isobars as determined by various global mass models (blue hash) along with values from AME16 (green hash). The red box designates nuclides whose production is possible in the ^{208}Pb(^{51}V, X) reaction system.

Chapter 5

Future prospective

5.1 Further mass measurements of superheavy nuclides

5.1.1 Plans for future measurements of Db and Sg isotopes

Following the success of the mass measurement of ^{257}Db, we are now planning to work on further mass measurement of the superheavy elements. Currently, the only fusion-amenable beam the RRC can supply to GARIS-II is a ^{51}V beam at 6 MeV per nucleon. One existing plan is for the production and mass measurement of other dubnium isotopes $^{256-258}$Db produced in the ^{51}V+^{208}Pb reaction system as well as to investigate Sg isotopes by the ^{51}V+^{209}Bi reaction system. The excitation function measured by J.M. Gates in Fig. 4.4 gives an estimated fusion-evaporation cross-section for ^{258}Db of 2 nb at a beam energy $E_{\mathrm{lab}} = 239.7$ MeV [120]. In experiments at RIKEN GARIS-II, the fusion-evaporation cross-section for ^{256}Db was estimated to be about 300 pb at 247 MeV mid-target energy [131], although this is an incomplete measurement.

The fusion-evaporation cross-sections for Sg isotopes from the ^{51}V+^{209}Bi reaction have not yet been reported. However, we can consider the systematics from other systems, such as the cross-section for ^{259}Sg from the $1n$ evaporation channel of the ^{52}Cr+^{208}Pb reaction system. In that reaction system the fusion-evaporation cross-section was reported to be 300 pb [130]. We can expect a similar fusion-evaporation cross-section in the ^{51}V+^{209}Bi reaction system despite the differences in the beam nuclei.

For the mass measurement of nuclei with even smaller fusion cross-sections, one possibility is to increase the yield through target improvement. In the experiment reported in Chapter 4 we used a target made from metallic Pb, which has a melting point of about 327.5°C. The low melting point limited the allowable average beam intensity to 0.4 pμA due to the thermal weakness of the target. By using sulfide targets such as PbS and BiS, hav-

ing melting points of 1,114°C and 775°C, respectively, we could use a beam intensity of more than 1.0 pμA. The transportation efficiency from the gas cell to the MRTOF system is currently 5%, but it is expected to be able to increase to about 10% with the optimization and improvement of the RF traps. Table 5.1 shows the yield estimation for the estimated fusion cross section and the improved transport efficiency and beam intensity. This estimate is only for production reactions using ^{51}V beam, If other beam species become available, the number of accessible superheavy nuclei will expand further.

Table 5.1: Yield estimation for SHE for which future study by α-TOF are planned. The yields are given in counts per day (cpd). The GARIS-II transmission is assumed to be 50%. The average target thickness and beam current are assumed to be 350 μg/cm^2 and 1.0 pμA, respectively. The Db isotopes are to be produced using PbS targets and the Sg isotope is to be produced using BiS targets. The efficiency from gas cell to the MRTOF system is assumed to be 10%.

	σ_{ER} [nb]	$Y_{\mathrm{GARIS-II}}$ [cpd]	Y_{MRTOF} [cpd]	$Y_{\alpha-\mathrm{TOF}}$ [cpd]
^{256}Db	0.3	82	8.2	4.1
^{258}Db	2.0	547	54.7	27.3
^{259}Sg	0.3	82	8.2	4.1

5.1.2 Mass measurement of Mc/Nh produced by hot fusion reaction

Furthermore, we are planning a flagship experiment of the SHE-Mass II project wherein we will perform direct mass measurement of isotopes of Mc, and their α-decay daughter Nh, produced in the hot fusion reaction system ^{48}Ca+^{243}Am. The ^{243}Am(^{48}Ca, 3n)^{288}Mc reaction has been reported to have a fusion-evaporation cross-section of 8.5 pb [132], which is relatively high among nuclei above $Z = 110$. It is often used for technical demonstrations in superheavy nuclei experiments using hot fusion reactions, such as X-ray measurements [23] and mass number identification [38]. The ^{243}Am has a high melting point (995 °C) and the targets can be produced by electrodeposition onto a strong, 3 μm-thick Ti backing. It is expected these targets would ba capable to withstand irradiation with a high intensity beam of about 2 pμA. Assuming an increase in MRTOF transport efficiency to 10%, the yield is expected to be about one event per 3 days in SHE-Mass facility II. The α-decay energies of ^{288}Mc and ^{284}Nh are 10.2-10.6 MeV and 9.98 MeV [132], which are far away from the α-energies of the transfer products from the ^{243}Am target, Therefore, it is expected that there will be less

accidental coincidence. The combination of MRTOF and α-TOF will enable us to measure even such low yield nuclei with a high accuracy.

The half-life of ^{288}Mc is reported to be approximately 160 ms. As ions stopped in the gas cell require, on average, $\sim$30 ms to be extracted about 10% decayed to ^{284}Nh during transport in the gas cell. Since the MRTOF is capable of measuring different A/q species with a wide band, both ^{288}Mc and ^{284}Nh can be measured simultaneously.

Moreover, the nuclides ^{288}Mc and ^{284}Nh are the α-decay daughter and granddaughter of the isotope ^{296}119 which is expected to be produced by the ^{248}Cm(^{51}V,3n) reaction. This reaction is presently being used in an ongoing campaign for discovery of new elements at the RIKEN Nishina Center. The mass measurement of Mc/Nh can thereby make a significant contribution in terms of identifying unknown new superheavy elements.

5.2 Future development of α/β-TOF detector

We have begun the investigation and development of for the next generation of α-TOF – the so-called α/β-TOF detector, which has the added capability to detect β-decays. The Si detector (Hamamatsu S3590-09) used in the α-TOF has a 300 μm depletion layer. This is thick enough to measure an α-ray but is not sufficient for the detection of light charged particles such as β-rays. Therefore, we are constructing new devices wherein the 300-μm Si detector is replaced with a $\Delta E - E$ telescope consisting of two relatively thick 500-μm Si detectors in a stack. A conceptual diagram of the upgraded design is shown in Fig. 5.1.

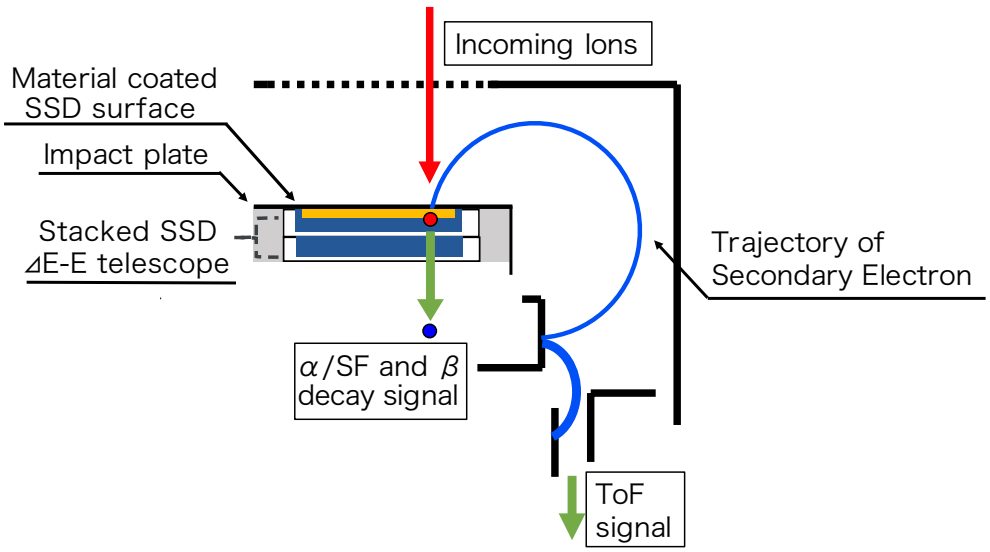

Figure 5.1: Conceptual diagram of the new α/β-TOF detector. The detector consists of a stack of two Si detectors.

The top Si detector is coated with a secondary electron emitting material on the surface, similar to the α-TOF, to provide electrons for time-of-flight signal acquisition. By using two Si detectors stacked on top of each other, the Si detector can detect β-rays while maintaining its sensitivity to α-rays. Figure 5.2 shows the nuclear chart with the regions to be studied with decay-assisted MRTOF measurements at SHE-Mass II ("GARIS-MRTOF") and sister projects at the KEK Isotope Separation System ("KISS-MRTOF") and ZeroDegree spectrometer ("ZD-MRTOF") have been indicated. In addition to studying fusion-evaporation products at GARIS-II, nuclei produced by in-flight fission and fragmentation at ZD and by multinucleon transfer at KISS will be studied. Eventually, the α/β-TOF will allow study of exotic transuranium nuclide produced by multinucleon transfer at KISS which are important for understanding the islands of stability. In the near future, however, the upgraded detector will be used in studies of neutron-rich nuclides important to understanding the astrophysical r-process, which is responsible for synthesis of heavy elements in astronomical objects. The mass measurement techniques of MRTOF equipped with an α/β-TOF detector will advance our understanding of these nuclides.

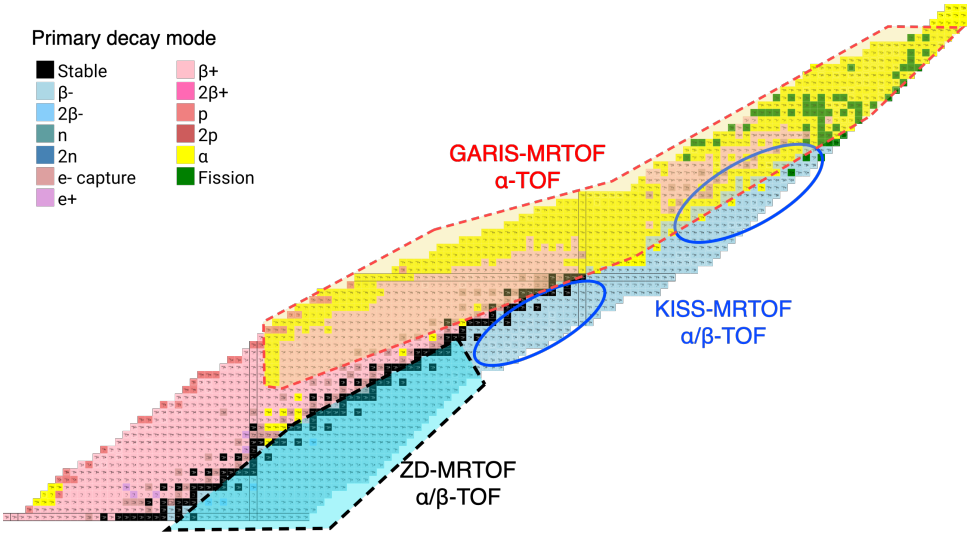

Figure 5.2: Areas on the nuclear chart expected to be explored by MRTOF equipped with an α/β-TOF detector system.

Chapter 6

Conclusion

In this study, we have developed a novel detector, α-TOF, which enables us to perform high-confidence mass measurements through correlation of ion implantation TOF events with subsequent α-decay events. It is an indispensable detector for accurate mass measurements of rare events such as superheavy nuclei with less than a few events per day, which must be discriminated from the background. The offline characterization of the α-TOF was evaluated using a 3 mixed α-source and ^{224}Ra radioactive source. The α-TOF has an α-decay energy resolution of σ_E=141.1(9) keV and time resolution of 250.6(68) ps. In addition to its utility in mass measurements of extremely low-yield α-decaying species, we have demonstrated that the half-life can be derived from the time difference between the arrival time and the decay time of the ions. Moreover, in subsequent online performance test, ions of the isotope ^{207}Ra, produced in the ^{51}V+^{159}Tb reaction system, were measured in a high background environment to demonstrate the ability of the decay correlation to suppress background events.

Furthermore, the α-TOF detector also enables nuclear spectroscopy studies by simultaneous measurement of time-of-flight and decay. The decay correlated mass measurement of ^{206,207}Ra produced by ^{51}V+^{159}Tb reaction have been performed to directly determine the mass excess ME(^{206}Ra) =3540(54) keV and ME(^{207g}Ra)=3538(15) keV and also the excitation energy of ^{207m}Ra is E_{ex}=552(42) keV. Moreover, the α-decay branching ratio of ^{207m}Ra was determined from the measured time-of-flight signal and its decay properties, and spin-parity was estimated to be $13/2^+$, based on its systematics with the reduced alpha width (δ^2) of the neighborhood nucleus.

The first direct mass measurement of a superheavy nuclei, ^{257}Db produced by the ^{208}Pb(^{51}V, 2n) reaction, was successfully measured using an MRTOF equipped with an α-TOF detector. In a total of 105 hours of beam irradiation, we acquired 11 events of ^{257}Db^{3+} with time-of-flight signals correlated to subsequent α-decay events. The measured correlated decay events are consistent with the decay properties of ^{257}Db and its

decay product nuclei. The mass excess of ^{257}Db was determined to be $ME(^{257}\mathrm{Db})$=100 063(231)(2) keV from a weighted average of 11 high-confidence events. The deviation from the indirectly determined value ME_{Indirect}= 100 234(224)(2) keV from our previous study was calculated to be ΔME=171(231) keV. Based on the ^{257}Db mass and the reported Q_α=10 500(50) keV/c^2, the mass excess of ^{261}Bh was indirectly determined to be $ME(^{261}\mathrm{Bh})$=112 988(236) keV/c^2. The mass excess of ^{257}Db and ^{261}Bh were compared to the global mass model, both value agrees with the macroscopic-microscopic calculation FRDM12 and WS4$^{\mathrm{RBF}}$. In addition, the mass excess derived from each of the individual events were clearly distinguished from those of isobars with different atomic numbers. It was experimentally shown that a single event is sufficient for the identification of Z and A, which demonstrates that accurate and precision mass measurement is an extremely powerful tool for the identification of superheavy nuclei.

Acknowledgments

First of all, I would like to thank my supervisor, Prof. Kosuke Morita, I deeply appreciate the teaching me an innumerable amount of nuclear physics. I would also like to thank him for enlightening me, when a high school student, on the joys of science and paving the way for superheavy elements research.

I would like to express heartfelt gratitude Prof. Michiharu Wada, who always gave me the teaching of an experimental techniques, fruitful advices, enlightening discussion. I really respect him as a scientist, and I would like to be a scientist like him.

I would also like to thank Dr. Kouji Morimoto who gave me useful discussions and advice for research and the opportunity for me to join the SHE team as the JRA program. I also thank Dr. Daiya Kaji who always help me in the preparation of the experiment and gave me a lot of advice for my research. I have been always impressed by his ideas for experiments.

I am deeply thankful to Dr. Peter Schury who gave me a lot of experimental techniques and knowledge of electronics and provided a lot of helpful suggestions and discussions with my poor English.

I would like to thank Dr. Sota Kimura, Dr. Yuta Ito and Dr. Marco Rosenbusch who gave me useful knowledge and experience for my research. I would also like to thank Dr. Pierre Brionett and Dr. Satoshi Ishizawa, who my colleagues and friends for their enjoyable discussions and encouragement during my life at RIKEN. I also appreciate to Dr. Kunihiro Fujita who gave me a fruitful advice during my master degree course.

I am express appreciate to the KEK/WNSC and RIKEN members, Prof. Hiroari Miyatake, Prof. Yutaka Watanabe, Dr. Yoshikazu Hirayama, Dr. Takashi Hashimoto, Prof. Daisuke Nagae, Dr. J.-Y. Moon, Mr. Shun Iimura, Dr. Hironobu Ishiyama, Dr. Aiko Takamine, Dr. Taiki Tanaka, Prof. Hermann Wollnik. Also appreciate to the research collaborators. I appreciate to the RIKEN Junior Research Associate Program.

I am grateful to the member of Kyushu University, Prof. Satoshi Sakaguchi, Prof. Masato Asai, Dr. Shintaro Go, Dr. Masaomi Tanaka and secretary Mrs. Keiko Saeki.

I would also like to thank the members of Ph.D thesis committee, Prof. Junji Tojo, Prof. Michiharu Wada, Prof. Kosuke Morita, Prof. Daisuke Nagae for

their useful advice and comments.

I also express my special thanks to Ms. Madoka Takagi who cheerful support and encouragement to me. I hope the days to come with you will be fruitful.

Finally, I would like to thank my parents and sisters for their love and kind support.

Appendix A

Statistical error and figure of merit

Radioactive decay of nuclei is a random event. Therefore, the decay event is described by Poisson statistics and the observed value has a statistical error. If x is the measured value, t is the measurement time, the symbol C is the measured object plus background, and B is related to the background, the observed value S of the counting rate expressed by

$$S = \frac{x_C}{t_C} - \frac{x_B}{t_B}. \tag{A.1}$$

Then, the standard deviation of S, σ_S, is

$$\sigma_S = \left(\frac{x_C}{t_C^2} + \frac{x_B}{t_B^2} \right)^{1/2}. \tag{A.2}$$

The relative error E can be written as $E = \sigma_s/S$. Here put $C = x_C/t_C, B = x_B/t_B$, and differentiating Eq. (A.2),

$$\sigma_s \mathrm{d}\sigma_s = -\left(\frac{C}{t_C^2} \right) \mathrm{d}t_C - \left(\frac{B}{t_B^2} \right) \mathrm{d}t_B. \tag{A.3}$$

To minimize this error $\mathrm{d}\sigma_S/\mathrm{d}t_c = 0$, and the time constant condition is $\mathrm{d}t_c + \mathrm{d}t_B = 0$. Substituting these into Eq. (A.3),

$$\frac{t_C}{t_B} = \left(\frac{C}{B} \right)^{1/2} \quad \text{or} \quad t_B = \frac{T}{1 + (C/B)^{1/2}}, \tag{A.4}$$

where T is the total counting time. The minimum value of error $(\sigma_s)_{\min}$ is obtained from Eqs. (A.2) and (A.4),

$$(\sigma_s)_{\min} = \left(\frac{C}{T} \right)^{1/2} + \left(\frac{B}{T} \right)^{1/2}. \tag{A.5}$$

Substituting Eqs. (A.5) and (A.4) into E,

$$E = E_{min} = \frac{(\sigma_s)_{\min}}{S} = \left\{ \left(\frac{C}{T}\right)^{1/2} + \left(\frac{B}{T}\right)^{1/2} \right\} \frac{1}{(C-B)} = \frac{1}{T^{1/2}(C^{1/2} - B^{1/2})}. \tag{A.6}$$

Transforming this,

$$S = \{1 + 2E\sqrt{TB}\}(E^2 T)^{-1}. \tag{A.7}$$

If ϵ is the total efficiency including geometric efficiency and detection efficiency, the radioactive intensity A is

$$A = \frac{S}{\epsilon} = \{1 + 2E\sqrt{TB}\}(\epsilon E^2 T)^{-1}. \tag{A.8}$$

According to Eq. (A.8), the most sensitive detector is that minimizes $(1 + 2E\sqrt{TB})/\epsilon$. If we set $E^2 = Q/T$, then from Eq. (A.6),

$$Q = \frac{1}{(C^{1/2} - B^{1/2})^2} = \frac{\{(C/B)^{1/2} + 1\}^2 B}{S^2}. \tag{A.9}$$

For low-level radiation, i.e. $S \ll B$, C=B and $t_B \sim T/2$ from Eq. (A.4) and $Q = 4B/S^2$ from Eq. (A.9). Therefore, Q can be used as a benchmark for comparison of measurement conditions when the size of (S, B) is used as a guide. The reciprocal of Q,

$$Q^{-1} = \frac{S^2}{4B} \quad \text{or} \quad 4Q^{-1} = \frac{S^2}{B}, \tag{A.10}$$

or in units of the background error,

$$(4Q^{-1})^{1/2} = \frac{S}{\sqrt{B}}, \tag{A.11}$$

is called the figure of merit (FOM) of the detector.

Appendix B

Fitting code for ^{206,207}Ra measurements

The ROOT macros used for the fitting of ^{206}Fr, ^{206}Ra, and ^{207}Fr, ^{207}Ra performed in Chapter 3 are described below.

B.1 Macro for ^{206}Fr,^{206}Ra

Source B.1 is the function used for fitting of ^{206}Fr and ^{206}Ra. Equation 3.2 is used for fitting of each ion. In the ^{206}Ra measurement of 267 laps, there was a bump structure that was assumed to be a molecular ion, thus the fitting was done including the bump structure. The ^{206}Fr is used as the isobaric reference to determine the shape of the fitting function and the switching points of the left and right side tails, and the fitting of the ^{206}Ra is done in ratio to the reference. The fitting of ^{206}Ra is a simultaneous fitting of these by displaying the events of decay correlation in a different position than the singles events.

Source B.1: Fitting function for ^{206}Fr and ^{206}Ra.

```
1  \\ ———— definition of parameter ————
2  \\ [0],[6],[8],[10] Amplitude
3  \\ [1] Time-of-flight of reference
4  \\ [2] Standard deviation
5  \\ [3] delta t_L
6  \\ [4] delta t_R
7  \\ [7],[9] Ratio of TOF
8  \\ [11] Ratio of decay correlated and singles 206Ra
9
10 TF1 *fit1  =
11   new TF1("fit1","
12     ((x>9423)&&(x<9424))*((x<([1]-[3]))*[0]*exp(0.5*([3])*((2*x
         -2*[1]+([3])))/([2]^2))+(([1]-[3])<x&&x<([1]+[4]))*[0]*exp(-0.5*((
         x-[1])/([2]))^2)+(x>([1]+[4]))*[0]*exp(0.5*[4]*((2*[1]-2*x+[4]))
         /([2]^2))) +
13     \\ fitting for reference ion 206Fr
14
```

```
15      ((x>9423.1)&&(x<9423.25))*((x<(([1]*[7])-[3]))*[6]*exp(0.5*([3])*((2*x
            -2*([1]*[7])+([3])))/([2]^2))+((([1]*[7])-[3])<x&&x<(([1]*[7])
            +[4]))*[6]*exp(-0.5*((x-([1]*[7]))/([2]))^2)+(x>(([1]*[7])+[4]))
            *[6]*exp(0.5*[4]*((2*([1]*[7])-2*x+[4]))/([2]^2))) +
16      \\ fitting for bump structure
17
18      ((x>9423.3)&&(x<9424))*((x<(([1]*[9])-[3]))*[8]*exp(0.5*([3])*((2*x
            -2*([1]*[9])+([3])))/([2]^2))+((([1]*[9])-[3])<x&&x<(([1]*[9])
            +[4]))*[8]*exp(-0.5*((x-([1]*[9]))/([2]))^2)+(x>(([1]*[9])+[4]))
            *[8]*exp(0.5*[4]*((2*([1]*[9])-2*x+[4]))/([2]^2))) +
19      \\ fitting for decay correlated 206Ra
20
21      ((x>9423.1)&&(x<9423.5))*((x<(([1]*([9]/[11]))-[3]))*([10])*exp
            (0.5*([3])*((2*x-2*([1]*([9]/[11])))+([3])))/([2]^2))
            +((([1]*([9]/[11]))-[3])<x&&x<(([1]*([9]/[11]))+[4]))*([10])*exp
            (-0.5*((x-([1]*([9]/[11]))))/([5]*[2]))^2)+(x>(([1]*([9]/[11]))
            +[4]))*([10])*exp(0.5*[4]*((2*([1]*([9]/[11]))-2*x+[4]))/([2]^2)))
22      \\ fitting for singles 206Ra
23      ",9423,9424);
```

B.2 Macro for ^{207}Fr, $^{207g/m}$Ra

The macro code used for fitting ^{207}Fr and, $^{207g/m}$Ra is shown in Source B.2. As in the analysis of ^{206}Fr, the shape of the function is determined from ^{207}Fr, which was used as an isobaric reference. By sharing the fitting parameters of the decay correlated event and singles events, the position of the isomeric state determined by the decay correlated ^{207m}Ra events was feedback into the fitting of singles to derive the time-of-flight ratio of the ground state and the isomeric state.

Source B.2: Fitting function for ^{207}Fr and $^{207g/m}$Ra.

```
1   \\ ———— definition of parameter ————
2   \\ [0],[6] Amplitude
3   \\ [1] Time-of-flight of reference
4   \\ [2] Standard deviation
5   \\ [3] delta t_L
6   \\ [4] delta t_R
7   \\ [5] scaling factor (Not use, fix to 1)
8   \\ [7] Ratio of TOF
9   \\ [12],[14],[16] Ratio of Amplitude
10  \\ [13] Ratio decay correlated and singles 207Ra
11  \\ [15] TOF of decay correlated 207Ra
12
13  TF1 *fit1 =
14    new TF1("fit1","
15      ((x>9410.55)&&(x<9410.75))*((x<([1]-[5]*[3]))*[0]*exp(0.5*([3])*((2*x
            -2*[1]+([3])))/([5]*[2]^2))+(([1]-[5]*[3])<x&&x<([1]+[5]*[4]))
            *[0]*exp(-0.5*((x-[1])/([5]*[2]))^2)+(x>([1]+[5]*[4]))*[0]*exp
            (0.5*[4]*((2*[1]-2*x+[4]))/([5]*[2]^2))) +
16      \\ fitting for reference ion 207Fr
17
18      ((x>9410.75)&&(x<9410.90))*((x<(([1]*[7])-[5]*[3]))*[6]*exp(0.5*([3])
            *((2*x-2*([1]*[7])+([3])))/([5]*[2]^2))+((([1]*[7])-[5]*[3])<x&&x
            <(([1]*[7])+[5]*[4]))*[6]*exp(-0.5*((x-([1]*[7]))/([5]*[2]))^2)+(x
            >(([1]*[7])+[5]*[4]))*[6]*exp(0.5*[4]*((2*([1]*[7])-2*x+[4]))
            /([5]*[2]^2))) +
```

```
19      \\  fitting for singles 207gRa
20
21      ((x>9410.75)&&(x<9410.90))*((x<(([1]*([15]/[13]))-[5]*[3]))*([6]*[12])
            *exp(0.5*([3])*((2*x-2*([1]*([15]/[13]))+([3])))/([5]*[2]^2))
            +((([1]*([15]/[13]))-[5]*[3])<x&&x<(([1]*([15]/[13]))+[5]*[4]))
            *([6]*[12])*exp(-0.5*((x-([1]*([15]/[13])))/([5]*[2]))^2)+(x
            >(([1]*([15]/[13]))+[5]*[4]))*([6]*[12])*exp
            (0.5*[4]*((2*([1]*([15]/[13]))-2*x+[4]))/([5]*[2]^2))) +
22      \\  fitting for singles 207mRa
23
24      ((x>9410.95)&&(x<9411.15))*((x<(([1]*[15])-[5]*[3]))*([6]*[14])*exp
            (0.5*([3])*((2*x-2*([1]*[15])+([3])))/([5]*[2]^2))+((([1]*[15])
            -[5]*[3])<x&&x<(([1]*[15])+[5]*[4]))*([6]*[14])*exp(-0.5*((x
            -([1]*[15]))/([5]*[2]))^2)+(x>(([1]*[15])+[5]*[4]))*([6]*[14])*exp
            (0.5*[4]*((2*([1]*[15])-2*x+[4]))/([5]*[2]^2))) +
25      \\ fitting for decay correlated 207mRa
26
27      ((x>9410.95)&&(x<9411.15))*((x<(([1]*[7]*[13])-[5]*[3]))
            *([6]*[14]*[16])*exp(0.5*([3])*((2*x-2*([1]*[7]*[13])+([3])))
            /([5]*[2]^2))+((([1]*[7]*[13])-[5]*[3])<x&&x<(([1]*[7]*[13])
            +[5]*[4]))*([6]*[14]*[16])*exp(-0.5*((x-([1]*[7]*[13]))/([5]*[2]))
            ^2)+(x>(([1]*[7]*[13])+[5]*[4]))*([6]*[14]*[16])*exp
            (0.5*[4]*((2*([1]*[7]*[13])-2*x+[4]))/([5]*[2]^2)))
28      \\ fitting for decay correlated 207gRa
29      ",9410.55,9411.15);
```

Appendix C

Table of confidence level

For each of the 14 decay correlated events, the confidence levels for comparison with the decay energies and decay times of the ^{257}Db series nuclides and ^{211}Po are summarized in Tables C.1 and C.2.

Table C.1: Confidence level of energy P_{ene}, and decay time P_{dt} for each isotopes.

	E_α [MeV]	dt [s]	$P_{ene}(^{257}\mathrm{Db}(1))$	$P_{dt}(^{257}\mathrm{Db}(1))$	$P_{ene}(^{257}\mathrm{Db}(2))$	$P_{dt}(^{257}\mathrm{Db}(2))$	$P_{ene}(^{257}\mathrm{Db}(3))$	$P_{dt}(^{257}\mathrm{Db}(3))$
E1	9.19	3.54	0.67	0.42	0.13	0.76	<0.01	0.76
E2	8.14	105	<0.01	0.02	<0.01	0.06	<0.01	0.06
E3	8.02	18.5	<0.01	0.09	<0.01	0.31	<0.01	0.32
E4	7.52	100.2	<0.01	0.02	<0.01	0.06	<0.01	0.06
E5	9.00	0.7	0.06	0.48	0.42	0.02	0.69	0.02
E6	9.35	1.3	0.02	0.92	<0.01	0.13	<0.01	0.13
E7	7.48	93.9	<0.01	0.02	<0.01	0.06	<0.01	0.92
E8	7.81	44	<0.01	0.04	<0.01	0.13	<0.01	0.13
E9	9.35	0.36	0.02	0.13	<0.01	<0.01	<0.01	<0.01
E10	7.52	21.1	<0.01	0.09	<0.01	0.27	<0.01	0.27
E11	8.08	43.4	<0.01	0.04	<0.01	0.13	<0.01	0.13
E12	8.77	4.3	<0.01	0.37	<0.01	0.92	0.02	0.92
E13	9.06	0.15	0.23	0.76	0.92	<0.01	0.23	<0.01
E14	9.16	1.2	0.92	0.92	0.23	0.11	0.02	0.11

Table C.2: Confidence level of energy P_{ene}, and decay time P_{dt} for each isotopes. (continued)

	$P_{ene}(^{253}\mathrm{Lr}(1))$	$P_{dt}(^{253}\mathrm{Lr}(1))$	$P_{ene}(^{253}\mathrm{Lr}(2))$	$P_{dt}(^{253}\mathrm{Lr}(2))$	$P_{ene}(^{249}\mathrm{Md})$	$P_{dt}(^{249}\mathrm{Md})$	$P_{ene}(^{245}\mathrm{Es})$	$P_{dt}(^{245}\mathrm{Es})$	$P_{ene}(^{211}\mathrm{Po})$
E1	<0.01	0.84	<0.01	0.62	<0.01	<0.01	<0.01	<0.01	<0.01
E2	<0.01	0.04	<0.01	0.07	0.16	0.48	<0.01	0.62	<0.01
E3	<0.01	0.27	<0.01	0.37	0.92	0.27	<0.01	<0.01	<0.01
E4	<0.01	0.04	<0.01	0.07	<0.01	0.55	<0.01	0.62	0.38
E5	<0.01	0.03	<0.01	<0.01	<0.01	<0.01	<0.01	<0.01	<0.01
E6	<0.01	0.19	<0.01	0.09	<0.01	<0.01	<0.01	<0.01	<0.01
E7	<0.01	0.06	<0.01	0.92	<0.01	0.55	<0.01	0.55	0.71
E8	<0.01	0.11	<0.01	0.16	<0.01	0.92	0.32	0.11	<0.01
E9	<0.01	<0.01	<0.01	<0.01	<0.01	<0.01	<0.01	<0.01	<0.01
E10	<0.01	0.23	<0.01	0.32	<0.01	0.42	<0.01	<0.01	0.38
E11	<0.01	0.11	<0.01	0.16	0.48	0.92	<0.01	0.11	<0.01
E12	0.55	0.92	0.84	0.76	<0.01	<0.01	<0.01	<0.01	<0.01
E13	<0.01	<0.01	<0.01	<0.01	<0.01	<0.01	<0.01	<0.01	<0.01
E14	<0.01	0.19	<0.01	0.07	<0.01	<0.01	<0.01	<0.01	<0.01

Bibliography

[1] S. Hofmann, et al., Eur. Phys. J. A. 52 (2016) 180.

[2] A. Sobiczewski, et al., Phys. Lett. 22 (1966) 500.

[3] M. Schadel, Acta Phys. A 34 (2003) 1701.

[4] N. Bohr, Nature 137 (1936) 344.

[5] S. Hoffman, et al., Rev. Mod. Phys. 72 (2000) 733.

[6] G. Gamow, Z. Phys. 52 (1928) 510.

[7] R. W. Gurney, et al., Phys. Rev. 33 (1929) 127.

[8] V. E. Viola, et al., Nucl. Chem. 28 (1966) 741.

[9] Z. Patyk, et al., Nucl. Phys. A 502 (1989) 591.

[10] R. Smolanczuk, Phys. Rev. C 56 (1997) 812.

[11] K. P. Santhosh, et al., Nucl. Phys. A 825 (2009) 159.

[12] R. G. Thomas, Prog. Theor. Phys. 12 (1954) 253.

[13] H. J. Mang, Phys. Rev. 119 (1960) 1069.

[14] J. O. Rasmussen, Phys. Rev. 113, 1593 (1959).

[15] T. Nomura, KEK Report (2005).

[16] N. Bohr, et al., Phys. Rev. 56 (1939) 426.

[17] J. H. Hamilton, et al., Annu. Rev. Nucl. Part. Sci. 63 (2013) 383.

[18] P. J. Karola, et al., Pure Appl. Chem. 88 (2016) 139.

[19] P. J. Karola, et al., Pure Appl. Chem. 88 (2016) 155.

[20] S. Hofmanna, et al., Pure Appl. Chem. 92 (2020) 1387.

[21] G. J. H. Moseley. Philosophical Magazine. 27 (1914) 703.

[22] C. E. Bemis et al., Phys. Rev. Lett. 31 (1973) 10.

[23] D. Rudolph et al., Phys. Rev. Lett. 111 (2013) 112502.

[24] K. Blaum, Physics Reports, 425 (2006) 1.

[25] W. Huang, et al., Chin. Phys. C 41 (2017) 030002.

[26] J. M. Pearson et al., Eur. Phys. J. A, 50 (2014) 43.

[27] V. M. Strutinsky. Nuclear Physics A, 122 (1968) 1.

[28] J. K. L. MacDonald. Physical Review, 43 (1933) 830.

[29] P. Dendooven, Nucl. Instrum. Methods Phys. Res. B 126 (1997) 182.

[30] F. Arai, et al., Int. J. Mass Spectrum. 362 (2014) 56.

[31] G. Bollen, Int. J. Mass Spectrum. 299 (2011) 131.

[32] D. Lunney. et al., Rev. Mod. Phys. 75 (2003) 1021.

[33] D. Beck. et al., Eur. Phys. J. A. 8 (2000) 307.

[34] J. J. Thomson, Proc. R. Soc. Lond. A 89 (1913) 1.

[35] R. Klapisch, et al., Phys. Rev. Lett. 31 (1973) 118.

[36] D. M. Moltz, et al., Phys. Rev. C 26 (1982) 1914.

[37] J. M. Gates. EPJ Web of Conference 131 (2016) 08003.

[38] J. M. Gates, et al., Phys. Rev. Lett. 121 (2018) 222501.

[39] J. K. Pore, et al., Phys. Rev. Lett. 124 (2020) 252502.

[40] B. Franzke., Nucl. Instrum. Methods Phys. Res. B 24/25 (1987) 18.

[41] M. Hausmann, et al., Nucl. Instrum. Methods Phys. Res. A 446 (2000) 569.

[42] Yu. A. Litvnov, et al., Nuclear Physics A 756 (2005) 3.

[43] Edmund G. Myers, Nature Physics 12 (2016) 986.

[44] G. Bollen et al., Nucl. Instrum. Methods Phys. Res. A 368 (1996) 675.

[45] V. S. Kolhinen et al., Nucl. Instrum. Methods Phys. Res. B 204 (2003) 502.

[46] G. Savard, et al., Nucl. Phys. A 626 (1997) 353.

[47] S. Schwarz, et al., Nucl. Instrum. Methods Phys. Res. B 204 (2003) 507.

[48] G. Sikler, et al., Nucl. Instrum. Methods Phys. Res. B 204 (2003) 482.

[49] H. Wollnik, et al., Int. J. Mass Spectrom. Ion Process 96 (1990) 267.

[50] R. N. Wolf, et al., Int. J. Mass Spectrum. 349 (2013) 123.

[51] Y. Ito, et al., Phys. Rev. C 88 (2013) 011306(R).

[52] W. R. Plass, et al., Int. J. Mass Spectrum. 349 (2013) 134.

[53] C. Jesch, et al., Hyperfine Interact. 235 (2015) 97.

[54] P. Chauveay, et al., Nucl. Instrum. Methods Phys. Res. B 376 (2016) 211.

[55] T. Y. Hirsh, et al., Nucl. Instrum. Methods Phys. Res. B 376 (2016) 229.

[56] J. -Y. Wang, et al., Nucl. Instrum. Methods Phys. Res. B 463 (2020) 179.

[57] I. Moore, et al., Hyperfine Interact. 223 (2013) 17.

[58] J. Yoon, et al., EPJ Web Conf. 66 (2014) 11042.

[59] B. Franzke, et al., Nucl. Instrum. Methods Phys. Res. B 24/25 (1987) 18.

[60] M. Toyoda, et al., Int. J. Mass Spectrum., 38 (2003) 1125.

[61] A. Casares, et al., Int. J. Mass Spectrum., 206 (2001) 267.

[62] H. Wollnik et al., Int. J. Mass Spectrum. 227 (2003) 217.

[63] P. Schury, et al., Int. J. Mass Spectrum., 359 (2014) 19.

[64] Robert N. Wolf, et al., Int. J. Mass Spectrum., 313 (2012) 8.

[65] F. Wienholtz, et al., Nature, 498 (2013) 346.

[66] T. Dickel, et al., Nucl. Instrum. Methods Phys. Res. A 777 (2015) 172.

[67] J.S. Winfield, et al., Nucl. Instrum. Methods Phys. Res. A 704 (2013) 76.

[68] T. Kubo, Nucl. Instrum. Methods Phys. Res. B 204 (2003) 97.

[69] D. Kaji, et al., Nucl. Instrum. Methods Phys. Res. B 317 (2013) 311.

[70] S. C. Jeong, et al., KEK Report, 2010.

[71] P. Schury, et al., Nucl. Instrum. Methods Phys. Res. B 376 (2016) 425.

[72] K. Morita, et al., J. Phys. Soc. Jpn. 73 (2004) 2593.

[73] P. Schury et al., Nucl. Instrum. Methods Phys. Res. A 407 (2017) 160.

[74] Lars von der Wense, et al., Nature 533 (2016) 47.

[75] A. Kramida, et al., NIST Atomic Spectra Database (ver. 5.7.1).

[76] Y. Ito, et al., Nucl. Instrum. Methods Phys. Res. B 317 (2013) 544.

[77] HeatWave Labs, available at http://www.cathode.com/.

[78] Y. Ito Ph.D thesis. University of Tsukuba (2014).

[79] S. Kimura, et al., Int. J. Mass Spectrum. 430 (2018) 134.

[80] Y. Ito et al., Phys. Rev. Lett. 120 (2018) 152501.

[81] E. Minaya Ramirez, et al., Science 337 (2012) 1207.

[82] M. Block, et al., Nature, 463 (2010) 785.

[83] M. Dworschak, et al., Phys. Rev. C 81 (2010) 064312.

[84] P. Schury, et al., in prep.

[85] M. Eibach, et al., Phys. Rev. C 89 (2014) 064318.

[86] ETP Electron Multipliers, Product data document.

[87] O. Nilsson, et al. Nucl Instrum and Methods., 84 (1970) 301.

[88] Y. Ushio, et al. Thin Solid Films, 167 (1998) 299.

[89] J. B. Johnson, et al., Phys. Rev. 91 (1953) 582.

[90] D.R. Lide, CRC Handbook of Chemistry and Physics, 81st ed., CRC Press, (2001) 39.

[91] T. Shanley, et al., private communication.

[92] K. Hunter, et al., Ion detection, John Wiley Sons, Ltd, (2009) 117.

[93] F. Busch et al., Nucl Instrum and Methods. 171 (1980) 71.

[94] K. Morimoto et al., RIKEN Accel. Prog. Rep. 46 (2013) 191.

[95] J. Narbutt, A. Bilewicz, Appl. Radiat. Isot. 49 (1998) 89.

[96] S. C. Wu. Nuclear Data Sheets 108 (2007) 1057.

[97] K.H. Schmidt, et al., Z. Phys. A 316 (1984) 19.

[98] D. Kaji, et al., Nucl. Instrum. Methods Phys. Res. A 792 (2015) 11.

[99] Y. A. Lazarev, et al., Phys. Rev. Lett. 75 (1995) 1903.

[100] K. Morita, Nuclear Phys. A 944 (2015) 30.

[101] F. P. Hessberger, et al., Eur. Phys. J. A. 41 (2009) 145.

[102] C. M. Folden, et al., Phys. Rev. Lett. 93 (2004) 101.

[103] K. E. Gregorich, et al., Phys. Rev. C 74 (2006) 135.

[104] B. Streicher, et al., Eur. Phys. J. A 45 (2010) 275.

[105] M. Kowalska, et al., Nucl. Instrum. Methods Phys. Res. A 689 (2012) 102.

[106] C. Lorenz, et al., Phys. Rev. C 96 (2017) 849.

[107] T. Dickel, et al., Phys. Lett. B 744 (2015) 137.

[108] F. G. Kondev, S. Lalkovski, Nuclear Data Sheets 112 (2011) 707.

[109] F. P. Hessberger, et al., Europhys. Lett. 3 (1987) 895.

[110] James F. Ziegler, Nucl. Instrum. Methods Phys. Res. B 219-220 (2004) 1027.

[111] Data extracted using the NNDC On-Line Data Service from the ENSDF database, file revised as of 2014-01-08. M. R. Bhat, Evaluated Nuclear Structure Data File (ENSDF), Nuclear Data for Science and Technology, www.nndc.bnl.gov.

[112] M. Rosenbusch et al., Phys. Rev. C 97 (2018) 064306.

[113] Z. Kalaninova, et al., Phys. Rev. C 89 (2014) 054312.

[114] Albert Ghiorso, et al., Phys. Rev. Lett. 24 (1970) 1498.

[115] F. P. Hessberger, et al., Z. Phys. A, 322 (1985) 557.

[116] F. P. Hessberger, et al., Eur. Phys. J. A. 12 (2001) 57.

[117] P. Brionnet. Ph.D thesis, Strasbourg University, 2017.

[118] B. Streicher. Ph.D thesis, Comenius University in Bratislava, 2006.

[119] D. Wittwer, et al., Nucl. Instrum. Methods Phys. Res. B 268 (2010) 28.

[120] J. M. Gates, et al., Phys. Rev. C. 78 (2008) 034604.

[121] A. Kaufmann, et al., Mathematics in Science and engineering Volume 124.

[122] R.T. Birge, Phys. Rev. 40 (1932) 207.

[123] J. Duflo and A. P. Zuker, Phys. Rev. C 52 (1995) 23(R).

[124] J. Mendoza-Temisa, et al., Nucl. Phys. A, 843 (2010) 14.

[125] P. Möller, et al., At. Data Nucl. Data Tables 109 (2016) 1.

[126] N. Wang, et al., Phys. Rev. C 84 (2011) 051303.

[127] S. Goriely, et al., Phys. Rev. C 93 (2016) 034337.

[128] H. Koura, et al., Bulletin Physical Society of Japan (BUTSURI), 60 (2005)

[129] H. Koura, et al., Prog. Theor. Phys. 113 (2005) 305.

[130] C. M. Folden III, et al., Phys. Rev. C 79 (2009) 027602.

[131] P. Brionnet, private communication.

[132] Yu. Ts. Oganessian, et al., Phy. Rev. C 87 (2013) 014302.